

IVANE JAVAKHISHVILI TBILISI STATE UNIVERSITY

ANNA GHEONJIAN

Faculty of Exact and Natural Sciences
Electrical and Electronics Engineering Department

INVESTIGATION OF BROADBAND EMC PROBLEMS RELATED TO ANTENNAS AND CABLES USING ADVANCED COMPUTATIONAL TECHNIQUES

DOCTORAL THESIS

Head of Doctoral Program:

Professor

GEORGE GHVEDASHVILI

Scientific Supervisor:

Doctor

ROMAN JOBAVA

Reviewer:

Professor at ESIGELEC/IRSEEM,
Rouen, France

MONCEF KADI

Reviewer:

Professor at The University of Georgia,
Tbilisi, Georgia

KAKHABER
TAVZARASHVILI

ივანე ჯავახიშვილის სახელობის თბილისის
სახელმწიფო უნივერსიტეტი

ანა გეონჯიანი

ზუსტ და საბუნებისმეტყველო მეცნიერებათა ფაკულტეტი
ელექტრული და ელექტრონული ინჟინერიის დეპარტამენტი

ანტენებთან და კაბელებთან დაკავშირებული
ელექტრომაგნიტური თავსებადობის
ფართოგეოლოგანი ამოცანების შესწავლა
რიცხვითი მეთოდებით

სადოქტორო დისერტაცია

სადოქტორო პროგრამის ხელმძღვანელი:

პროფესორი

გიორგი ღვინაძე

სამეცნიერო ხელმძღვანელი:

ფიზ.-მათ.-მეცნ. კანდიდატი

რომან ჯობაძე

ობონენტი:

პროფესორი, ESIGELEC/IRSEEM

რუანი, საფრანგეთი

მონსიეჟ კადი

ობონენტი:

პროფესორი, საქართველოს უნივერსიტეტი

თბილისი, საქართველო

პასაბერი

თავზარაშვილი

თბილისი 2015

Contents

INTRODUCTION	9
1.1 The Value and Goals of Electromagnetic Compatibility Modeling	9
1.2 Process Chain for Generation of Calculation Model.	11
1.2.1 Car-Body Model Preprocessing	11
1.2.2 Electronic Control Unit Model Generation	12
1.2.3 Cable-Harness Processing	13
1.2.4 Antenna Modelling	14
1.3 Calculation Methods: State of the Art	14
1.3.1 Method of Moments	14
1.3.2 Finite-Element Method	15
1.3.3 Finite-Difference Time-Domain and Finite-Volume Time-Domain ...	16
1.3.4 Hybridisation of Method of Moments and Multi-Transmission Line Methods	17
1.4 Objectives	17
1.5 Outline	18
CHAPTER 1	
MODELLING OF AM AND FM/TV GLASS ANTENNAS IN AUTOMOBILES	19
1.1 Automotive Antenna Overview: Design and Placement	19
1.2 Method of Moments (MoM) for the Solution of Automotive Antenna Problems	23
1.2.1 Traditional MoM	23
1.3 Modelling of Automotive Glass Antennas Using Hybridisation of MoM with a Special Green's Function	25
1.3.1 Problem Formulation.....	25
1.3.2 Theoretical Approach	26
1.4 Validation of the Hybrid MoM Scheme with a Special Green's Function	33
1.4.1 Simple Grid Antenna on a Thin Glass	33
1.4.2 Complex Grid Glass Antenna	35
1.4.3 Automotive Windshield Glass Antenna.....	36

- 1.5 Application of Hybrid MoM Scheme for the Design of Automotive Glass Antennas 37
 - 1.5.1 Complete Car Model with Windshield Antenna 37
 - 1.5.2 Hybridisation of MoM with Multiport Networks 39
 - 1.5.3 Application of Multiport Networks: Simulations of Vehicle Antenna Validation Tests 41
 - 1.5.4 Multi-partitioned and Multi-excitation MoM Scheme 44
 - 1.5.5 Application of Multi-partitioned MoM Scheme to Antenna Design 48
 - 1.5.6 Testing of Vehicle Antenna Reception in an Open-area Far-field Test Setup 49
 - 1.5.7 Conclusion 55

CHAPTER 2

CABLE HARNESS MODELLING 57

- 2.1 Cable Harness Description 57
- 2.2 Simulation of Non-uniform Transmission Lines 59
 - 2.2.1 Introduction 59
 - 2.2.2 Multi-transmission Line (MTL) Approach for the Investigation of Crosstalk in Cables 59
- 2.3 Crosstalk Application Examples 63
- 2.4 Radiation and Susceptibility Hybrid Approaches 65
 - 2.4.1 Introduction 65
 - 2.4.2 Experimental Validation 65
 - 2.4.3 Discussion 70
- 2.5 Modelling of Power Cables 71
 - 2.5.1 Introduction 71
 - 2.5.2 Numerical Model of the Sensor and Cable 72
 - 2.5.3 Conclusions 79
- 2.6 HV Cables for Electric Vehicle Applications 80
 - 2.6.1 Modelling of a Shielded Power Cable with Single Core: Coroplast 35 mm2 80
 - 2.6.2 Modelling of Shielded Power Cable with Single Core: Coroplast 25 mm2 86
 - 2.6.3 Conclusions 89

CHAPTER 3

SIMULATION OF LOW-FREQUENCY MAGNETIC FIELDS IN AUTOMOTIVE EMC

PROBLEMS	91
3.1 Introduction	91
3.2 Theoretical Background	95
3.3 Method Validation	99
3.3.1 Investigation of Shielding Effectiveness with an Infinite Plane	99
3.3.2 Vertical Loop Near a Finite Plate	101
3.3.3 Spherical Shield	103
3.4 Magnetic Fields Radiated by an Automotive Power Cable	103
3.5 Magnetic Field of a Ferrite-Coil Antenna Near Metallic Structures	106
3.5.1 Ferrite-Coil Antenna in Free Space	106
3.5.2 Antenna with Aluminium Shield: Edge Effect	109
3.6 Analysis and Optimisation of Smart-Entry System Performance	111
3.6.1 Operation of External Smart-Entry System	111
3.7 Investigation of Inductive Charging System	113
3.8 Conclusions	114

CHAPTER 4

FULL-WAVE MOM SIMULATIONS OF EM INTERACTIONS IN EMC FILTERS FOR

POWER APPLICATION	115
4.1 Introduction	115
4.2 Validation of 3D MoM Models for Filter Components	116
4.3 Modelling of the 3D Layout Influence on Filter Performance	120
4.4 Modelling of Radiated EM Fields	124
4.5 Conclusions	126
CONCLUSIONS	127
REFERENCE	128
LIST OF FIGURES	140
LIST OF TABLES	145

INTRODUCTION

1.1 The Value and Goals of Electromagnetic Compatibility Modeling

Systems such as automobiles, aeroplanes and ships need special treatment in order to evaluate their electromagnetic compatibility behaviour. If different structures such as antennas, antenna amplifiers, cable bundles, integrated circuits, or large metallic scatterers are to be treated collectively, a numerical solution of the wave equations will give unsatisfying results in most cases.

Various electronic systems and components are used throughout modern vehicles, from traditional entertainment systems to communication and navigation.

As systems and components started to influence each other as a result of their operation, the electronics industry developed concepts and methods to address system interoperation both with other systems and the external environment; included in this is the study of electromagnetic compatibility, which can be defined as “the ability of an electronic system to function properly in its intended electromagnetic environment and not to contribute interference to other systems in the environment”. The goal is to have an EMC system that is immune to emission from other systems and does not interfere with either its own operation or the operation of other systems.

Electromagnetic compatibility is concerned with the generation, transmission and reception of electromagnetic energy; these three aspects of electromagnetic compatibility form the basic framework of any electromagnetic compatibility design. A source (also referred to as an emitter) produces the emission, and a transfer or coupling path transfers the emission energy to a receptor (receiver), where it is processed, resulting in either desirable or undesirable behaviour. Interference occurs if the received energy causes the receptor to behave in an undesirable manner. Transfer of electromagnetic energy occurs frequently via unintended coupling modes. However, the unintentional transfer of energy causes interference only if the received energy is of sufficient magnitude and/or spectral content at the receptor input to cause the receptor to behave in an undesirable manner. It is also important to understand that a source (or receptor) may be classified as intended or unintended. In fact, a source (or receptor) may behave in both modes. Whether the behaviour of the source (or receptor) is intended or unintended depends on the coupling path as well as the type of source (or receptor).

There are four main aspects to electromagnetic compatibility: (i) radiated emissions, (ii) radiated susceptibility, (iii) conducted emissions, and (iv) conducted susceptibility. Modelling can be used to study the coupling of both internal and external sources.

In order to ensure that modern vehicle onboard electronics will not be interfered with or cause interference with themselves or with external receptors, vehicles are tested to certain standards.

Electromagnetic compatibility testing is usually a time-consuming and resource-demanding process. Unfortunately, these tests are often conducted late in the development process when correcting an electromagnetic compatibility problem can be difficult and unduly expensive. Validated analytical and numerical methods have the potential to become increasingly important as a means of determining the effects of external fields on vehicular electronic systems, or of predicting how emission will develop.

Proper electromagnetic compatibility modelling can reduce development resources significantly. If the analysis is performed during the early stages of vehicle design, when the vehicle layout is more flexible, changes to improve immunity can be adopted without an appreciable increase in costs.

To summarise, the primary advantages of adequate electromagnetic compatibility design are:

1. Minimising the additional costs associated with suppression elements or redesign in order to satisfy regulatory requirements (minimising product cost)
2. Maintaining the development and product announcement schedule (minimising development schedule delays)
3. Ensuring that the product will operate satisfactorily in the presence of the inevitable external noise sources at its installation location (minimising customer complaints)

Perhaps the most important factor in ensuring that a product will satisfy the regulatory requirements at the end of the design and that the development schedule will be adhered to, is the early and continuous application of electromagnetic compatibility design principles throughout the entire development cycle of the product.

Thus, the goal of automotive system electromagnetic compatibility modelling is to enable efficient analysis to reduce or to completely replace time-consuming and expensive testing. This is where modelling has the highest likelihood of impacting vehicle system electromagnetic compatibility work and where the most significant benefits are expected.

Results and approaches described in this thesis have been used proactively by the automotive industry during the last decade for electromagnetic compatibility

modelling. Most of the methodologies presented herein have been implemented in the software packages produced by EMCoS Ltd., Tbilisi, Georgia [1].

1.2 Process Chain for Generation of Calculation Model

A successful electromagnetic compatibility computation that is integrated into the development process and gives valuable information for product improvement must adhere to the product development process. Generation of the electromagnetic compatibility calculation model must be performed on a timescale of minutes rather than days. Available data must be adjusted rapidly for electromagnetic compatibility calculations in order to meet time-schedule demands.

Synergy effects between different computer-aided design/engineering groups, as well as mechanical engineering groups, must be maximised. Component measurement results that are generated independently from electromagnetic compatibility computation activities must be included in the design process.

The initial data for the generation of the calculation model needs further processing. The next sections describe the nature and processing of data available from the automotive industry

1.2.1 Car-Body Model Preprocessing

Analytical computer-aided car-body models are not suitable for numerical computation. However, triangular meshes that are processed for the mechanical analysis of a car body provide a good base for the generation of a suitable car-body model for electromagnetic compatibility computations. Mechanical analysis calculates the internal mechanical tensions in a structure, with finite-element methods used widely. The space surrounding the vehicle does not need to be modelled as part of the mechanical calculation. Due to the sparse equation system of finite-element methods, car-body models contain 200,000 up to several million triangular elements.

Fig. 1. shows an initial car model that is represented by a dense mesh containing 334,421 elements.

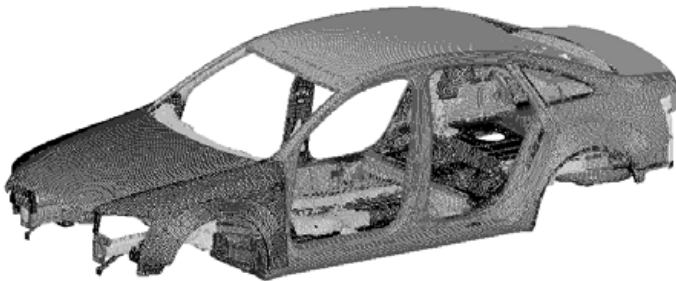


Fig. 1. Initial car model (334,421 elements)

For electrodynamic surface-current and field calculations with large structures, the method of moments was found to be the most appropriate.

Due to the dense matrix involved in these electromagnetic calculations, the number of unknowns must be notably smaller than those in mechanical finite-element calculations. Reasonable mechanical finite-element models contain between 10,000 and 50,000 triangular elements.

Reducing the number of triangular elements and keeping all important information is a time-consuming and complex task. To solve this task, numerous mesh-handling algorithms have been implemented and combined into a program for improved usability [2]. This developed program is called ReMesh [3] and it is partially integrated into EMC Studio. As a result of preprocessing of the initial model, the car body is represented with a coarse mesh. Fig. 2. shows an example of a coarsened mesh containing 11,014 elements (mesh size: 5-7 cm, upper frequency limit: 430 MHz), which is used for electrodynamic calculations.

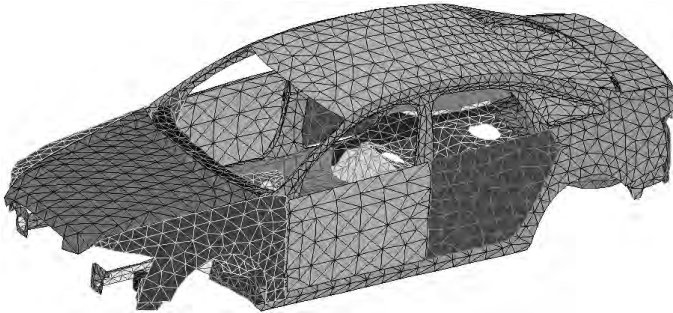


Fig. 2. Coarsened car model (11,014 elements, valid up to 430 MHz)

For rapid calculations at different frequencies, it is useful to have a number of meshes of different mesh sizes. Such models can be easily generated by using a coarsened basic model.

1.2.2 Electronic Control Unit Model Generation

Electronic control unit model generation is a critical task. A modern electronic control unit contains a large number of complex transistor circuits that cannot be modelled in each detail as part of a complete automobile calculation model. Single pins of an electronic control unit or structures have been proposed to be handled with models such as IBIS [4]. Nevertheless, to date, there are no usable methods that are able to overcome the dynamic-range problems of the necessary time-domain measurements or that can model electromagnetic compatibility effects within an integrated-circuit model. Black-box models generated in the frequency domain are the most promising models currently [5] - [7].

1.2.3 Cable-Harness Processing

The modern computer-aided design process for modelling a cable harness leads to a database that contains nearly complete information regarding the vehicle cable harness. What this database does not contain, however, is distinct information regarding the location of each cable in the cross section of the harness bundle. This information is not available and is not necessary for the cable-harness production process. The location of each cable within the bundle can only be determined by statistics.

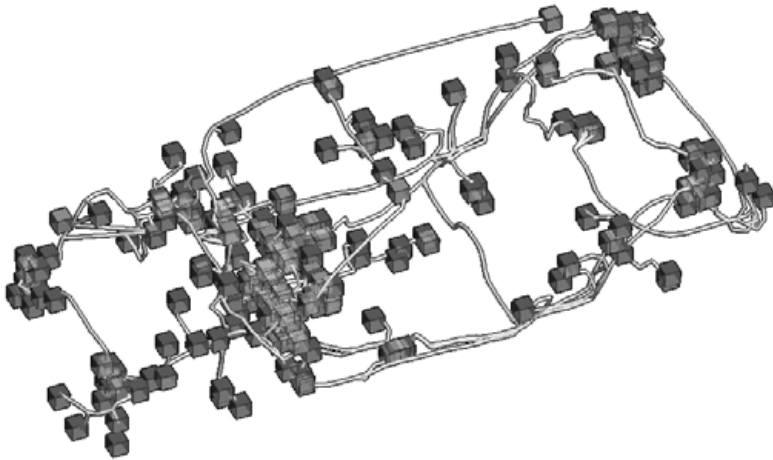


Fig. 3. EMC Studio view of the complex cable harness of a vehicle; boxes represent devices

There is no information, either, regarding how cables pass from one segment to another. Here, the aim of preprocessing is to determine the distinct placement of cables, ready for further calculation. This is only possible when done randomly, based on the rules of wire routing. It is also necessary to extract data from large databases, which contain data on the cables that are used in the calculation model (between 10 and 3,000 cables). For electromagnetic compatibility simulations, database extraction and cable routing is performed using a special module named Harness Studio [8].

1.2.4 Antenna Modelling

Car antennas can have very different shapes and follow different concepts [9]. Most important in modern automobiles are glass antennas. Here the following important aspects must be considered:

- Topology of antenna structures
- Glass permittivity and resistivity of conductors
- Models of amplifiers and antenna terminations

Antenna topology can be provided either as a given model or with knowledge regarding the desired general antenna features; the topology must be optimised in order to obtain these features. For termination/amplifier, linear models need to be generated. If experimental data are available, it is possible to adjust the termination/amplifier models and glass-model parameters. The influence of glass permittivity is considered by using an equivalent-impedance approach within the method of moments. According to this approach, it is possible to determine equivalent-impedance parameters for metallic structures on a dielectric-like glass.

1.3 Calculation Methods: State of the Art

At present, many numerical techniques for modelling electromagnetic compatibility problems are available [10]. Furthermore, numerical electromagnetic modelling is advancing rapidly. Sorting through this wealth of information in order to choose the technique that is best for a particular application can be overwhelming.

The following sections outline several general numerical modelling techniques that have been used to analyse electromagnetic interference source configurations with some success. Each technique is best suited for the analysis of different configurations. No single technique can be used to model all electromagnetic interference sources, however each of these techniques can be applied to a number of electromagnetic-interference source configurations. Two or three of these techniques, collectively, represent a potentially powerful set of tools for the electromagnetic interference engineer.

1.3.1 Method of Moments

The method of moments is a technique for solving complex integral equations by reducing them to a system of more simple linear equations. In contrast to the variation approach of finite-element methods however, the method of moments employs a technique known as the method of weighted residuals. Indeed, the terms method of moments and method-of-weighted-residuals are synonymous. Harrington [11] was largely responsible for popularising the term method of moments in the field of electrical engineering. His pioneering efforts first demonstrated the power and flexibility of this numerical technique for solving problems in electromagnetics.

Depending on the form of the field integral equation that is used, moment methods can be applied to configurations of conductors only, homogeneous dielectrics only, or very specific conductor-dielectric geometries. Moment method techniques applied to integral equations are not very effective when applied to arbitrary configurations with complex geometries or inhomogeneous dielectrics.

The method of moments is appropriate for vehicle simulations, especially in the radio frequency range, where vehicles can be represented by thin metallic structures. A 3D field solver program, TriD, based on the method of moments is part of the program package EMC Studio [1]. Currents on metallic structures consisting of arbitrary shaped wires and surfaces (both open and closed) can be calculated with TriD; near and far fields can be calculated from the currents. The TriD program allows finite conductivity of wire segments to be calculated by specifying their resistance, inductance and capacitance. Values can be frequency dependent. Complex impedances (frequency dependent), as a load to any wire segment, can be used. Any linear time-invariant passive circuit can be incorporated into the calculation with a unique SPICE link. Different types of excitation sources are available in TriD including incident plane waves, voltage sources over a wire segment, current sources, impressed currents, electric and magnetic dipoles, as well as any arbitrary combination of sources. Sources can operate in either the frequency or the time domain. For transient problems, the multi-frequency approach (based on fast Fourier transform) combined with adaptive frequency sampling is applied. Different fast solvers (out-of-core version, parallel-cluster version) are used in TriD for solving the resulting systems of linear equations in order to obtain the coefficients of the current expansion. Out-of-core and parallel solvers are used in large-scale problems. Special algorithms designed to estimate the accuracy of a calculation are included, ensuring high-quality results [12].

1.3.2 Finite-Element Method

Scalar finite-element methods are used widely by civil and mechanical engineers in order to analyse material and structural problems. Electrical engineers use finite-element methods to solve complex, non-linear problems in magnetics and electrostatics. Until recently, however, very little practical modelling of 3D electromagnetic radiation problems had been performed using this technique. There are two reasons for this. Firstly, practical 3D vector problems require significantly more computation than 2D or scalar problems. Secondly, spurious solutions known as vector parasites often result in unpredictable, erroneous results. Active developments in this field [13], [14] appear to have solved the vector parasite problem. The increasing availability of computer resources, coupled with a desire to model more complex electromagnetic problems, has resulted in a renewed interest in finite-element methods for solving electromagnetic-radiation problems.

A major advantage of finite-element methods over other electromagnetic-modelling techniques stems from the fact that the electrical and geometric properties of each

element can be defined independently. This permits the problem to be set up with a large number of small elements in regions of complex geometry and fewer, larger elements in relatively open regions. Thus, it is possible to model configurations with complicated geometries and many arbitrarily shaped dielectric regions in a relatively efficient manner.

1.3.3 Finite-Difference Time-Domain and Finite-Volume Time-Domain

Finite-difference time-domain techniques require the entire volume to be meshed. Unlike most finite-element and method-of-moment techniques, finite-difference time-domain techniques work in the time domain, and thus they are very well suited to transient analysis problems. Like finite-element methods, finite-difference time-domain methods are very good at modelling complex inhomogeneous configurations. As a result, finite-difference time-domain techniques are often the method of choice for modelling unbounded complex inhomogeneous geometries [15].

Surface-conforming finite-difference time-domain techniques with non-rectangular elements have been introduced to address the problem of curvilinear surfaces. One of the most promising of these techniques, which permits each element in the grid to have an arbitrary shape, is referred to as the finite-volume time-domain method [16].

The finite-difference time-domain and finite-volume time-domain methods are widely used for radar cross-section analysis, although they have been applied to a wide range of electromagnetic modelling problems. Their primary advantage is their great flexibility. Arbitrary signal waveforms can be modelled as they propagate through complex configurations of conductors, dielectrics and lossy non-linear non-isotropic materials. Another advantage of these techniques is that they are readily implemented on massively parallel computers and, in particular, on vector processors.

The only significant disadvantage of this technique is that the problem size can easily become unmanageable for some configurations. The fineness of the grid is generally determined by the dimensions of the smallest features that need to be modelled. The volume of the grid must be large enough to encompass the entire object and most of the near field. Large objects with regions that contain small, complex geometries may require large, dense grids. Finally, modelling cable systems is very difficult. When this is the case, other numerical techniques may be significantly more efficient than the finite-difference time-domain or finite-volume time-domain methods.

1.3.4 Hybridisation of Method of Moments and Multi-Transmission Line Methods

To handle the radiation of complex cable bundles, direct methods such as the method of moments are not appropriate. Inhomogeneous charge distribution over the cable cross sections due to close proximity can reduce calculation accuracy. Hybrid methods combining multi-transmission line theory with the method of moments are much more appropriate for such problems. These methods free the user from many of the limitations of pure electromagnetic-field solvers. Termination circuits are not restricted to be linear or passive. Any termination that can be modelled with a SPICE-like network-analyser computer program can be included in the analysis.

1.4 Objectives

The objective of this thesis is the development of efficient computational techniques for:

- Modelling automotive glass antennas and the interaction of these antennas with cables
- Simulation of crosstalk, signal integrity, radiation and susceptibility problems in complex cable-harness systems, embedded into a 3D environment
- Modelling high-voltage cables used in power electronics and in electrical vehicles
- Modelling low-frequency magnetic fields in the presence of thin material sheets

Finally, the work presented in this thesis enables accurate prediction of the coupling between components of electromagnetic interference filters for power electronics applications.

1.5 Outline

This thesis is organised in the following chapters:

CHAPTER 1 gives a detailed description of an method-of-moments-based approach that is appropriate for glass-antenna modelling. Three method-of-moments-based approaches on different configurations are validated. For each problem the measurement range, test setup, parameters of the setup, simulation models and comparisons of results are provided. The problems that are considered range from very simple to more complicated in order to take into account different components and to investigate their contributions as well as to evaluate the applicability of the considered methods for modelling complex setups.

CHAPTER 2 presents a cable-harness model.

CHAPTER 3 details a computationally efficient method for solving automotive low-frequency electromagnetic compatibility problems by using integral equations. Interaction of magnetic fields with thin, finite, conducting 3D metallic structures is considered, obtaining the fields radiated by these structures by using single- and double-layer equivalent currents. This numerical electromagnetic solution is validated against semi-analytical solutions and measured data, and its applicability is illustrated by analysing three practical automotive problems.

CHAPTER 4 is devoted to modelling high-voltage filters.

CHAPTER 1

MODELLING OF AM AND FM/TV GLASS ANTENNAS IN AUTOMOBILES

1.1 Automotive Antenna Overview: Design and Placement

The number of radio services and communication systems offered in the automotive field has expanded greatly in recent years; indeed, contemporary vehicles contain over twenty services that rely on wireless communication [9], [17], [10]. Entertainment systems that began with simple amplitude modulation (AM) radio rapidly expanded to include frequency modulation (FM) and television (TV) broadcast services. A number of current broadcasting systems use digital rather than analogue modulation schemes, such as digital audio broadcasting (DAB) or digital video broadcasting (DVB) systems, which are modern in-car entertainment broadcasting formats for both radio and video. Satellite digital audio radio services (Sirius and XM radio) allow broadcasting across a much wider geographical area than can be reached by terrestrial radio stations. Communication and information services that were initially available only in luxury vehicles are now available in mass-produced vehicles; such services include universal mobile communication system (UMTS), global system for mobile communication (GSM), bluetooth and global positioning system (GPS). Comfort and safety systems such as central door locking, remote key-less entry (RKE) and go systems, tyre pressure monitoring system (TPMS) and collision avoidance radar also utilise wireless communication technology. Finally, car-to-car and car-to-infrastructure communication systems are both subject to much research and development by leading car manufacturers; these intelligent technologies are intended to enhance not only safety and comfort but also driving efficiency.

Modern vehicles are fitted with multiple antennas in order to facilitate communication and operation of the aforementioned services at different frequency bands; up to 25 antennas are used currently and it is expected that this number will increase in the future. Operation frequencies span from low frequencies (LF) (for RKE and Go systems) to millimetre waves (MMW) (for anti-collision radar systems). Carrier frequencies for AM radio are located in the 500 to 1700 kHz band. Some systems require the use of multiple antennas; for example, TV services, which operate in different bands starting from 40 MHz up to 800 MHz, or FM radio services, which

operate from 75 MHz up to 109 MHz, use two or even three antennas (antenna diversity system) to achieve stable reception characteristics. Differences in the frequency range for different countries should be taken into account; for example, RKE systems operate at 433 MHz within Europe and at 315 MHz in Japan and the USA.

Since an antenna is a key part of radio transmission and reception, its design and placement has a significant affect on communication performance. In order to ensure good communication quality, a number of requirements regarding antenna placement should be fulfilled [18].

- Antenna must be unobstructed and placed as high as possible above the ground.
- Coupling with metallic objects and other antennas should be minimal.
- Distance to receivers (cable-length) should be minimised.
- Distance to spurious emissions should be maximised.
- Ground plane of antenna should be sufficiently large.

Antennas can be placed at many positions both outside and inside the vehicle, but not all positions are ideal. In order to determine whether an antenna position is good, it is necessary to consider the selected service, frequency band and antenna technology collectively. Finding an appropriate antenna structure can help to overcome problems and achieve a satisfactory compromise between antenna position and performance.

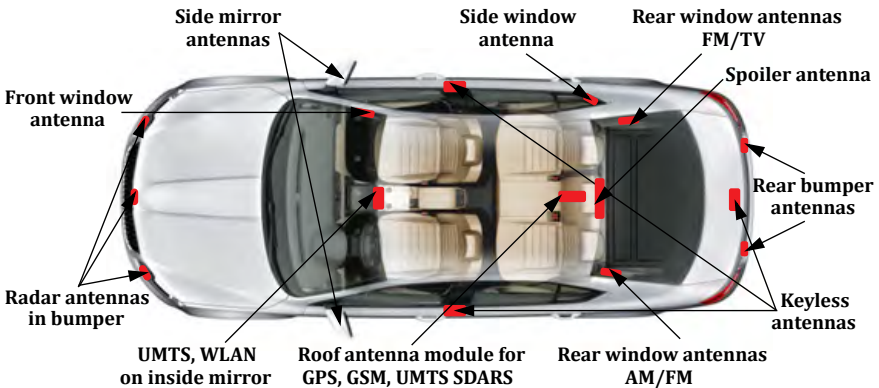


Fig. 4. Typical locations for antenna systems

Fig. 4. illustrates typical locations that are utilised for mounting antennas on or inside modern vehicles.

Positions on the wing and boot are used typically for mounting monopole antennas for AM/FM radio and special services. Short helical AM/FM antennas can be mounted on

the vehicle roof (at the centre of the roof, at the edge or on the frame). The roof position is one of the best options because it is unobstructed and high above the ground, thus providing mostly omni-directional reception. While antenna parameters for a rooftop position are largely unaffected by car-body shape, the rooftop position is unsuitable for convertible vehicles. Since modern design rules prohibit the positioning of a rod antenna on a roof or wing, car designers avoid using simple rod antennas, especially for luxury cars; instead, car designers require that antennas are incorporated into the vehicle structure.

Very popular positions for printed-on-glass antennas for AM/FM/TV or DAB services are the side, rear or front windows; here, the antenna structure can be either on the glass or along the window frame. Most usually, antennas are placed at the rear window when the engine is at the front of the vehicle, offering the maximum distance from spurious emission noise. The front-window position is used mostly for convertible cars or when the engine is at the back of the vehicle. Alternatively, side windows can be used in estate cars. The glass itself is usually large enough to incorporate several antennas. Such design requires greater engineering efforts to determine a suitable structure because, in general, and despite a number of other advantages, passive glass-mounted antennas exhibit lower FM gains when compared to whip antennas. Critical advantages of passive glass-mounted antennas are that they are hidden, they have low noise levels under bad weather conditions and they are less vulnerable to damage. A typical printed antenna is constructed of conductive strips arranged on a glass mount. Since defrosting structures are normally placed on the rear window, the same conductors can be utilised for on-glass antennas by using a special filter to separate the DC component and noise interference from the radio signal. AM and FM antennas can be designed as two separate units, one for each frequency band; such design is typically used for quarter side-window antennas. Another alternative design technique for on-glass antennas follows a slot antenna principle whereby the metallic car structure becomes part of the antenna and the glass is used as the slot. Coupling this slot with a thin conductor, the slot resonates and can be used as an antenna. When an appropriate feeding position is used, different modes of the required polarisation and radiation behaviour can be excited. This antenna design can be useful for antennas integrated into the front windscreen.

When GPS, SDARS, satellite TV and cellular phone antennas are integrated into a single antenna unit, they are also usually mounted on the roof or on the car boot lid, especially for convertible vehicles. A classical GPS antenna is realised as a microstrip (patch) antenna. According to the requirements, an antenna should be designed to operate at 1575 MHz +/- 2 MHz. A GPS antenna can be combined with a SDARS antenna operating at 2300 MHz, thus allowing the size of the multi-frequency antenna unit to be reduced. The antenna includes two coplanar patches that are not in physical contact and requires a large metallic ground structure, preferably flat, of minimum $1 * \lambda$

around it. In some circumstances GPS/SDARS antennas can be positioned in exposed spoilers or mirror housing.

Some sport and regular hatchback cars have a plastic spoiler to improve the downward force at higher speeds; such spoilers can be used to incorporate hidden/integrated antennas for digital sound and TV broadcasting, GPS, SDARS, telephone and, most recently, car-to-car communication. Compared to regular cars, light trucks and sport utility vehicles (SUV) have large side mirrors that can accommodate a number of high-frequency antennas. The side mirrors of some trucks are large enough to incorporate FM-receiving antennas at the VHF band, telephone antennas for GSM and UMTS systems, GPS navigation and SDARS satellite broadcasting antennas.

Foil and fractal antennas, which are mounted on metallic foil and glued to plastic elements, are common for mobile telephone antennas, car-entry systems and Bluetooth/WLAN antennas. The possible geometries that can be used for these very flat structures is virtually unlimited and they can be placed in rear-view mirrors, side mirrors, spoilers, bumpers and wings.

Antennas for short-range wireless communication devices are usually mounted out of sight, inside the car; for example, under the car front panel or in the interior of a door or boot (in particular, low-frequency magnetic antennas for RKE and Go systems and antennas for remote start engine (RSE)).

Radar collision antennas are mounted into front bumper structures. Two common systems are long-range radar (LRR) and short-range radar (SRR). LRR operates at 77 GHz and has a resolution of approximately 3 m at distance of 150 m [19]. An example of a front bumper system with LRR radar is adaptive cruise control (ACC), which controls the driving path in front of the car in order to maintain the minimum safety distance relative to the vehicle in front. The antenna system includes two separate antennas: one to transmit and the other to receive. Each antenna is comprised of a microstrip slot-coupled antenna array. The SRR system operates at 24 GHz with 4 to 5 GHz frequency bandwidth and a range of less than 30 m. The SRR system is used to reduce side, rear and front blind spots and to provide other safety enhancements.

As already discussed above, a sophisticated design of antenna pattern is needed for efficient performance of printed-on-glass antennas. High-quality antenna designs require comprehensive theoretical simulations and prototype measurements. Many patents and academic papers are devoted to these studies [20] - [29].

1.2 Method of Moments (MoM) for the Solution of Automotive Antenna Problems

There are many contemporary numerical techniques for modelling antenna and electromagnetic compatibility (EMC) problems; each technique is best suited for the analysis of a particular antenna configuration. However, taking into consideration the complexity of the antenna systems together with the associated electronic modules, as well as the variety of their components and electromagnetic (EM) sources, no single technique can be used in its traditional formulation to model all of the structural features of antenna systems and their interactions with other electronic systems. Therefore, a suitable combination of traditional and specialised methods and techniques, including adaptive and hybrid techniques, is required.

Based on recent enhancements of the traditional method of moments (MoM) [11], this work proposes a set of advanced methods and special means [30] - [36] that provide an accurate and effective simulation of EM/EMC automotive antenna problems.

1.2.1 Traditional MoM

The MoM (or moment method) is a technique for solving complex integral equations by reducing them to a system of more simple linear equations. In contrast to the variational approach of the finite-element method however, MoM employs a technique known as the method of weighted residuals. As a matter of fact, the terms 'MoM' and 'method-of-weighted-residuals' are synonymous. R.F. Harrington [11] was largely responsible for popularising the term MoM in the field of electrical engineering, when his pioneering efforts first demonstrated the power and flexibility of this numerical technique for solving problems in electromagnetics.

The equation solved by MoM techniques is generally a form of the electric field integral equation (EFIE) or the magnetic field integral equation (MFIE); both equations can be derived from Maxwell's equations by considering the problem of a field scattered by a perfect conductor (or a lossless dielectric). The equations are of the form:

$$EFIE : \vec{E} = f_e(\vec{J}) \quad (1)$$

$$MFIE : \vec{H} = f_m(\vec{J}) \quad (2)$$

where the terms on the left-hand side of these equations are incident field quantities and \vec{J} is the induced current.

As already known, an arbitrary boundary-value EM problem on geometry G may be written in operator form as (3):

$$L(\vec{J}) = \vec{g} \quad (3)$$

where L is an integro-differential operator, \vec{g} is the excitation, and \vec{J} is the unknown current density on G . Furthermore, we discretise G to consider the following expansion for the unknown current:

$$\vec{J}(\vec{r}') = \sum_{n=1}^N I_n \vec{f}_n(\vec{r}'), \quad (4)$$

where $\{\vec{f}_n(\vec{r}')\}_{n=1}^N$ are the sub-domain expansion functions, I_n are unknown coefficients, and N is the total number of unknowns. Substituting (4) into (3) and applying a testing procedure with weighting functions $\{\vec{w}_m(\vec{r}')\}_{m=1}^N$ defined in the range of L leads to a linear set of equations written in matrix form:

$$[Z_{mn}][I_n] = [V_m], \quad (5)$$

where $[Z_{mn}]$ and $[V_m]$ are, respectively, the MoM impedance matrix and voltage matrix-vector with elements $Z_{mn} = \langle \vec{w}_m, L\vec{f}_n \rangle$ and $V_m = \langle \vec{w}_m, \vec{g} \rangle$, and $[I_n]$ is the vector of unknown coefficients in the current expansion (4).

1.3 Modelling of Automotive Glass Antennas Using Hybridisation of MoM with a Special Green's Function

This section describes an equivalent model of layered antenna structures based on the refined modified image theory and derives the hybrid MoM scheme, which incorporates the approximate Green's function of such a model. Validation of the model is done by comparison of the measured and simulated antenna characteristics for a number of special simplified examples. Application of the technique is demonstrated for a solution of antenna design problems with a real complex windshield, side window antennas and car body.

1.3.1 Problem Formulation

As already discussed, automotive design tends towards conformal and hidden antenna applications, such as glass antennas integrated in vehicle windows, as depicted in Fig. 5.

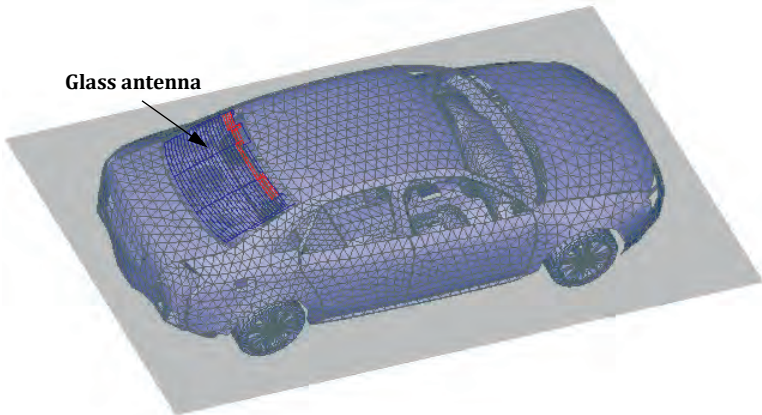


Fig. 5. Computational models of vehicle with glass antenna in the rear window

An accurate analysis of vehicle glass antennas requires a proper discretisation of not only the metallic elements, but also the dielectric substrate of glass antennas. Applying the typical finite-element method (FEM)/MoM approach to such a mesh results in an excessively large number of unknowns (a few hundreds of thousands). As a result, some studies of vehicle glass antennas [28] - [29] neglect the window glazing so that only far-field calculations are performed. To account for the dielectric effect of the glass on vehicle EMC characteristics, most studies [40] - [42] utilise a sheet impedance approximation [43], which is available in many EM solvers such as [44] - [46]. Although such an approach is efficient, it is not sufficiently accurate for complex glass-

antenna geometries and the substrate still requires discretisation, although the discretisation is appreciably less fine.

The discretisation of the substrate can be avoided when the curvature of the glass and impact of the main vehicle geometry is ignored by applying the appropriate Green's functions for infinite layered structures [47] - [50]. However, the rigorous Green's functions represented by Sommerfeld integrals [51] are, unfortunately, too time-consuming to calculate and too inflexible to be incorporated in the full vehicle geometry. To overcome this problem, a number of studies [52] - [54] have been performed to approximate the Sommerfeld integrals. Alternative studies propose different approximate image theories, such as complex image theory (CIT) [55] - [58] and modified image theory (MIT) [59] - [63], and others suggest different equivalent models of layered structures [64] - [67]. However, the majority of such theories and models are suited only to simple layered geometries and are insufficiently flexible to be hybridised with the full vehicle geometry.

A new simple but accurate and flexible equivalent glass-antenna model is reported in [68]. It is based on the image concept; image amplitudes are expressed through those for the dielectric interface problem and found by refining the MIT [62] - [63]. In [69] - [70], this model is hybridised with the main vehicle geometry.

1.3.2 Theoretical Approach

The described traditional MoM procedure described in Section 1.2.1 requires discretisation of all parts of the geometry, including the dielectric substrate. In order to exclude the dielectric from the formulation, we should modify the boundary operator L and excitation \vec{g} in the glass area in such a way as to account for the effect of the dielectric and to automatically satisfy the boundary conditions on the dielectric.

The first aim is to find the modified boundary operator and excitation in the glass area by introducing the equivalent glass-antenna model. The next aim is to incorporate an approximate Green's function of the equivalent model in a full MoM matrix in order to apply the hybrid MoM scheme for the analysis of finite-size and curved glass-antenna structures integrated into the full vehicle geometry. Finally, this approach is validated.

Equivalent Glass Antenna Model

Fig. 6. (a) shows an original structure of the metallic strip (glass-antenna element) A with current \vec{J} placed above, inside or under the dielectric layer (regions $i = 1, 2, 3$, respectively). The layer of thickness l and material parameters ϵ, μ (region $i = 2$) is placed in vacuum with parameters ϵ_0, μ_0 ($i = 1, 3$). In a multilayer case, effective medium parameters are considered.

Fig. 6. (b) shows the equivalent model of the microstrip structure of Fig. 6. (a), consisting of the source current \vec{J} on element A and its mirror images \vec{J}_k ($k = 0, \pm 1, \pm 2, \dots$) in the upper and lower dielectric-layer interfaces.

For the source current \vec{J} in region i , the electromagnetic field at the observation region $j = 1, 2, 3$ is composed of the field of the original current \vec{J} (only if $j = i$) and that produced by its images \vec{J}_k with amplitudes A_{kv}^{ji} and A_{kh}^{ji} for the vertical and horizontal components of the vector potentials, and A_{kq}^{ji} for the scalar potentials. Hereinafter, the first superscript in amplitude notations indicates the observation region and the second superscript indicates the source region.

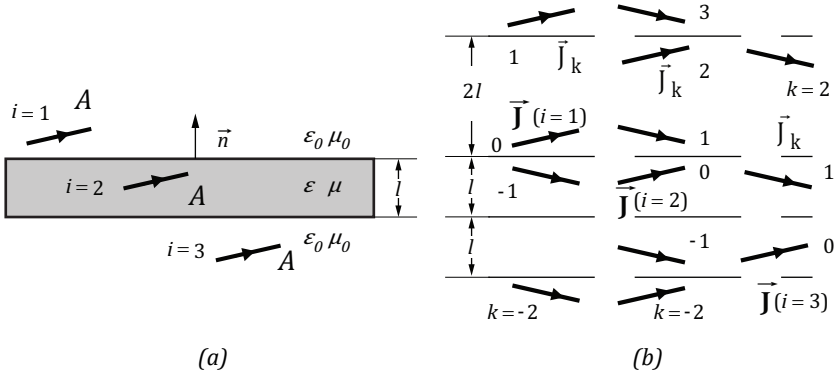


Fig. 6. Original (a) and equivalent (b) glass-antenna models

Note that both the source and image currents radiate in the medium with the material properties of the observation region j . Meanwhile, only image currents, which are not situated in the observation region, radiate into this region.

The suggested model requires finding the image amplitudes by ensuring the boundary conditions on both dielectric interfaces. This can be done by recursively applying the mirror-image method to relate these amplitudes to those obtained for the approximate solution of the boundary-value problem on a separate dielectric interface. In the next subsection we will refine the MIT [62] - [63] in order to reconsider the dielectric half-space problem in a quasi-static approximation. Furthermore, we will derive the image amplitudes A_{kt}^{ji} ($t = v, h, q$).

Refined Modified Image Theory

Consider the interface between two dielectric media m and i characterised by material parameters ϵ_m, μ_m and ϵ_i, μ_i , respectively, as depicted in Fig. 7. (a). Let the current \vec{J} and charge $q = \mp \frac{1}{i\omega} \text{div} \vec{J} dV$ associated with the elementary electric dipole of volume dV exist in one of two media, say medium i , as depicted in Fig. 7. (a). We are interested in the calculation of the EM field due to these sources at the observation points from both sides of the interface.

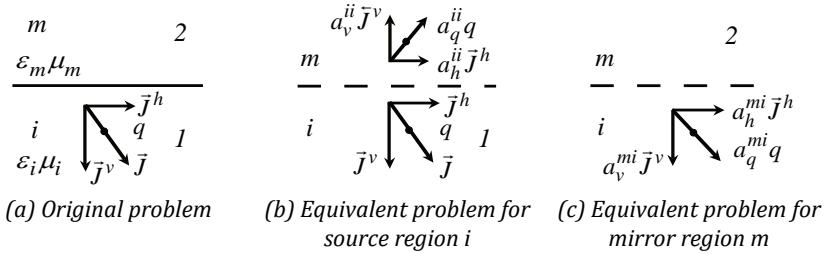


Fig. 7. Sources and images in the presence of dielectric interface

The above problem can be solved accurately in terms of Sommerfeld integrals. However, in order to determine the approximate field at both the source region i and the mirror region m , we take advantage of the MIT [59] - [63], extending the canonical mirror-image method to the dielectric half-space problem. Following the MIT, the EM response from the imperfect interface is described approximately by inserting the mirror-image source radiating to the source region i , and the space-like image source radiating to the mirror region m ; see Fig. 7. (b) and (c), where the original current \vec{J} is decomposed into its vertical \vec{J}^v and horizontal \vec{J}^h components, and $\vec{J}^v = -\vec{J}^v$. Unlike the canonical mirror-image method, the image amplitudes a_t^{ji} ($t = v, h, q$) are modified so as to approximately satisfy the boundary conditions (whence the method's name). The variants of the MIT [59] - [63] differ by the method of finding the image amplitudes.

The traditional MIT [59] - [61], also known as the reflection-coefficient method (RCM), utilises the far-field plane-wave approximation for image amplitudes. Its solution is, therefore, valid only at distances that are rather far ($kR \gg 1$) from the boundary surface, where k is the wavenumber and R is the distance between the image and observation points. In contrast, the simplified MIT [62] - [63] is obtained in the electrostatic approximation $kR \ll 1$ and does not consider the boundary conditions for the magnetic field. Thus, the obtained image coefficients are fully valid only for the charge problem, and the current images are approximately valid in the source region

for the vertical-dipole problem, but fully invalid for the horizontal-dipole problem. Therefore, it is necessary to reconsider the latter problem.

In order to find the unknown image amplitudes a_t^{ji} ($t = v, h, q$), we impose the boundary conditions on both the electric field $\vec{E}^j = -i\omega\vec{A}^j - \nabla\Phi^j$ and the magnetic field $\vec{H}^j = \frac{1}{\mu_j}\nabla\times\vec{A}^j$ ($j = i, m$) due to all sources in their radiation domain, considered in the quasi-static approximation $(kR)^2 \ll 1$. The electric field is expressed by means of the sources of both vector and scalar potentials, i.e. the currents and charges, while the magnetic field is expressed by means of the sources of only the vector potential, i.e. the currents.

Imposing the boundary conditions for the same amplitudes of the current and charge images leads to an inconsistent set of equations for the image amplitudes. However, we are at liberty to assign different amplitudes a_v^{ji} and a_h^{ji} for the current images and a_q^{ji} for the charge images, in view of the non-uniqueness of the vector and scalar potentials in the presence of a dielectric boundary [71] - [72]. Furthermore, we consider the vertical- and horizontal-dipole problems separately, as in the traditional Sommerfeld solution. Consequently, we obtain the following set of equations for image amplitudes:

$$\frac{1}{\varepsilon_i}(1+a_q^{ii}) = \frac{1}{\varepsilon_m}a_q^{mi}, \quad 1-a_q^{ii} = a_q^{mi} \quad (6a)$$

$$1-a_v^{ii} = a_v^{mi} \quad (6b)$$

$$1-a_h^{ii} = a_h^{mi}, \quad \mu_i(1+a_h^{ii}) = \mu_m a_h^{mi} \quad (6c)$$

Note that equation (6a) follows from the boundary conditions for the electric field, and equations (6b), (6c) for the magnetic field. Therefore, equation (6) defines an approximate electromagnetic solution of the Sommerfeld problem.

Analysis of equation (6) shows that the vertical-dipole problem has a unique solution only for the same amplitudes of the charge and current images: $a_v^{ji} = a_q^{ji}$. However, the horizontal-dipole problem cannot be solved, even approximately, for the same image amplitudes and it requires different amplitudes for various images. Now the solution of equation (6) is expressed as:

$$a_q^{ii} = a_v^{ii} = \frac{\varepsilon_i - \varepsilon_m}{\varepsilon_i + \varepsilon_m}, \quad a_q^{mi} = a_v^{mi} = \frac{2\varepsilon_m}{\varepsilon_i + \varepsilon_m} \quad (7a)$$

$$a_h^{ii} = \frac{\mu_m - \mu_i}{\mu_i + \mu_m}, \quad a_h^{mi} = \frac{2\mu_i}{\mu_i + \mu_m} \quad (7b)$$

Derivation of Image Amplitudes A_{kt}^{ji}

Once the image amplitudes a_t^{ji} of the equivalent interface problem of Fig. 7. (b) and (c) are found, a recursive procedure to derive the image amplitudes A_{kt}^{ji} of the equivalent glass-antenna problem of Fig. 6. (b) can be developed. In order to satisfy the boundary conditions on the upper dielectric interface in Fig. 6. (b), following the refined MIT above, we introduce, along with the source current \vec{J} radiating in the source region 1, two image currents situated at equal distances d from the interface: (i) the mirror current \vec{J}_{-1} with amplitude $A_{-1t}^{11} = a_t^{11}$ again radiating in region 1, and (ii) the space-like image \vec{J}_0 with amplitude $A_{0t}^{21} = a_t^{21}$ radiating in region 2.

To satisfy the boundary conditions on the lower interface we consider the radiation problem for the image current \vec{J}_0 with amplitude a_t^{21} in region 2 in the presence of the lower interface. This requires two additional image currents situated at equal distances $l \pm d$ from the lower interface: \vec{J}_{-2} with amplitude $A_{-2t}^{21} = a_t^{21} a_t^{22}$ radiating in region 2, and \vec{J}_0 with amplitude $A_{0t}^{31} = a_t^{21} a_t^{12}$ radiating in region 3.

Next, we should adjust the boundary conditions on the upper interface that is imbalanced due to the radiation of image current \vec{J}_{-2} with amplitude $a_t^{21} a_t^{22}$ in region 2 in the presence of the upper interface. This produces a pair of additional image currents situated at equal distances $2l \pm d$ from the upper interface: (i) the mirror image \vec{J}_{-1} with amplitude $A_{-1t}^{21} = a_t^{21} (a_t^{22})^2$ radiating in region 2, and (ii) \vec{J}_{-2} with amplitude $A_{-2t}^{11} = a_t^{21} a_t^{22} a_t^{12}$ radiating in region 1.

Furthermore, recursively applying the refined MIT results in the following amplitudes of image currents \vec{J}_k due to the source current \vec{J} in region $i = 1$:

$$A_{-1t}^{11} = a_t^{11}; A_{kt}^{11} = a_t^{21} a_t^{12} (a_t^{22})^{2k-3}, \quad k = 2, 3, \dots \quad (8a)$$

$$A_{-kt}^{21} = a_t^{21} (a_t^{22})^{2k-3}, \quad k = 2, 3, \dots \quad (8b)$$

$$A_{kt}^{21} = a_t^{21} (a_t^{22})^{2k}, \quad k = 0, 1, 2, \dots \quad (8c)$$

$$A_{kt}^{31} = a_t^{21} a_t^{12} (a_t^{22})^{2k}, \quad k = 0, 1, 2, \dots \quad (8d)$$

Similar formulae for the source current \vec{J} placed inside the layer ($i = 2$) are given in [70]. In the next section, these results will be validated by comparing them with the accurate Sommerfeld solution.

MoM Solution to the Equivalent Glass-Antenna Model

The equivalent glass-antenna model of Fig. 6. (b) allows us to write the equivalent current and charge (i.e. the divergence of current) associated with the antenna element A at any observation region $j = 1, 2, 3$ as

$$\vec{J}' = \vec{J} \delta_{ij} + \sum_k [A_{kv}^{ji} \vec{J}_k^v + A_{kh}^{ji} \vec{J}_k^h] \quad (9)$$

$$i/\omega \nabla \vec{J}' = i/\omega (\nabla \vec{J} \delta_{ij} + \sum_k A_{kq}^{ji} \nabla \vec{J}_k) \quad (9a)$$

where \vec{J} is the original current on element A in the i -th region, δ_{ij} is the Kronecker delta, $\vec{J}_k = \mathfrak{R}_k \vec{J}$ is the current on the k -th image, \mathfrak{R}_k is the imaging operator, $\vec{J}_k^v = (\vec{J}_k \cdot \hat{n}) \hat{n}$ and $\vec{J}_k^h = \vec{J}_k - \vec{J}_k^v$ are the vertical and horizontal components of the k -th image currents, respectively, and \hat{n} is the unit normal vector to the dielectric interface.

Equation (9) can be viewed as $\vec{J}' = \mathfrak{S}(\vec{J})$, where \mathfrak{S} is the transforming operator. Substituting (9) into (3) along with the modified excitation $\vec{g}' = \mathfrak{S}(\vec{g})$ leads to the following equivalent boundary-value problem on the antenna-element geometry:

$$L_G(\vec{J}) = \vec{g}_G \quad (10)$$

where

$$L_G = L \mathfrak{S}, \quad \vec{g}_G = \mathfrak{S} \vec{g} \quad (10a)$$

are the modified boundary operator and excitation in the glass area including the dielectric effect and automatically satisfying the boundary conditions on the dielectric interfaces.

Equation (10) allows application of the traditional MoM scheme to the equivalent model of Fig. 6. (b), with expansion functions taken on both the original and image geometry, and testing performed only on the original geometry.

Equation (10a) allows us to derive the hybrid MoM scheme with the finite-size glass-antenna model incorporated into the full MoM geometry.

Finite-size and Curved Glass-Antenna Models

Although the equivalent glass-antenna model of Fig. 6. (b) is derived for infinite dielectric layers, it may also be applied approximately to finite-size glass-antenna structures. Moreover, slightly curved glass-antenna geometries may be considered. For this purpose, the finite-size dielectric substrate is subdivided into separate areas, and each antenna element is associated with a nearby glass area. The antenna elements near that area are considered to radiate such as in the presence of an infinite dielectric substrate being the extension of this glass area.

Hybrid MoM Scheme

In order to incorporate the equivalent glass-antenna model into the full MoM geometry, we divide the full geometry into the basis, e.g. vehicle geometry B , and glass-antenna element geometry A , and modify the boundary operator and excitation on A such as to include the dielectric effect. Thereby, we reduce the boundary-value problem (3) to the following set:

$$L(\vec{J}^B) + L_G(\vec{J}^A) = \vec{g}^B + \vec{g}_G^A \quad \text{on } S^B \quad (11a)$$

$$L_G(\vec{J}^B) + L_G(\vec{J}^A) = \vec{g}_G^B + \vec{g}_G^A \quad \text{on } S^A \quad (11b)$$

where L_G and \vec{g}_G are the modified boundary operator and excitation defined by (10a), and the superscripts B and A stand for the basis and glass-antenna elements, respectively. The set (9) represents the hybrid MoM formulation of the problem to be solved.

Next, applying the traditional MoM scheme with expansion functions $\{\vec{f}_n(\vec{r}')\}_{n=1}^N$ and weighting functions $\{\vec{w}_m(\vec{r})\}_{m=1}^N$, with $N = N^A + N^B$, to (11) leads to the following set of linear algebraic equations written in block-matrix form as

$$\begin{bmatrix} [Z_{mn}^{BB}] & [Z_{mn}^{BA}] \\ [Z_{mn}^{AB}] & [Z_{mn}^{AA}] \end{bmatrix} \begin{bmatrix} [I_n^B] \\ [I_n^A] \end{bmatrix} = \begin{bmatrix} [V_m^{BB}] + [V_m'^{BA}] \\ [V_m'^{AB}] + [V_m'^{AA}] \end{bmatrix} \quad (12)$$

with MoM impedance matrix elements $Z_{mn}^{BB} = \langle \vec{w}_m^B, L \vec{f}_n^B \rangle$, $Z_{mn}^{\beta\alpha} = \langle \vec{w}_m^\beta, L_G \vec{f}_n^\alpha \rangle$, excitation elements $V_m^{BB} = \langle \vec{w}_m^B, \vec{g}^B \rangle$, $V_m^{\beta\alpha} = \langle \vec{w}_m^\beta, \vec{g}_G^\alpha \rangle$, and $\alpha, \beta = \{A, B\}$.

The linear set (12) incorporates the equivalent glass-antenna model into the full MoM geometry and, therefore, accounts properly for the dielectric effect on glass-antenna elements.

1.4 Validation of the Hybrid MoM Scheme with a Special Green's Function

The hybrid MoM scheme utilising a Green's function approach was validated on a number of models by comparing simulation results with those obtained by measurements and calculated using the previous modelling techniques: a sheet- or surface-impedance approach [38] and a coated-wire approach [39]. All simulations were performed using the MoM-based program "TriD" included in the program package "EMC Studio" [1].

1.4.1 Simple Grid Antenna on a Thin Glass

Fig.8. shows the two measurement setups for a simple grid antenna printed on a thin glass: (a) without a frame, and (b) with a metallic frame to emulate the fixing of glass in the automobile window. The glass antenna consists of five metallic strips printed on a dielectric substrate that is elevated over the metallic plate. The two antenna terminals are connected to a network analyser via BNC connectors, the outputs of which are considered as ports. The quantity of interest is the reflection coefficient at Port 1.

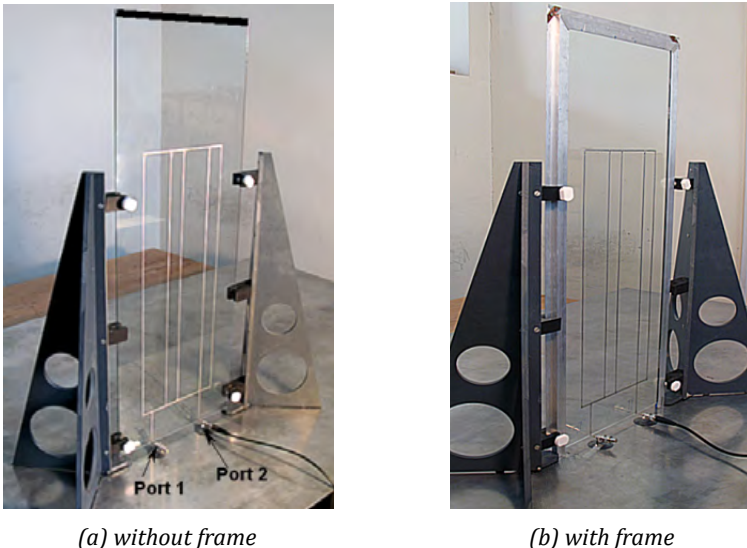


Fig. 8. Measurement setups for a simple grid antenna on a thin glass

The parameters of the measurement setup are as follows. The metallic strips of the glass antenna have width $w = 2$ mm, grid height $h = 500$ to 570 mm, and the minimum separation between the strips is $t = 30$ mm.

The dielectric substrate has width $W = 290$ mm, height $H = 800$ mm, thickness $l = 3$ mm, elevation over the plate $hd = 10$ mm, relative permittivity of the glass $\epsilon_r = 6.6$, and loss tangent $\tan(\delta) = 0.02$. The metallic frame has width $wf = 20$ mm, and the plate dimensions are $1 \text{ m} \times 2 \text{ m}$.

The simulation model of the measurement setup for the Green's function approach consists of glass triangular antenna elements (triangles printed on the glass) to model the glass antenna, metal triangles to model the metallic plate and wire segments to model the antenna ports. BNC connectors are modelled as non-radiating transmission-line elements. Antenna Port 1 is active and excited by a lumped voltage source with a 50Ω series resistance to match the characteristic impedance of the transmission line. Antenna Port 2 is passive and loaded by a similar resistance.

The simulation model for the surface-impedance approach consists of metallic triangles, representing the actual antenna, and triangles with appropriate surface impedance [38] to model the glass. For the coated wire approach, the strips of the glass antenna are replaced by wire segments with an appropriate equivalent coating [39]. When using this approach, dielectric losses in the glass are neglected.

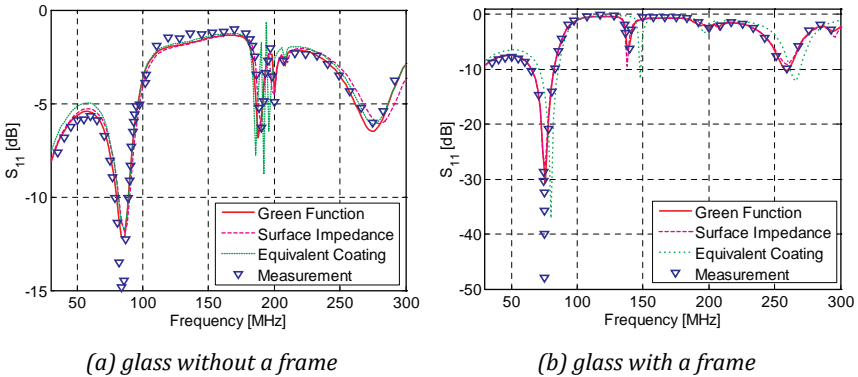


Fig. 9. Comparison between the simulation and measurement results

Fig. 9. (a) and (b) present a comparison between the simulation and measurement results for both measurement setups. This comparison shows that the simulation results obtained by different simulation methods agree well with the measured data up to a frequency of 300 MHz. Meanwhile, the Green's function results are closer to this data for both measurement setups. The surface-impedance approach reveals a slight shift of higher frequency resonances when the glass is without a frame. The coated-wire approach displays superfluous oscillations near the resonance at around 190 MHz when the glass is without a frame, and a shift of resonances when the glass is in the metallic frame. These discrepancies may be explained by a poor accounting of the

dielectric effect for the surface-impedance approach, and by neglecting the dielectric losses and mutual coupling between the strips for the coated-wire approach.

1.4.2 Complex Grid Glass Antenna

A validation setup, shown in Fig. 10. , has been developed to check the accuracy of the numerical approach for grids with high density. The two antenna terminals are connected to the network analyser via BNC connectors, the outputs of which are considered as ports. The reflection coefficient at each port and the transmission coefficient between the ports was measured.

A schematic representation of the measurement setup with the dimensions of the constituent elements is depicted in Fig. 11. The metallic strips of the antenna have width $w = 2$ mm and length $L = 510$ mm. The dielectric substrate has width $W = 290$ mm, height $H = 800$ mm, thickness $l = 6$ mm, relative permittivity $\epsilon_r = 6.6$ and loss tangent $\tan(\delta) = 0.02$. The dimensions of the metallic plate are 1 m x 2 m.

The simulation model of the measurement setup consists of 405 glass triangular antenna elements (triangles printed on the glass) to model the glass antenna, 18 wire segments to model the antenna ports and 1,082 metal triangles to model the metallic plate, on which the antenna is mounted, giving a total of $N = 2,018$ unknowns. The metallic elements are assumed to be perfectly conducting.

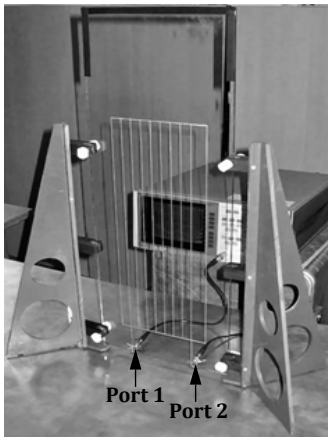


Fig. 10. View of the measurement setup for complex grid antenna

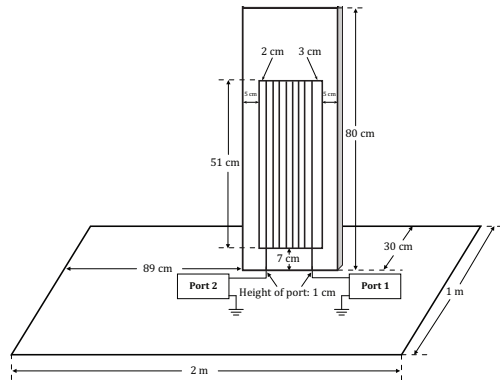


Fig. 11. Schematic representation of the measurement setup

In order to model the connectors at the antenna terminals, network transmission-line elements of 22 mm length and characteristic impedance 50Ω are used. One of the antenna ports is considered to be active and excited by a lumped voltage source with a

series resistance of 50Ω . The other antenna port is passive and terminated by the same resistance. Furthermore, the active and passive ports are swapped to simulate the complete scattering matrix.

Fig. 12. shows the comparison between the simulation and measurement results as well as the simulations performed without the dielectric (glass). The comparison of the simulation results with and without the dielectric shows that neglecting the dielectric effect leads to a considerable shifting and distortion of resonances and, thus, is no longer acceptable starting from frequencies of around 30 MHz.

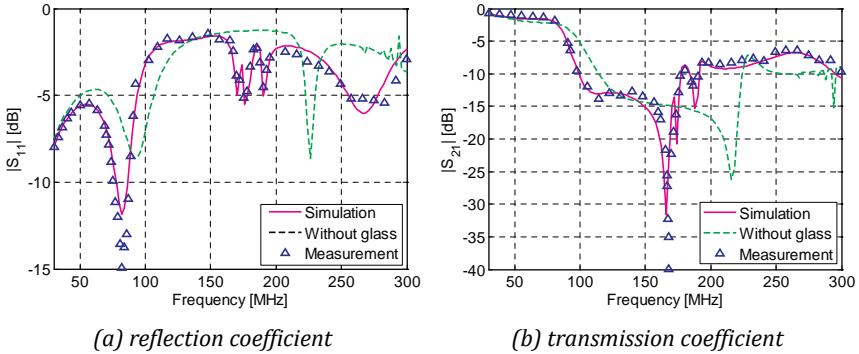


Fig. 12. Comparison of the measurement and simulation results for complex grid antenna

The comparison between the simulation and measurement results with the glass included shows a good agreement in a wide frequency range from 30 to 300 MHz. Specifically, these results show a very good prediction of the location and maxima of all resonances. A slight deviation between the compared results in resonance minima and discrepancies at higher frequencies may be caused by some uncertainty of the measurement setup and imperfection of the simulation model.

1.4.3 Automotive Windshield Glass Antenna

In order to validate the method for a realistic antenna, input impedance of a rear-window automobile glass antenna was measured and simulated. Fig. 13. shows the measurement setup consisting of a glass antenna with dimensions 1.19×0.77 m, strip width $w = 0.3$ mm, glass thickness $l = 3.45$ mm, glass permittivity $\epsilon_r = 7.5$ and loss tangent $\tan(\delta) = 0.02$, which is placed over a metallic plate of dimensions $1 \text{ m} \times 2 \text{ m}$. The quantity of interest is the reflection coefficient at the FM antenna port.

The comparison between the simulation and measurement results for this setup is shown in Fig. 14. It can be seen that the Green's function approach correctly describes the frequency behaviour of the reflection coefficient, so that the simulation results

agree well with the measured data. Results obtained using the surface-impedance and coated-wire approaches differ noticeably from the measured data, revealing the significant shift of resonances. Thus, this comparison shows a considerable advantage of the Green's function approach over other approaches for modelling integrated glass antennas.

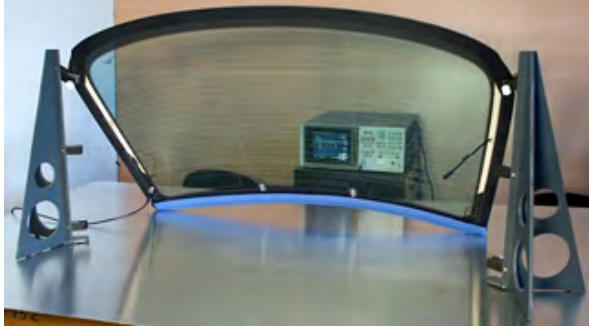


Fig. 13. Measurement setup for a rear-window automobile glass antenna

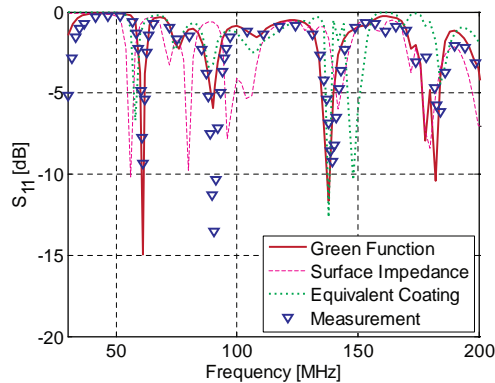


Fig. 14. Comparison between the simulation and measurement results

1.5 Application of Hybrid MoM Scheme for the Design of Automotive Glass Antennas

1.5.1 Complete Car Model with Windshield Antenna

The derived hybrid MoM scheme has been applied to simulate the reflection coefficient of the rear-window glass antenna in a complete model of a car. Simulation results were compared with measured data.

A simulation model of the measurement setup with a glass antenna and its AM/FM1/TV1 port is shown in Fig. 15. This model consists of 19,052 metal triangles to model the car bodyshell, 67 wire segments to model the antenna-to-body connections, and 2,477 triangles to model the glass antenna elements, giving a total of $N = 31,028$ unknowns. The curved glass surface is represented by 5,210 triangles. The dielectric substrate has thickness $l = 3.14$ mm, relative permittivity $\epsilon_r = 7.5$, and dielectric loss tangent $\tan(\delta) = 0.02$. The metallic elements are assumed to be perfectly conducting. In order to represent the measurement setup accurately, the BNC connectors attached to the antenna terminals are modelled as non-radiating TL elements of length 64 mm and having a characteristic impedance of 50Ω .

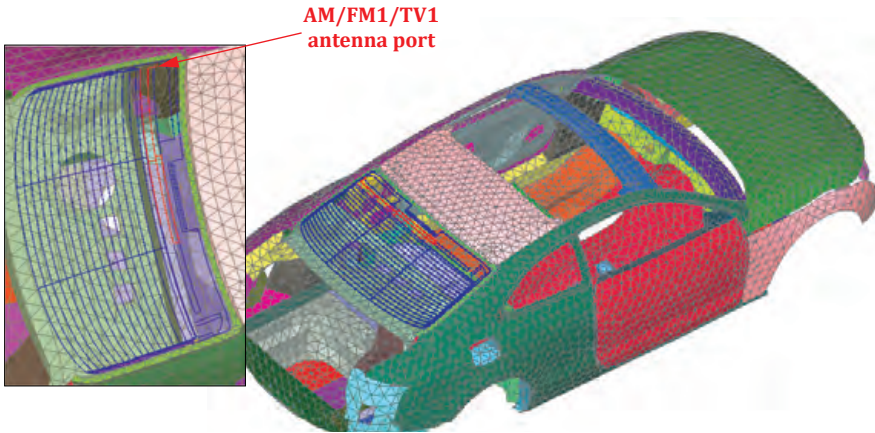


Fig. 15. Simulation model of measurement setup with a glass antenna and its FM port

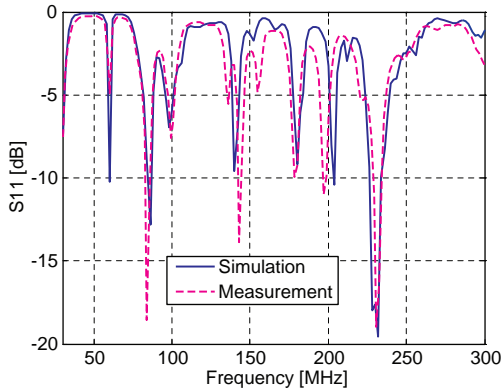


Fig. 16. Comparison of measurement and simulation results for a complete car model

Fig. 16. shows measurement and simulation results for the reflection coefficient $|S_{11}|$ at the FM1 port of the glass antenna. Comparison between these results shows that the simulation results are in close agreement with the measured data at all frequencies in the range 30 to 300 MHz.

1.5.2 Hybridisation of MoM with Multiport Networks

Incorporation of Network Equations in the MoM

Modern automotive antennas frequently involve a number of network devices ('black boxes'); in the context of MoM, a detailed analysis of such black-box network devices is impossible because of excessive computational intensity. This section describes a hybridisation of the MoM with general multiport networks specified through their network parameters, such as open-circuit impedances (Z-matrices), short-circuit admittances (Y-matrices), scattering parameters (S-matrices), transmission lines (TL) and so on.

Fig. 17. shows a general N-port network connected to the wire segments or ports of the MoM geometry. A network connection to ports 1, 2, ..., N forces the currents i_1, i_2, \dots, i_N through and voltages U_1, U_2, \dots, U_N over the ports, according to the network parameters of the considered network.

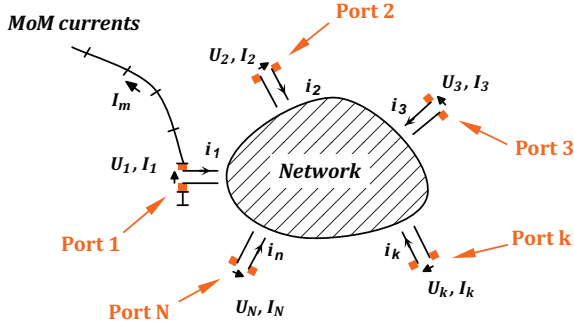


Fig. 17. N-port network directly connected to the MoM geometry

Network parameters can be introduced via different forms of network equations:

$$\mathbf{U} = \mathbf{Z}^{Net} \mathbf{i}, \quad (13a)$$

$$\mathbf{i} = \mathbf{Y}^{Net} \mathbf{U}, \quad (13b)$$

$$\mathbf{a}^- = \mathbf{S}^{Net} \mathbf{a}^+, \quad (13c)$$

where $\mathbf{i} = [i_1, i_2, \dots, i_N]$ and $\mathbf{U} = [U_1, U_2, \dots, U_N]$ are the network port current and voltage matrix-vectors, respectively. \mathbf{Z}^{Net} , \mathbf{Y}^{Net} and \mathbf{S}^{Net} are the network Z-, Y- and S-matrices with network parameters Z_{mn}^{Net} , Y_{mn}^{Net} and S_{mn}^{Net} , respectively. $\mathbf{a}^\pm = \frac{1}{2}(\bar{\mathbf{U}} \pm \bar{\mathbf{i}})$ are the

normalised incident (+) and reflected (-) port voltage vectors. $\bar{U} = Z_L^{-1/2} U$ and $\bar{i} = Z_L^{1/2} i$ are, respectively, the normalised network voltage and current vectors. Z_L is the diagonal matrix of the characteristic impedances $Z_{L_1}, Z_{L_2}, \dots, Z_{L_N}$ of the transmission lines connected to each port (reference impedances).

In order to incorporate the network equations (13a) to (13c) into the MoM system (5), it is necessary to relate the elements of the matrix-vectors V and I in (5) to the network port voltage and current matrix-vectors U and i . Let us choose the expansion and testing functions $\vec{f}_n(\vec{r}')$ and $\vec{w}_m(\vec{r}')$ in (4) and (5) so as to interpret V_m and I_n in (5) as segment currents and voltages. Then, the segment voltages $V = [V_1, V_2, \dots, V_N]$ can be shared between those caused by the external sources $V^S = [V_1^S, V_2^S, \dots, V_m^S, \dots]$ and those by the network voltages $U = [U_1, U_2, \dots, U_N]$:

$$V = V^S + U \quad (14)$$

For a free-port network (with controlled voltages), the port currents $i = [i_1, i_2, \dots, i_N]$ are easily related to the segment currents $I = [I_1, I_2, \dots, I_N]$:

$$i = -I \quad (15)$$

Therefore, inserting (15) into (13a) and then into (14) yields:

$$V = V^S - Z^{Net} I \quad (16)$$

Now, introducing (16) into (5) and regrouping the components with the currents I yields the following hybridised MoM and network algebraic system:

$$(Z^{MoM} + Z^{Net}) I = V^S \quad (17)$$

For the mixed (free and forcing) ports, the network equation (17) is generalised to:

$$(Z^{MoM} + Z'^{Net}) I = V^S + V^{add} \quad (18)$$

where $Z'^{Net} = (Y'^{Net})^{-1}$ is the free-port generalised impedance matrix of the N-port network,

$$V^{add} = -Z'^{Net} Y''^{Net} U^S \quad (19)$$

is an additional voltage matrix-vector on the free ports induced due to the connection to the forcing ports, and Y'^{Net} , Y''^{Net} are the free- and mixed-port generalised network admittance matrices, respectively. The latter are mixed matrices with the row index corresponding to the free port and the column index corresponding to the forcing port.

The matrix equations (18) represent the general hybridisation of the MoM with multiport networks. Here, the total impedance matrix is composed of the MoM matrix and a reduced general network matrix for free ports, while the voltage column is

composed of the MoM voltages and impressed network voltages, induced by the connection to the forcing ports. Specifically, for the free-port network, (18) reduces to (17), while for the forcing-port network, (18) reduces to (5), with $\mathbf{V} = \mathbf{V}^S$. In the latter case, the MoM system remains unchanged.

1.5.3 Application of Multiport Networks: Simulations of Vehicle Antenna Validation Tests

The developed techniques have been applied to simulate various EM and EMC problems on automotive antennas.

First, a vehicle antenna validation test (which usually precedes a chamber vehicle-emission test) is modelled [37].

A schematic representation of this test is shown in Fig. 18.

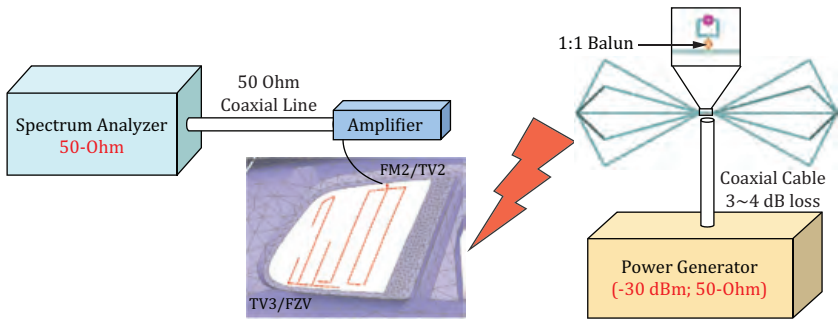


Fig. 18. Schematic representation of an antenna validation test

The measurement setup consists of an active vehicle antenna (with amplifier) exposed by a test antenna with defined feeding, and a spectrum analyser to measure the coupled voltage. The obtained voltage level is compared to the standard acceptable reception level, which is known for each type of vehicle antenna. The computer simulations are designed to predict the total antenna system performance in order to detect possible problems, especially if a physical vehicle prototype is not yet available for measurements. Fig. 19. shows the location of a car and a test antenna in an anechoic chamber, which was used in this study.

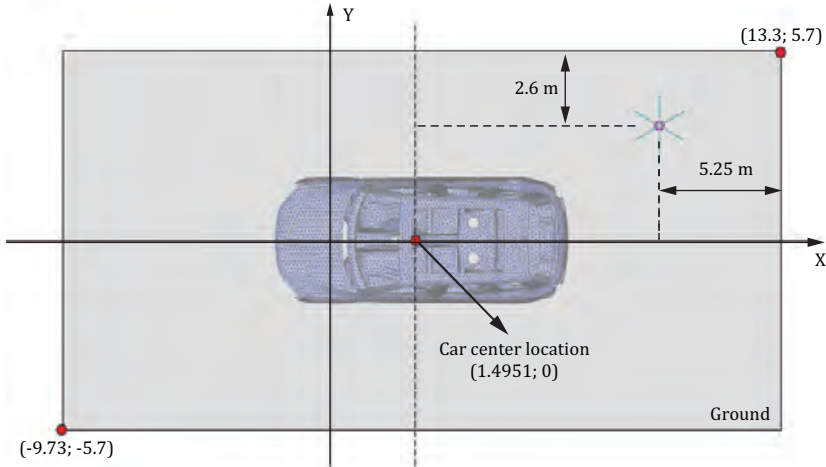


Fig. 19. Location of a car and a test antenna in an anechoic chamber

In the current example, a vertically polarised biconical Schwarzbeck BBA9106 test antenna, with 1:1 balun, is used. The antenna, which is located at 1.0 m above the ground, is fed by a -30 dBmW generator with 50Ω internal resistance, using a lossy coaxial cable. The dimensions and the antenna factor of the test antenna are presented in Fig. 20. and Fig. 21.

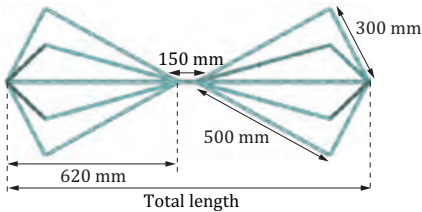


Fig. 20. Test antenna dimensions

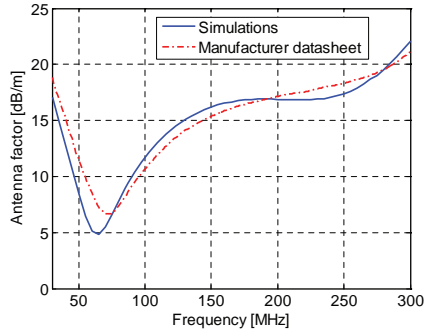


Fig. 21. Antenna factor

A simulation model of the side-window TV2 antenna in a Volkswagen car is shown in Fig. 22. The car bodyshell is modelled by 31,045 triangles and the antenna pattern is modelled by 535 triangles and 19 wire segments. The antenna pattern is printed onto a right-window glass of thickness $l = 3$ mm, permittivity $\epsilon_r = 7$, loss tangent $\tan(\delta) = 0.02$, which is adjacent to the TV3/FZV antenna.

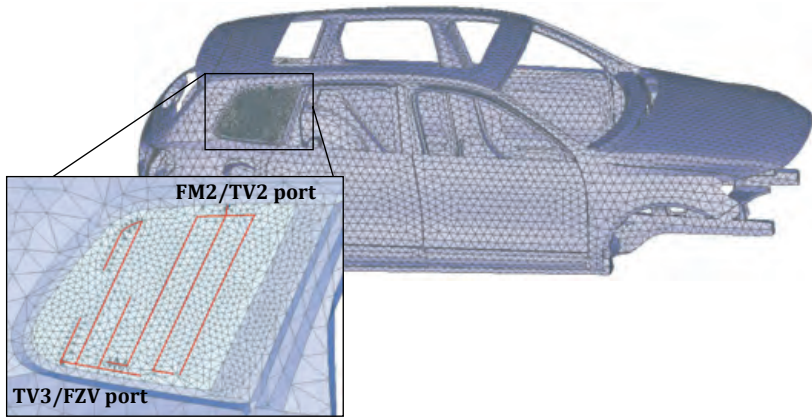


Fig. 22. Volkswagen car model with a glass antenna in the right window

In order to properly characterise the validation test, antenna amplifiers are also included in the simulation model as non-radiating networks. The scattering parameters of the TV2 and TV3 antenna amplifiers are depicted in Fig. 23. (a) and (b). It is assumed that any backward transmission of the signal from the radio to the antenna is negligible and that the amplifier output is perfectly matched to a 50 Ω coaxial cable that is connected to the radio. Thus, a complete simulation model consists of a biconical test antenna, a car bodyshell model and a side-window glass antenna with an amplifier. Analysis of such a model requires application of the following modelling techniques: power normalisation of the biconical antenna source, hybridisation of the MoM with the special Green's function to model the glass antenna, and hybridisation of the MoM with multiport networks to model the amplifiers and lossy coaxial cables.

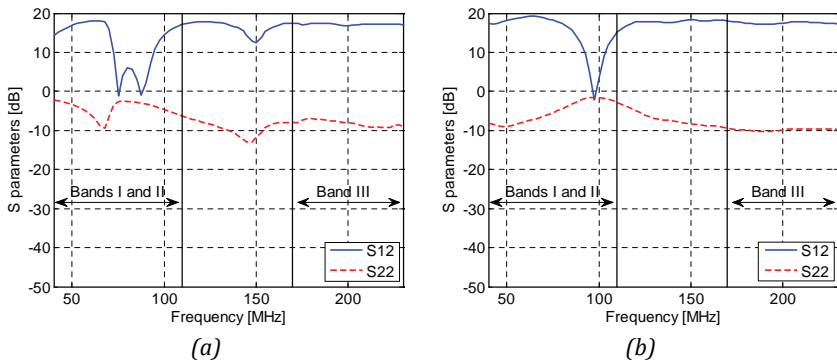


Fig. 23. S-parameters of (a) TV2 amplifier and (b) TV3 amplifier

Fig. 24. shows the comparison of the simulated voltage at the TV2 amplifier output port with measurement results obtained in a Volkswagen car. Two separate frequency ranges are considered: 40 MHz - 110 MHz (Bands I and II) and 170 MHz -230 MHz (Band III).

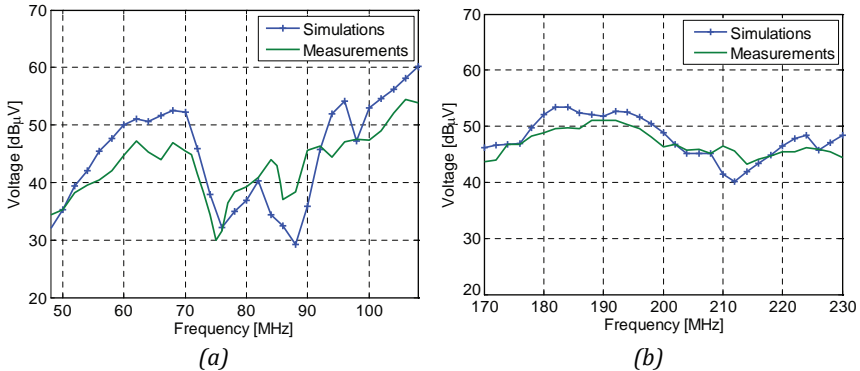


Fig. 24. Voltage received by TV2 antenna in (a) Band I and II, and (b) Band III

Comparison of the simulation results with measured data shows good agreement over the considered frequency ranges. The maximum difference between the simulation and measurement results does not exceed 6 dB.

1.5.4 Multi-partitioned and Multi-excitation MoM Scheme

Problem Formulation

When solving automotive antenna problems, a considerable proportion of the vehicle geometry remains the same in different calculations. For example, this is the case when comparing the characteristics of different antennas mounted in a window-pane of the same car model, or when optimising the shape, dimensions, position and material parameters of a particular antenna to be installed in an automobile. An optimisation of the calculation for different sets of excitations is also required. This section describes a multi-partitioned and multi-excitation MoM scheme that is designed to handle such geometries and excitations effectively.

Let G be a series of geometries G_1, G_2, \dots, G_K with a predominant common (basis) part

$G^b = \bigcap_{k=1}^K G_k$ being an intersection of the geometries G_k . Calculation of the geometries $G_k, k = 1, 2, \dots, K$, using the traditional MoM scheme requires K-times more central processing unit (CPU) time than that needed to handle a single geometry. The purpose here is to enhance the MoM scheme in such a way as to minimise the total CPU time needed to handle a series of geometries under different excitation schemes.

Partitioned MoM Scheme

Let geometry G_K be partitioned on the basis G^b and additional G^a parts, so that $G_K = G^b + G^a$. Reconsidering the boundary-value problem (3) by applying the partitioned sets of expansion and testing functions for the basis G^b and additional G^a geometries, we reduce (3) to the matrix equations with the following block structure:

$$\begin{bmatrix} Z^{bb} & Z^{ba} \\ Z^{ab} & Z^{aa} \end{bmatrix} \begin{bmatrix} I^b \\ I^a \end{bmatrix} = \begin{bmatrix} V^b \\ V^a \end{bmatrix} \quad (20)$$

where the first superscript is associated with the testing procedure, and the second superscript is associated with the expansion procedure, so that the total number of unknowns is $N = N^b + N^a$.

Considering now the lower upper (LU) decomposition of the partitioned impedance matrix:

$$\begin{bmatrix} Z^{bb} & Z^{ba} \\ Z^{ab} & Z^{aa} \end{bmatrix} = \begin{bmatrix} L^{bb} & 0 \\ L^{ab} & L^{aa} \end{bmatrix} \begin{bmatrix} U^{bb} & U^{ba} \\ 0 & U^{aa} \end{bmatrix} \quad (21)$$

one can see that the decomposition of the basis block matrix $Z^{bb} = L^{bb} U^{bb}$ is the same as that obtained for a pure basis geometry G^b . Therefore, considering first the boundary-value problem on the basis geometry G^b and storing the inverted matrices $\tilde{L}^{bb} = (L^{bb})^{-1}$ and $\tilde{U}^{bb} = (U^{bb})^{-1}$ for this geometry, one should then calculate only additional blocks of the partitioned impedance matrix in (20) in order to determine the additional blocks in the LU decomposition (21). Then, the solution of the initial boundary-value problem on the total geometry G_K is found to be:

$$\begin{bmatrix} I^b \\ I^a \end{bmatrix} = \begin{bmatrix} U^{bb} & U^{ba} \\ 0 & U^{aa} \end{bmatrix}^{-1} \begin{bmatrix} L^{bb} & 0 \\ L^{ab} & L^{aa} \end{bmatrix}^{-1} \begin{bmatrix} V^b \\ V^a \end{bmatrix} \quad (22)$$

or, after inversion of the block matrices,

$$\begin{bmatrix} I^b \\ I^a \end{bmatrix} = \begin{bmatrix} \tilde{U}^{bb} & \tilde{U}^{ba} \\ 0 & \tilde{U}^{aa} \end{bmatrix} \begin{bmatrix} \tilde{L}^{bb} & 0 \\ \tilde{L}^{ab} & \tilde{L}^{aa} \end{bmatrix} \begin{bmatrix} V^b \\ V^a \end{bmatrix} \quad (23)$$

where $\tilde{U}^{ba} = -(\tilde{U}^{bb} U^{ba}) \tilde{U}^{aa}$, $\tilde{L}^{ab} = -(\tilde{L}^{aa} L^{ba}) \tilde{L}^{bb}$. In (23), a predominant part of the calculations is associated with determining the inverse block matrices \tilde{L}^{bb} and \tilde{U}^{bb} for

the basis geometry G^b to be stored at the first stage of calculations. If an additional part G^a of the total geometry G_K is much less than the basis part G^b , then calculation of additional blocks needs much fewer operations than that required for the total geometry. This allows performing the additional calculations to obtain the sought solution without considerable spending of CPU time. The structure of multi-partitioned and multi-excitation calculations is illustrated in Fig. 25.

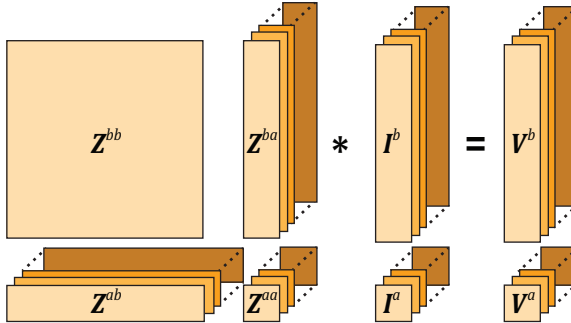


Fig. 25. Structure of multi-partitioned and multi-excitation calculations

A theoretical gain G in solving time is obtained when applying the partitioned MoM scheme (if using the stored LU matrices for the basis geometry), and it can be evaluated as

$$G = \frac{1}{(1 - \beta)/K + \beta} \quad (24)$$

where $K = 1/[1 - (1 - \alpha)^3]$ is the theoretical gain of LU decomposition, $\alpha = N^a/(N^b + N^a)$ is the fraction of the number of additional unknowns (N^a) over the total number of unknowns ($N^b + N^a$), and β is the fraction of the additional time necessary for the calculation processing (it is characterised by the computational system) over the direct-task time. This additional time includes the time necessary for data preparation, loop and thread organisation, memory access, etc. For in-core calculations, this time may be ignored, while for out-of-core calculations this time should include the hard disk drive (HDD) read/write time. For cluster (distributed memory) calculations this time should include the data-exchange time, which may be significant. Table 1. and Table 2. compare the solving times and gains for the sequential/multi-threaded and cluster calculations. These tasks were run on 2-CPU Intel Xeon 3.00 GHz computers (four cores in total) and the cluster consisted of nine computers (36 processors in total).

Table 1. Solving times and gains for sequential calculations for $\beta = 0$

N^b	N^a	α	$G \equiv K$	1 thread used		4 threads used	
				Direct [sec]	Partition [sec]	Direct [sec]	Partition [sec]
28,093	2,935	0.095	3.87	8063	2116	2233	750
28,093	118	0.004	80.03	6052	91	1696	38

Table 2. Solving times and gains for cluster calculations

N^b	N^a	α	K	Direct, [sec]		β	G	3 Partition
				Solve	Exchange			Solve, [sec]
28093	2935	0.095	3.87	474	200	0.42	1.75	332
28093	118	0.004	80.03	383	170	0.44	2.22	211

The presented data shows the significant advantage of using the partitioned MoM scheme when applied to a series of partitioned geometries with a predominant basis part (small values of α). However, this scheme is less effective in the case of distributed memory (parallel) calculations, due to the large amount of data exchange. By optimising the data exchange in the multi-partitioned regime, one can significantly decrease the average β , resulting in an increased gain G in solving time.

1.5.5 Application of Multi-partitioned MoM Scheme to Antenna Design

The derived multi-partitioned MoM scheme has been applied to optimise the glass-antenna structure in a complete car model. Fig. 26. shows a computational model of an Audi A5 with a heating structure and antenna pattern printed on the rear windscreen. A part of the antenna structure used for AM, FM and TV services will be optimised (this part is electrically separated from the heating structure and may be changed relatively easily during the design).

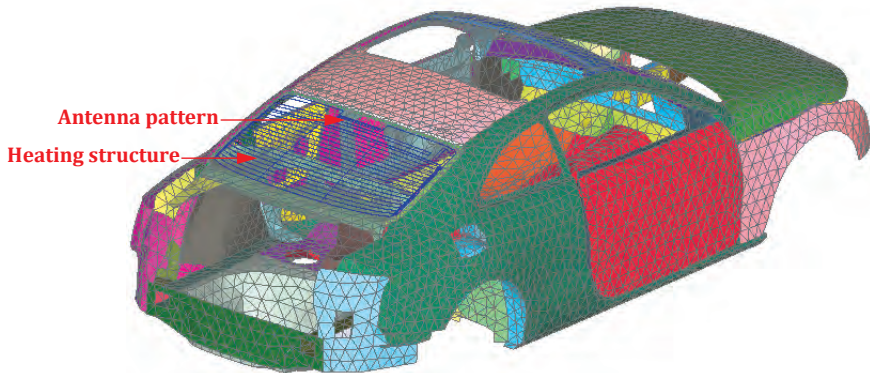


Fig. 26. Audi A5 car body with heating structure printed on the rear windscreen

Using the multi-partitioned scheme, we consider the car bodyshell and heating structure as the basis part of geometry (totally 20,573 metallic elements), and the antenna structure as the additional (partition) part. Fig. 27. (a) to (c) show different variants of the antenna structure with a corresponding pigtail wire, considered as partitions. Fig. 27. (d) compares the reflection coefficients of the antenna variants, calculated in the frequency range 30 MHz to 300 MHz. The obtained results show that modification of the antenna structure does not change the reflection coefficient in the FM frequency range, but it significantly shifts and changes the level of resonances in the TV range (150 - 175 MHz and 210 - 225 MHz, respectively).

Table 3. compares the computational times needed for calculation of three variants of the antenna structure using the direct MoM and multi-partitioned approach. Comparison of CPU times shows a gain G of 1.5 in calculation time for three partitions, demonstrating the advantage of the multi-partitioned scheme when solving optimisation problems on complete car models.

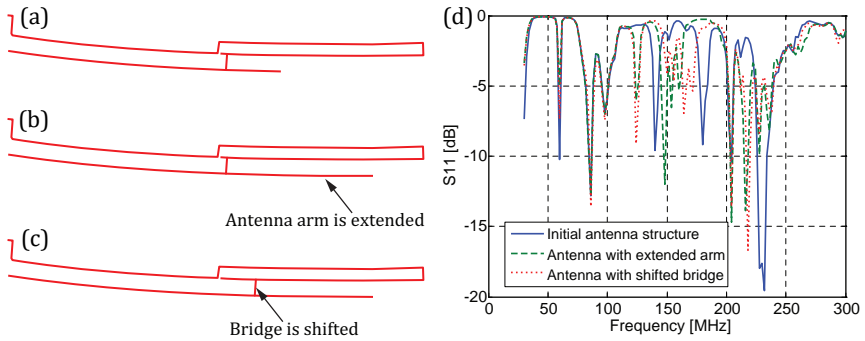


Fig. 27. Different variants of antenna structure: (a) initial structure, 102 metallic elements, (b) structure with extended arm, 117 metallic elements, (c) structure with shifted bridge, 117 metallic elements, and (d) reflection coefficient of the above antennas as a function of frequency

Table 3. Summary of computational times

Solution type	CPU time for one frequency point
Direct solution (three tasks)	3.7 hours (1.23 hours per task)
Matrix-partitioned approach (three partitions)	2.55 hours (1.9 hours for basis + 0.65 hours for three partitions; 13 minutes for each partition)

1.5.6 Testing of Vehicle Antenna Reception in an Open-area Far-field Test Setup

Here, a vehicle antenna reception in an open-area far-field test setup is modelled. Examination of vehicle antenna reception is one of the key stages in system development and certification. A single-axis rotational technique is used to measure the antenna reception pattern. This technique involves the equipment under test (EUT) being placed on a rotational positioner and rotated about the azimuth to measure a two-dimensional polar pattern. It is important to be able to measure two perpendicular (vertical and horizontal) components of the pattern. This measurement is usually accomplished by using a dual-polarised horn, a log-periodic dipole array or a dipole antenna as the transmitting antenna, and it requires either two transmitters or the ability to automatically switch the polarisation of a single transmitter. A typical polar-pattern test setup is shown in Fig. 28.

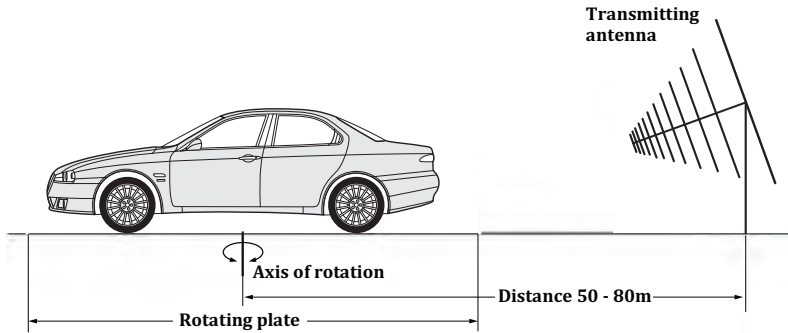


Fig. 28. Test setup for antenna pattern measurements

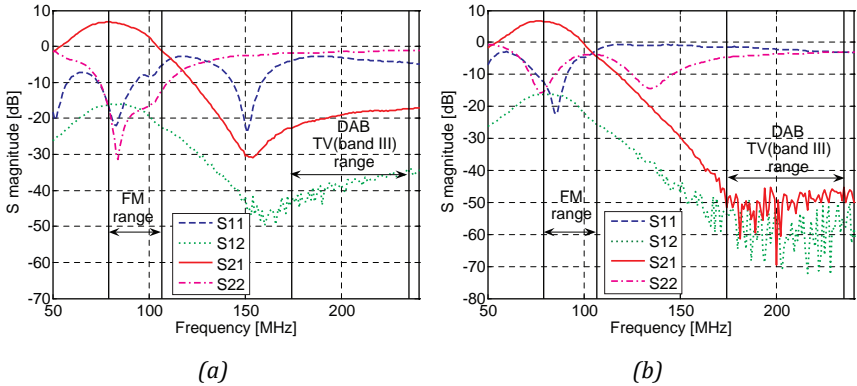
The vehicle with the antenna under test (AUT) is placed on a rotating turntable; the transmitting antenna is placed at a certain level above the ground and at a fixed distance away from the AUT. The turntable is rotated over 360° and the response between the antennas is measured as a function of angle. The distance between the transmitting antenna and AUT is assumed to be large enough to satisfy the far-field condition.



Fig. 29. Car body exposed to plane waves incident from different angles

In the current example, the reception of a glass antenna placed in the rear window of an Audi A5 model is examined. The aim of testing is to analyse the influence of different antenna amplifiers on the level of the received signal. First, a passive antenna is analysed, and then five different amplifiers are connected to the antenna, sequentially, in order to compare the received voltages. The simulations are performed at selected frequencies in the FM and DAB/TV (band III) ranges. In order to obtain vertical and horizontal components of the far-field antenna patterns, the excitation of the transmitting antenna is replaced by vertically and horizontally polarised plane waves of equivalent magnitude. The elevation angle of the incident plane wave corresponds to the location of the transmitting antenna (Fig. 28.) and equals $\theta = 85^\circ$. Instead of rotating the car, in the simulation model it is possible to vary the azimuth angle ϕ from 0° to 360° in order to obtain the received signal as a function of the azimuth angle. In the example given here, the angle ϕ varies from 0° to 350° with a step of 10° (Fig. 29.). The complete number of excitations is 72 incident plane waves. A multi-excitation technique is used to perform these simulations effectively; a multi-partitioned technique is also used. Amplifiers are included in a simulation model as 2-port networks with measured S-parameters, see Fig. 30. (a) to (e), and applied to a pigtail wire connected to antenna structure.

In multi-partitioned calculations, a car body and a complete glass antenna (Fig. 31.), except for a pigtail wire connected to antenna, are defined as a basis part. Six pigtail copies are defined as additional parts (partitions): five for active antenna with different amplifiers (Fig. 32.), one with non-radiating 3 cm TL element with 50Ω resistance for passive antenna.



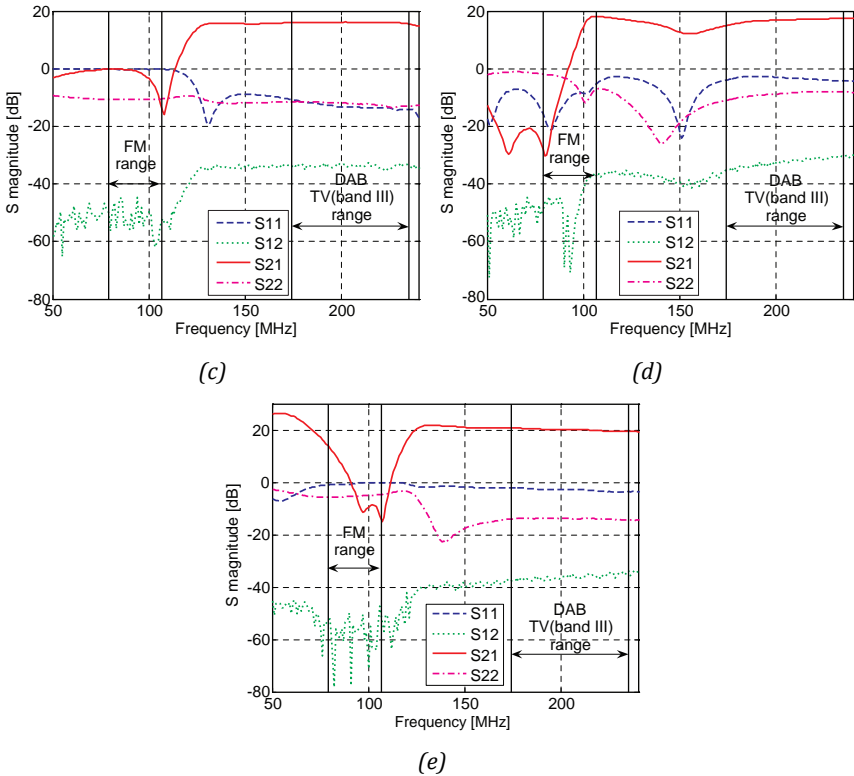


Fig. 30. Measured S-parameters of RF amplifiers as a function of frequency: (a) AM/FM1 amplifier, (b) FM2 amplifier, (c) DAB amplifier, (d) TV1 amplifier, (e) TV3 amplifier

Fig. 33. shows calculated voltages received by antenna with different amplifiers at a certain frequency $f = 174$ MHz as a function of azimuth angle ϕ of incident plane wave for vertical and horizontal polarisations. Received voltage for passive antenna is considered as a reference to see the effect of amplifier. Besides, Fig. 34. and Fig. 35. show the frequency dependence of averaged received voltages (over ϕ angle) for the different frequency ranges and polarisations of incident plane wave.

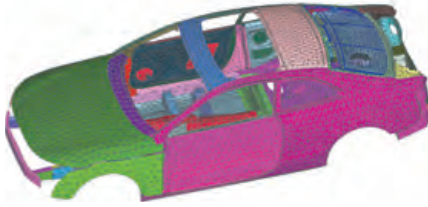
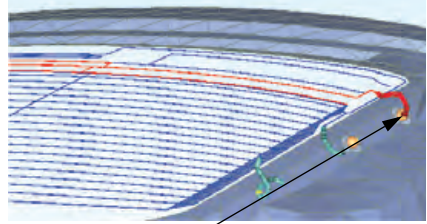
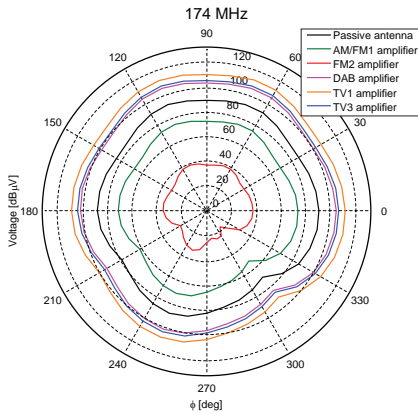


Fig. 31. A car model with a complete antenna pattern considered as a basis part

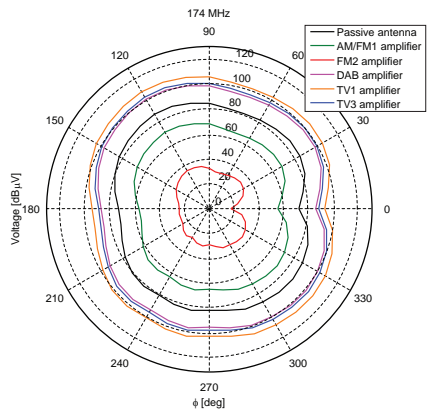


Pigtail wire with amplifier model

Fig. 32. Pigtail wire copies with different amplifiers (partitions)



(a)



(b)

Fig. 33. Voltage received by antenna with different amplifiers as a function of azimuth angle of plane wave at a frequency 174 MHz: (a) vertical polarisation, (b) horizontal polarisation

The presented results clearly show the effect of amplifiers. In FM frequency range AM/FM1 and FM2 amplifiers give the gain of 5-6 dB for both components, except for frequencies 100 MHz and 106.6 MHz, where the amplifier gain goes down. DAB, TV1 and TV3 amplifiers give a quite stable amplification of 15-20 dB in a complete DAB/TV (band III) range.

Comparison of CPU times for the direct and multi-partitioned approach, both using multi-excitation regime (Table 4.), shows the 3.5 gain in calculation time for six partitions, thus demonstrating the efficiency of a multi-partitioned scheme for vehicle antenna problems.

Table 4. Summary of computational times

Solution type	CPU time for a one frequency point
Direct solution with multi-excitation (6 tasks; 72 excitation sources)	9.84 hours (1.64 hours per task)
Matrix-partitioning with multi-excitation (6 partitions; 72 excitation sources)	2.85 hours (2 hours for basis + 0.85 hours for 6 partitions; 8.5 minutes for each partition)

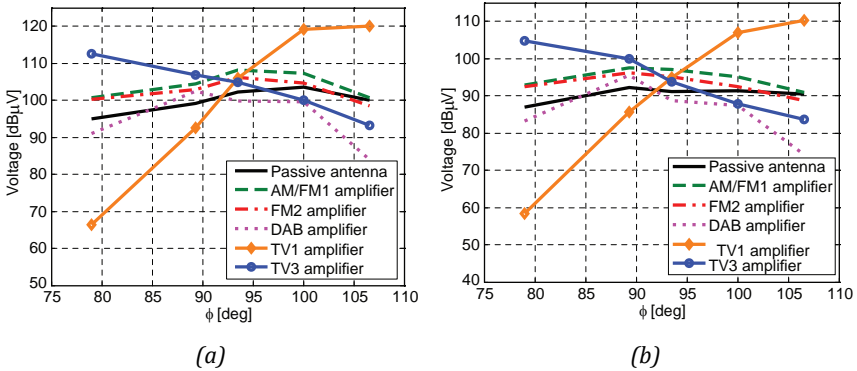


Fig. 34. Averaged received voltage in FM frequency range: (a) vertical component, (b) horizontal component

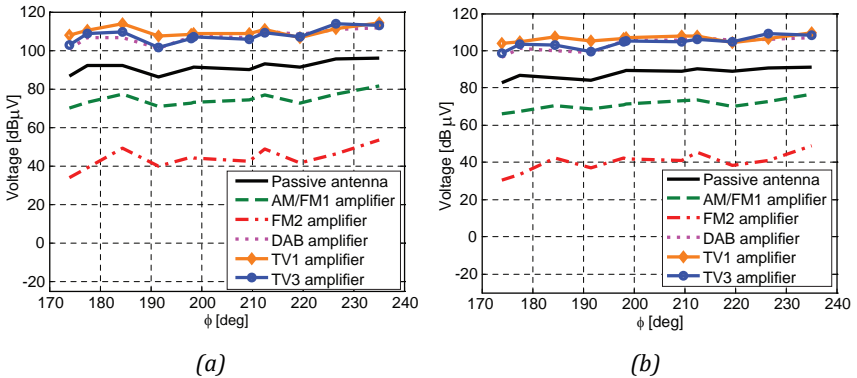


Fig. 35. Averaged received voltage in DAB/TV (band III) frequency range: (a) vertical component, (b) horizontal component

1.5.7 Conclusion

Modern automotive antenna simulations represent a sophisticated and time-consuming process that requires the development of new computational methods and techniques. In this chapter, a number of recent developments in this area have been described, based on the enhancements of the traditional MoM scheme. Special attention has been devoted to adaptive and hybrid methods, special Green's functions for conformal glass antennas and optimisation techniques. Validation and application examples have been considered along with experimental data. The benefits of the described new computational methods and techniques have been illustrated. It is shown that the combined use of traditional and special methods and techniques, as described in this chapter, facilitates obtaining accurate and optimal solutions to complicated automotive antenna problems.

CHAPTER 2

CABLE HARNESS MODELLING

2.1 Cable Harness Description

The design of the cable harnesses that are used to connect electrical modules within an electromechanical device is a complex problem, being also time consuming and costly. The end connectors are dependent on the type of socket provided by the individual modules, which, in turn, determines the types of wires to be used. These individual wires vary in size and, when taken together, they determine the stiffness and mass distribution of the entire cable harness. As a consequence, the stiffness, bend radii and mass of the cable harness collectively dictate the position and number of fasteners required.

A commercial wide-body aeroplane has more than 150 km of wires. Fibre optics will most likely replace many of the wires in aeroplanes in the future. The designers of the Boeing B-52, for example, expected it to have an operational life of 16 to 18 years; however, it is now scheduled to stay in active duty for 50 years. The designers of the Boeing B-52 did not consider the effect of ageing on the copper and insulation materials in the aircraft's cables. In satellites and other space vehicles, the challenges are even more daunting. Radiation can be corrosive and generates electromagnetic interference. Such systems cannot tolerate poor design specifications because every kilogram of extra weight adds around US \$32,000 to the cost of an aircraft launch.



Fig. 36. Part of the cable harness of an automobile

A typical vehicle today has more than twenty on-board microcomputers, all of which need to communicate with each other and with sensors and actuators in all types of weather conditions and, in certain cases, at extreme temperatures. In a commercial vehicle, the weight and cost of a cable harness is second only to the weight and cost of the engine. Since ten years ago vehicle development time has reduced from 36 months to 18 months today. Indeed, Formula 1 racing cars go from design start to first competitive start in about six months.

Because cables are electromechanical devices, the software that is used to support their development must address both the electronic and the mechanical aspects of the design process. System architects seek a tool that allows them to design an entire system and evaluate choices. Electronic and mechanical engineers use somewhat different terminology (jargon) and they have different physical principles to consider. Thus, automotive engineers need tools in their respective disciplines that can communicate relevant data and information to the tools in the other disciplines involved in the vehicle design, while at the same time keeping track of the progress and status of the entire design as a complete unit. Even more importantly, the development flow is separated from the manufacturing and procurement flow; a situation that often leads to errors and delays. The challenges are many: designers select wire gauges and create wire interconnects by hand, and the process is difficult to replicate. Many departments within a company share design data. Without an integrated computerised design flow, designers must enter the same data many times and store them in different databases. Modifying the design data is, therefore, an error-prone and a time-consuming task.

The 10303-series of ISO standards, known under the acronym STEP (Standard for the Exchange of Product Model Data), defines data schemas and file formats that help to facilitate the exchange of product data between various types of data management systems. Unlike earlier ISO standards such as GES, SET and VDAFS not only is STEP focussed on geometric aspects but also it covers product identification, product structure, change management, external (black-box) documents and so on. The data schemas that are relevant for actual data exchange processes are defined in the so-called application protocols. An application protocol (AP) is designed to suit the requirements of a certain application domain and it is an individual part of the 10303-series, e.g. ISO 10303-212: Electrotechnical Design and Installation (AP212). A file that contains data according to AP212 and is structured according to ISO-10303-21 is known as an 'AP212 physical file'. One of the forms of the AP212 format, used widely in the German automotive industry, is the KBL format, which describes information related to cable harness.

The following paragraphs describe methods of EM simulation of cable harnesses.

2.2 Simulation of Non-uniform Transmission Lines

2.2.1 Introduction

Problems of proper cable harness design are increasingly significant in the context of modern technological progress. In sensitive electronic systems such as radio communication, GPS, TPMS etc., noise from cable harnesses or interactions between cables may influence overall system performance. Laboratory EMC tests are difficult and time consuming in some cases. Use of simulation as a supplementary tool to physical measurements for the investigation of complex EMC problems promises to increase the overall speed of system design. Such simulations are based on different numerical methods. Generally, cables are represented by multi-conductor transmission-line models and can be simulated by means of lumped (LCTL) circuits [73]. Such an approach based on LCTL belongs to approaches using approximate methodologies. Full-wave 3D solutions (MoM, FEM, FDTD) are more accurate than methods that use approximate methodologies but, at the same time, more demanding in terms of computational resources and time. It has been demonstrated that for cable harness simulations, multi-conductor line representation gives reasonable results in most practical cases. Simulations based on multi-transmission line (MTL) account for non-uniform charge distribution in cross sections of cables. In full-wave solutions, consideration of cable proximity drastically increases the demand for computational resources. It can, therefore, be concluded that the approximate LCTL method gives both rapid and acceptably accurate solutions for industrial cable harness EMC problems.

The following sub-sections will focus on cable-to-cable and on antenna-bundle interactions [74]. Three kinds of problems will be considered: crosstalk (xtalk) – interaction between cables; susceptibility – when a passive cable harness is irradiated by an antenna; and radiation – when a cable radiates into a passive antenna. Corresponding hybrid approaches are called susceptibility and radiation hybrids. Both approaches are based on a combination of basic methods (MoM, LCTL).

2.2.2 Multi-transmission Line (MTL) Approach for the Investigation of Crosstalk in Cables

General Theory

An MTL model of a system of cables, under the assumption of the transverse electromagnetic (TEM) mode of propagation, can be represented by the distributed parameter transmission-line equations [73]:

$$\frac{\partial V(z,t)}{\partial z} = -rI(z,t) - l \frac{\partial}{\partial t} I(z,t) \quad (25)$$

$$\frac{\partial I(z, t)}{\partial z} = -gV(z, t) - c \frac{\partial}{\partial t} V(z, t) \tag{26}$$

where $I(z, t)$ and $V(z, t)$ are the currents in the conductors and the voltages between two conductors, respectively. The coefficients r , c and l are the per-unit-length resistance, capacitance and inductance of the two conductors, respectively. If the surrounding dielectric has non-zero conductivity, there is an additional per-unit-length conductance parameter, g .

In the general case, a non-uniform multi-conductor line can be modelled as an assembly of segments, see Fig. 37. Each segment is approximated by a uniform transmission line with some pre-defined parameters. The per-unit-length parameter matrices (inductance L , capacitance C , resistance R and medium conductance G) are calculated using a combination of the method of auxiliary sources and MoM [75].

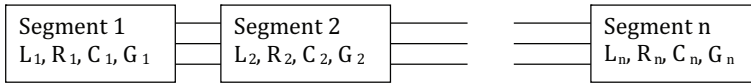


Fig. 37. Segmentation of MTL

The segmentation is performed according to selected physical properties such as wavelength, non-uniformity of both the line and the surrounding 3D environment, termination impedances, and, if necessary, branches. After segmentation, the circuit model is prepared and a SPICE-like circuit simulator is used to perform calculations.

Each line segment has its own characteristic impedance matrix. Fig. 38. shows an example of a short two-wire segment of length Δl modelled as a T-circuit [73] - [74].

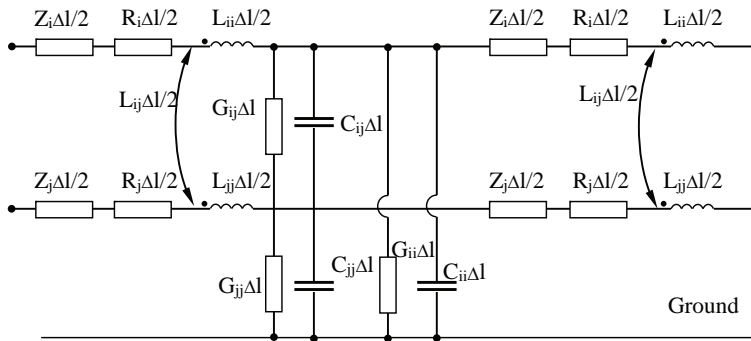


Fig. 38. Equivalent lumped-circuit model for two wires

For conductors with finite conductivity, the DC resistance is given by:

$$R_i = \frac{1}{\sigma_i \cdot S}; S = \pi \cdot r_w^2 \quad (27)$$

If the surrounding medium of conductors is lossy, then the conductance is obtained by [73]:

$$G_{ij} = \omega \cdot C_{ij} \cdot \tan \delta_{ij} \quad (28)$$

where $\tan \delta_{ij}$ are the tangential losses between two conductors (or between a conductor and the ground) due to the realistic surrounding medium and $\omega = 2\pi f$, where f is frequency of interest. A special technique is developed to calculate approximate tangential losses, based on finding an effective area between conductors and averaging out losses of all dielectric regions within this area.

The skin effect should be taken into account at high frequencies, and it can be modelled as an impedance that is calculated by the following formulas [76]:

$$\begin{cases} Z_i = (1 + j) \frac{1}{2\pi r_w \sigma \delta}, & r_w \gg \delta \\ Z_i = \frac{j \cdot R_s}{\sqrt{2} \cdot \pi \cdot r_w} \cdot \frac{J_0(\sqrt{-j} \cdot q)}{-\sqrt{-j} \cdot J_1(\sqrt{-j} \cdot q)}, & \text{otherwise} \end{cases} \quad (29)$$

$$\delta = \frac{1}{\sqrt{\pi \cdot f \cdot \mu_0 \cdot \mu_r \cdot \sigma}}, R_s = \frac{1}{\sigma \cdot \delta}, q = \frac{\sqrt{2} \cdot r_w}{\delta} \quad (30)$$

The model considered above allows simulation of shielded cables and successfully represents inductive and capacitive interactions between the shield and core. However, the external electric and magnetic fields can penetrate through imperfections in the cable shield and give rise to spurious currents and voltages on the internal conductors. The coupling between the external EM field and the inner conductors occurs due to three physical phenomena: (i) diffusion of the E and H fields through the sheath material, (ii) penetration of the E and H fields through the small apertures of the braided shields and (iii) more complicated induction phenomena due to the overlap of the individual strands (or carriers) of the shield. The last two phenomena occur only for braided shields. The behaviour of the induced response in the inner conductors of a shielded cable can be described in terms of the transfer impedance Z_t and the transfer admittance Y_t of the shield.

A scheme for a shielded cable segment is represented in Fig. 39. below.

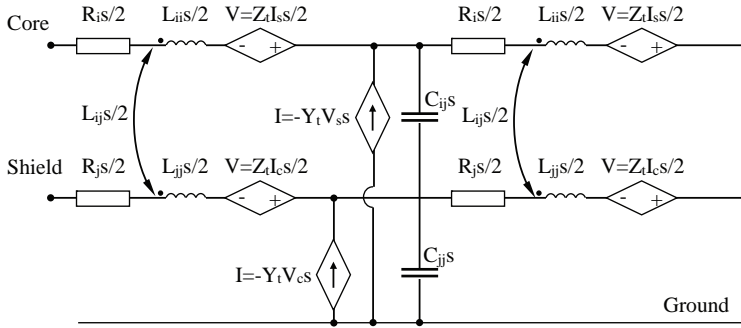


Fig. 39. Equivalent circuit for coaxial cable

In Fig. 39., I_s is the current on the shield, I_c is the current on the inner conductor, Z_t is the transfer impedance, and Y_t is the transfer admittance.

In the case of a braided shield, the transfer impedance and admittance are calculated according to the well-known formulas [77] - [78]:

$$Z_t = Z_d + j \cdot \omega \cdot L_a \pm j \omega L_p \quad (31)$$

$$Y_t = j \cdot \omega \cdot \frac{\pi \cdot \epsilon_{eq} \cdot C \cdot C_s}{6 \cdot \ell \cdot \epsilon_{int} \cdot \epsilon_{ext}} \cdot (1 - K)^{3/2} \cdot \frac{1}{E(e)}, \quad \psi < 45 \quad (32)$$

$$Y_t = j \cdot \omega \cdot \frac{\pi \cdot \epsilon_{eq} \cdot C \cdot C_s}{6 \cdot \ell \cdot \epsilon_{int} \cdot \epsilon_{ext}} \cdot (1 - K)^{3/2} \cdot \frac{1}{(1 - e^2) \cdot E(e)}, \quad \psi > 45^\circ$$

$$\epsilon_{eq} = \frac{2 \cdot \epsilon_{int} \cdot \epsilon_{ext}}{\epsilon_{int} + \epsilon_{ext}} \quad (33)$$

where Z_d represents the field penetration through the shield material and is calculated by Schelkunoff's formula [77] - [78], L_a corresponds to the penetration through the holes in the shield, and L_p is caused by the magnetic flux linkage between the inner and outer braid layers. In these formulas, $\epsilon_{int} = \epsilon_{r_{int}} \epsilon_0$, $\epsilon_{ext} = \epsilon_{r_{ext}} \epsilon_0$ are the dielectric constants of the regions inside and outside the cable, respectively, C_s is the capacitance of the coaxial region, C is the external capacitance of the line to the ground, K is the optical coverage of the shield, e is the eccentricity of the elliptical aperture equivalent to the rectangular shield holes, and ℓ is the major axis length of the equivalent elliptical aperture. In the case of a solid shield, only penetration through the shield material occurs, and L_a and L_p vanish. The transfer admittance Y_t is sufficiently small that it does not affect the calculation and, thus, it can be considered equal to zero.

2.3 Crosstalk Application Examples

Crosstalk between Cables

Here the crosstalk between two cables is investigated and simulation results are compared with measurements. A twisted-pair cable N.901.916 (Fig. 40.) and a single wire without insulation are located above a 2 m x 1 m metallic plate (Fig. 41.). A scheme for the solution of the problem is described below. First, the total electric field radiated by a single wire is calculated by using a full-wave MoM solver [1]. Next, the obtained fields are converted into coupled voltage sources, which are used in the transmission-line model of the victim cable (TWP N.901.916). Finally, the voltages and currents at cable terminations are calculated by using the SPICE circuit solver. The simulation model is shown in Fig. 42.

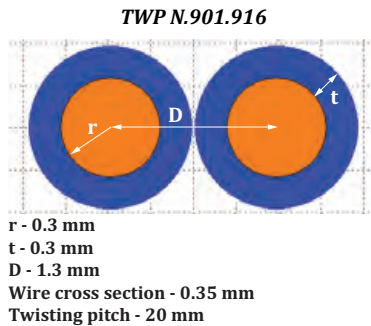


Fig. 40. Twisted-pair cable

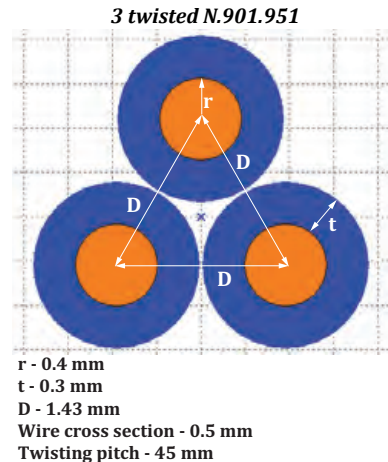


Fig. 41. 3-twisted wire cable

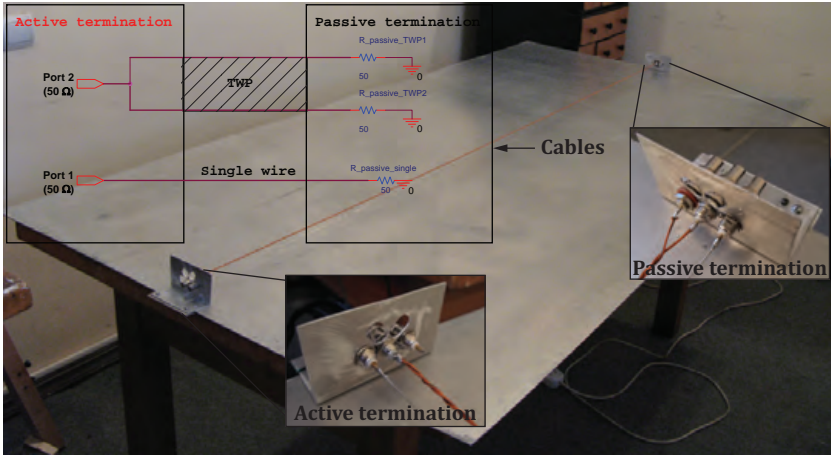


Fig. 42. Single wire and TWP cable. Measurement setup

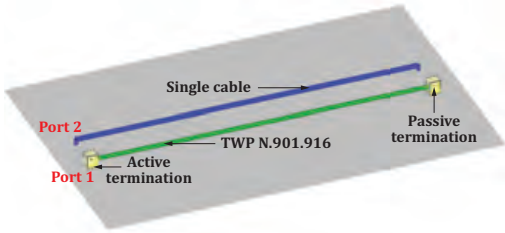


Fig. 43. Simulation model of a single wire and a TWP cable

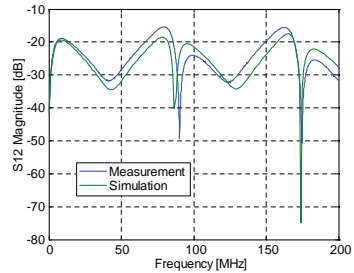


Fig. 44. Magnitude of the transmission coefficient vs. frequency

Measurement and calculations are performed for the transmission coefficient of a two-port system; Port 1 is a single-wire port, while Port 2 is a TWP cable port. A comparison of measured and simulated transmission coefficients is presented in Fig. 44.

This hybrid approach was applied successfully for the inverse problem (where the cable harness radiates into the wire or antenna) and for more complex combinations of TWP and 3-twisted cables with different rod and glass antennas, including a rear-window car antenna [74].

2.4 Radiation and Susceptibility Hybrid Approaches

2.4.1 Introduction

Radiation and susceptibility hybrid approaches will now be considered. A radiation hybrid approach is realised as follows. A cable harness is analysed as MTL by means of the LCTL approach. This results in the calculation of currents along each cable. These currents are then converted into external sources for MoM calculations. In susceptibility problems, fields in the absence of cables are calculated using the MoM approach. Then, field values at cable positions are transformed to external sources for MTL equations, and the LCTL approach is used to solve these equations. Such hybridisation of methods exploits the advantages of each separate method: MoM is strong for modelling 3D structures and weak for modelling tightly placed cables. LCTL is a convenient tool for cable modelling but it is unable to estimate fields in a 3D environment. However, such hybridisation accounts only for primary field coupling and is unable to consider multiple interactions between cables and the 3D surroundings.

2.4.2 Experimental Validation

Combinations of twisted cables with rod and different glass antennas, including an automotive rear-window antenna, are now considered. The measurement setup is shown in Fig. 45. A two-port system is considered in all measurements. Port 1 is the antenna port, while Port 2 is the cable port. The cables shown in Fig. 40. and Fig. 41. are used for measurements and simulations.

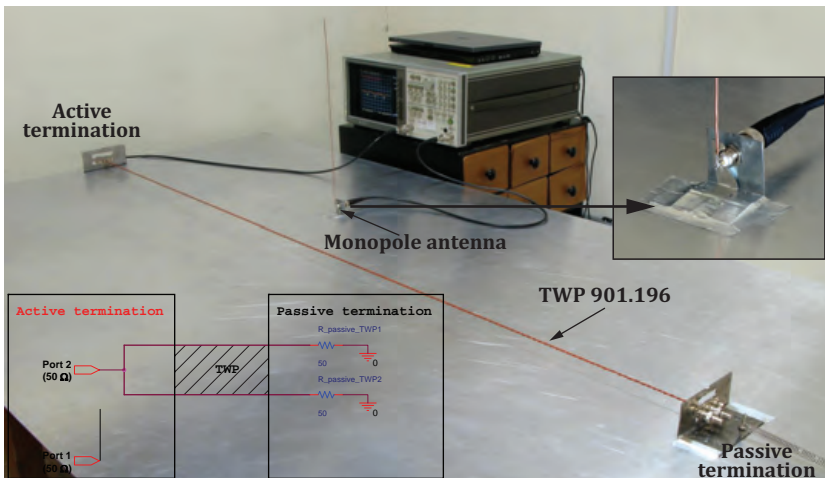


Fig. 45. Monopole and TWP cable. Measurement setup

Consider the problem of the interaction between a TWP N.901.916 cable and a monopole antenna located above a metallic plate, as shown in Fig. 45., where the monopole antenna is an uncoated metallic rod with diameter 1 mm. The corresponding simulation model is shown in Fig. 46.

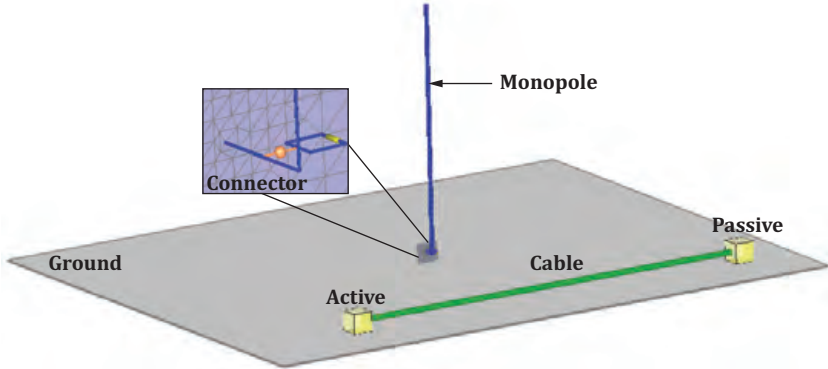


Fig. 46. Monopole and TWP cable. Simulation model

Numerical results for the transmission coefficient are presented in Fig. 47. and Fig. 48.

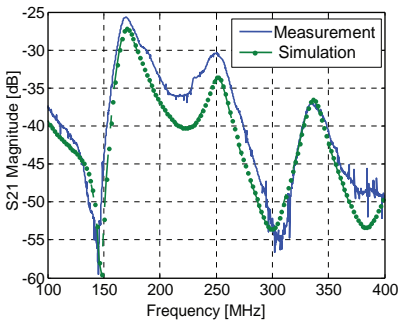


Fig. 47. Active monopole

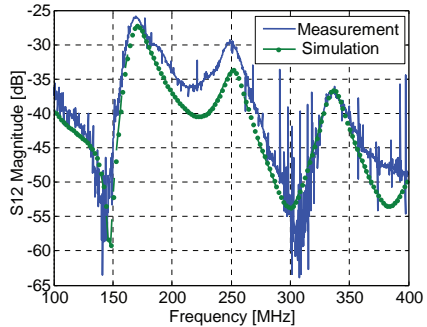


Fig. 48. Active TWP cable

From Fig. 47. and Fig. 48., it can be seen that the simulation results are in very good agreement with the measurements. Furthermore, the transmission coefficient is the same in both cases, in agreement with theory. Additional noise is present on the measurement curve when the antenna works in receive mode (Fig. 48.); this is because the measurements were performed in an unshielded room and an antenna is more sensitive to surrounding noise sources than is a cable.

Measurements and simulations were also performed for a planar glass antenna in combination with TWP N.901.916 and 3-twisted N.901.951 cables. A general view of the measurement setup is shown in Fig. 49. and a schematic representation of the cable terminations is shown in Fig. 50.

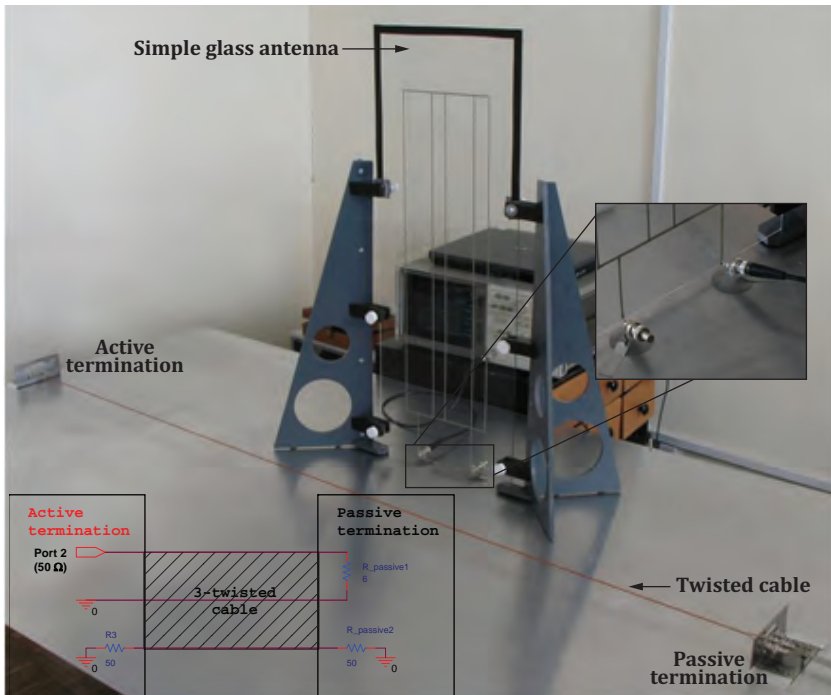


Fig. 49. Glass antenna and TWP cable. Measurement setup

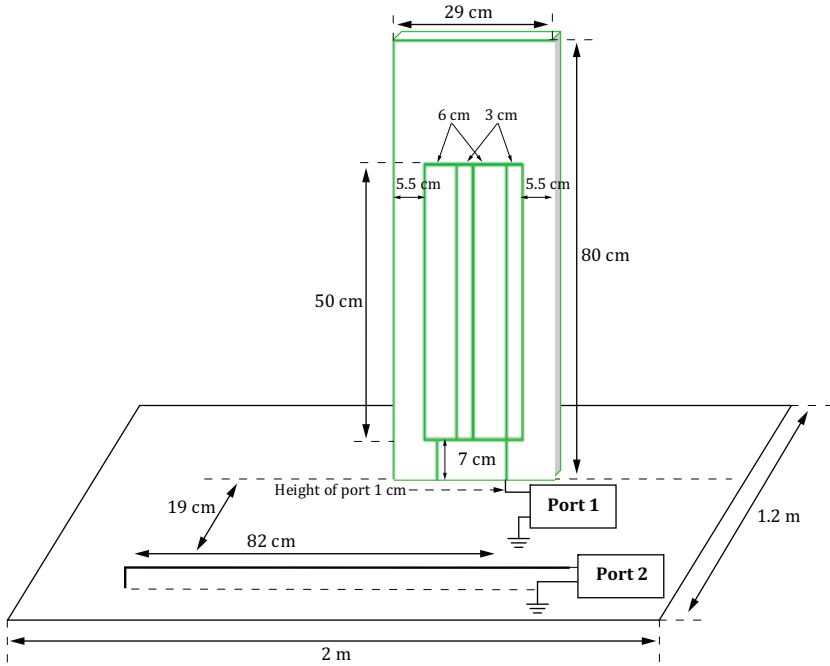


Fig. 50. Glass antenna and TWP cable. Setup schematic

The transmission coefficients are presented in Fig. 51. and Fig. 52.

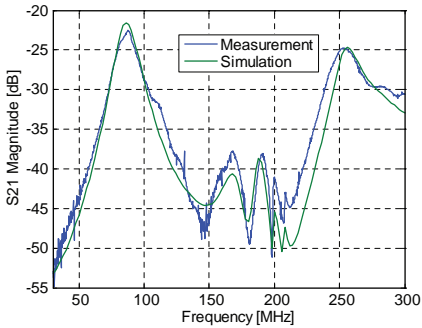


Fig. 51. Transmission (TWP 901.916)

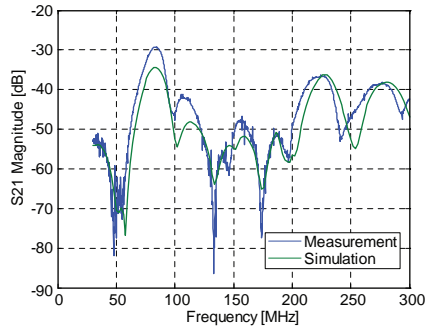


Fig. 52. Transmission (3-twisted 901.951)

Once again, it can be seen that the simulations give results that are in good agreement with the measured data.

Consider now the more complex structure of Fig. 53., which shows the setup for a vehicle rear-window antenna located above a metallic plate; the antenna interacts with a 3-twisted cable. Two models of signal propagation through an active cable are considered: common and differential modes. The window is placed at some angle (about 60°) above the metallic plate. In addition to the general measurement setup, Fig. 53. gives a schematic representation of the cable terminations.

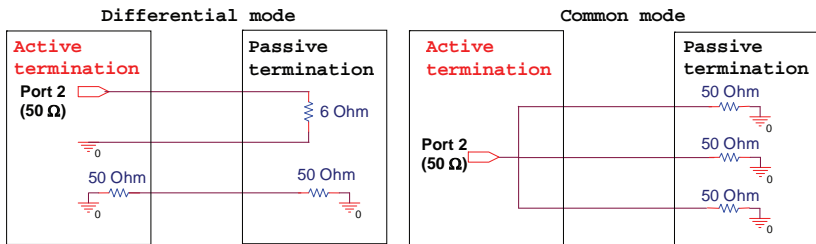
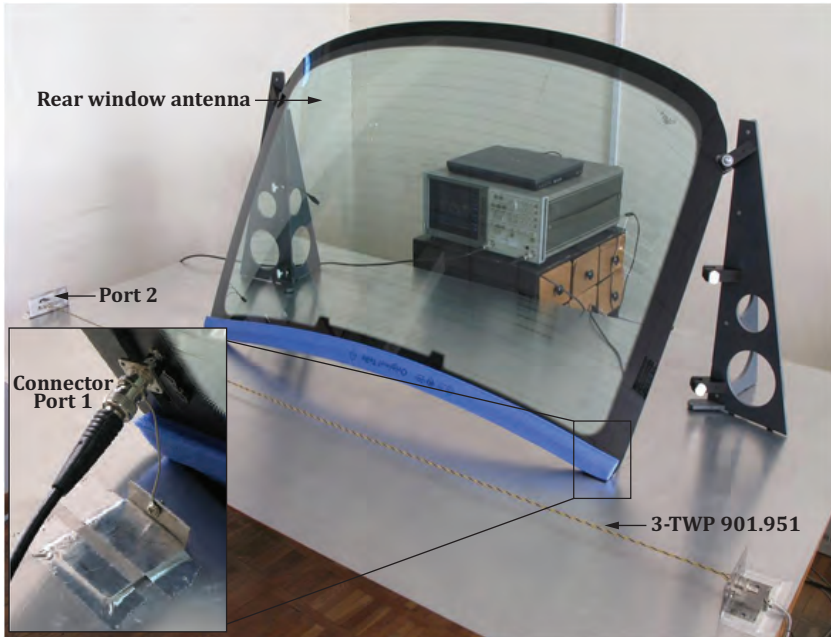


Fig. 53. Cable and car rear-window antenna. Measurement setup and schematic of cable terminations

Numerical results for the transmission coefficients are shown in Fig. 54. and Fig. 55.

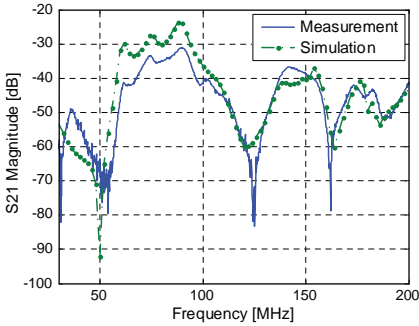


Fig. 54. Transmission coefficient (common mode)

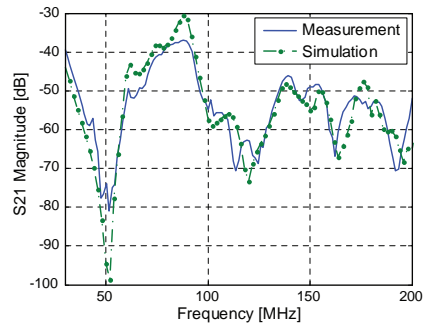


Fig. 55. Transmission coefficient (differential mode)

From Fig. 54. and Fig 55. it can be seen that the hybrid approaches described above can be applied not only to simple antenna-harness configurations but also to complex problems that often occur in real car systems.

2.4.3 Discussion

An LCTL approach and LCTL variations for cable harness-related EMC problems are developed and realised in software. It is demonstrated that the simulations performed using this approach give acceptable results. Using skin-effect impedances and tangential loss coefficients in the circuit analysis gives the possibility for the consideration of realistic cables with dielectric losses, which makes the simulation results more accurate and brings them into better agreement with physical measurements. Implementation of the transfer impedance and admittance in the shielded-cable scheme allows simulation of shield imperfections. A special model is implemented for rapid calculation of lossless and quasi-uniform transmission lines. A fast Branin's method [74] has improved calculation times in comparison to the basic LCTL approach.

Radiation and susceptibility methods are very useful for simulation of the problems highlighted in this section, because a multi-transmission line model successfully describes interactions inside cable bundles, and for antenna (especially glass antenna) structures, it is convenient to use MoM hybridised with a special Green's function. It is demonstrated that simulations performed by hybridising transmission-line theory with MoM can give reasonably accurate results in cable-antenna interaction problems.

2.5 Modelling of Power Cables

2.5.1 Introduction

The utility industry in Germany and elsewhere is under increasing pressure to use new underground transmission facilities in urban areas. Although undergrounding is acceptable for many reasons, faults and failures of undergrounding can be extremely severe in financial terms, due to both revenue loss and repair costs. Consequently, there is an increasing need for more reliable tests during installation, commissioning and operation. Such tests are required to ensure the reliability of the entire cable system, especially that of joints and terminations.

Traditionally, cable users prefer high-voltage (HV) endurance tests, such as DC or AC hipot tests, or other dielectric tests, such as dissipation factor (power factor) and insulation resistance measurement. Such testing methods are efficient for oil-insulated cables, but they have limited effectiveness for polymer-insulated cables, where the tests may be destructive or, under certain conditions, will pre-damage the cable.

One common non-destructive method providing information on the presence of latent defects, known to cause premature in-service failure of HV cables, is the measurement of partial discharges. Low-energy sparks in HV cables are usually an early indicator of a forthcoming serious failure. The most critical locations are at cable accessories, e.g., cable joints. In order to fully realise the benefits of partial discharge (PD) testing, the measurement system must be sufficiently sensitive. Traditionally, this measurement has been done at one cable end, but only very limited sensitivities can be achieved due to the strong attenuation of PD pulses along the polymer cables. Noise voltage sources and pulses that couple into the measurement setup will further reduce the achievable sensitivity for the traditional method. Alternative methods detect the transient fields close to the PD location using field sensors that are usually placed directly on the cable close to, or in, cable accessories.

In order to design and improve the needed field sensors, it is necessary to understand the pulse properties, the propagation characteristics within the cable and its joints, and the coupling mechanisms of PD fields into sensors.

Cross-linked polyethylene (XLPE) is used widely as an insulation material in HV cables. HV cables are inhomogeneous, lossy for higher frequencies and dispersive. High-frequency characteristics such as permittivity and conductivity are not well known for this material. It is also difficult to predict the sensitivity of the PD sensor as a function of longitudinal and radial PD locations for different sensor types.

Most recent studies have been limited by their experimental approach due to the fact that in order to measure PD on HV cable joints, long and expensive cables with joints must be destructed. Furthermore, only a few of the possible PD locations are accessible without destroying the joint. These practical barriers to physical measurement make simulation the method of choice for analysis.

Application of advanced numerical approaches and the development of new computational algorithms will provide an in-depth understanding of the electrodynamical processes in XLPE cables and joints, and will support the design of optimal PD sensors.

One common method to detect PD is the measurement of the radiated fields of the PD with sensitive field sensors [79] - [83]. External noise coupled with the cable may, however, be stronger than the fields generated by PD; this limits measurement sensitivity, often to an unsatisfactory level.

In order to design and improve the field sensors, which are usually placed directly on the outer semi-conducting (semicon) layer of the cable or accessory, knowledge of the pulse properties, the propagation characteristics of the cable and the external noise interference is necessary. XLPE cables and accessories are, for higher frequencies, inhomogeneous, lossy and dispersive. The behaviour of the PD itself is difficult to predict. It is also difficult to predict the sensitivity of the PD sensor as a function of longitudinal and radial PD locations for different sensor types. Taken together, these problems account for the dominance of experimental rather than simulation studies in this field, to date. It is, therefore, desirable to develop additional numerical tools in order to improve the measurement methods and the sensitivity of PD sensors.

This section presents a simple and efficient finite-difference time-domain (FDTD) model for the simulation of a radially symmetric PD sensor [83] - [85]. The dependence of the sensor sensitivity on the length of the sensor and on the thickness of the substrate is investigated experimentally and theoretically.

2.5.2 Numerical Model of the Sensor and Cable

An HV cable consists of an inner conductor, insulation, inner and outer semicon layers and an outer shield. The sensor is placed on the outer semicon layer and consists of an insulation layer, an electrode and a dielectric substrate above the electrode. The sensor is completely covered by the outer shield of the HV cable. The shield normally consists of copper wires and a water-impermeable aluminium or copper foil, or of a completely closed outer metallic aluminium sheath, both of which shield against external noise very well.

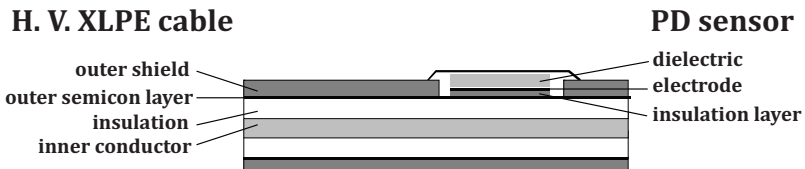


Fig. 56. Schematic representation of an HV cable and PD sensor

Considering the problems of constructing a 3D full-wave time-domain model of the HV cable and PD sensor, a radially symmetric model was developed initially. Using this symmetry, the analysis can be reduced to a 2D model.

According to the measurement data, semicon materials (carbon black-filled polymers) have large frequency-dependent dielectric constants (ϵ_r , from several 1000 s down to several 10 s in the frequency range up to 1 GHz) and conductivity in the range 0.1 - 10 S/m. This data shows good agreement with literature data [86] - [88]. However, consideration of frequency-dependent data and high dielectric constants and conductivity require considerable computational efforts. Therefore, it was decided that effective values for the conductivity and the dielectric constant of the semicon layers for simulation should be derived.

The effective data are derived from a comparison between measurements of pulse propagation on HV cables and simulations. The effective permittivity was chosen to be $\epsilon_r = 2.3$ in the simulations in order to obtain similar propagation characteristics of the insulation and semicon layers. A good agreement with experimental data for 1 ns and 3 ns pulse widths, which simulate internal PD pulses, was found for a constant effective permittivity of $\epsilon_r = 2.3$ and a constant effective conductivity of $\sigma = 0.1$ S/m. Any dispersive characteristics of the semicon layers were neglected.

Furthermore, only the TEM mode of PD is taken into account; this is valid if the PD source is located at a sufficiently large distance from the sensor, so that higher modes are attenuated.

Computer simulation is performed using the FDTD method. The FDTD grid that was used to model the cable and the sensor is shown in Fig. 57. This grid uses a 2D cylindrical coordinate system, exploiting the rotational symmetry of the coaxial cable and the sensor about the z-axis. In this coordinate system, the TE mode is composed of E_ϕ , H_r and H_z components, while the TM mode has E_r , E_z and H_ϕ components. Since the coaxial line is excited with a TEM mode consisting of only E_r and H_ϕ , only the TM cylindrical mode is modelled.

The discrete analogue of the Maxwell equations used for this calculation are functions of space points and time [89]. We denote a point in space in a cylindrical coordinate system in a uniform, rectangular lattice as:

$$(i, j) = (i\Delta r, j\Delta z) \quad (34)$$

Since we consider just rotationally symmetric fields, all physical quantities are related to the plane $\phi = 0$. Δr and Δz are the lattice space increments in the r and z coordinate directions, respectively, and i and j are integers. Furthermore, we denote any function F of space and time as:

$$F(i\Delta r, j\Delta z, n\Delta t) = F^n(i, j) \quad (35)$$

where Δt is the time increment and n is integer. Using standard centred finite-difference (central-difference) expressions for the space and time derivatives, and solving for the field components that represent later time quantities, we obtain the following formulas.

E_r (represented by rhombuses in Fig. 57.):

$$E_r^{n+1}(i, j - 0.5) = \frac{1 - \frac{\sigma(i, j - 0.5)\Delta t}{2\varepsilon(i, j - 0.5)}}{1 + \frac{\sigma(i, j - 0.5)\Delta t}{2\varepsilon(i, j - 0.5)}} E_r^n(i, j - 0.5) - \frac{\Delta t}{\varepsilon(i, j - 0.5)\Delta z} \cdot \frac{1}{1 + \frac{\sigma(i, j - 0.5)\Delta t}{2\varepsilon(i, j - 0.5)}} \cdot [H_\phi^{n+0.5}(i, j) - H_\phi^{n+0.5}(i, j - 1)] \quad (36)$$

E_z (represented by asterisks in Fig. 57.):

$$E_z^{n+1}(i + 0.5, j) = \frac{1 - \frac{\sigma(i + 0.5, j)\Delta t}{2\varepsilon(i + 0.5, j)}}{1 + \frac{\sigma(i + 0.5, j)\Delta t}{2\varepsilon(i + 0.5, j)}} E_z^n(i + 0.5, j) - \frac{\Delta t}{\varepsilon(i + 0.5, j)\Delta r} \cdot \frac{1}{1 + \frac{\sigma(i + 0.5, j)\Delta t}{2\varepsilon(i + 0.5, j)}} \cdot \frac{1}{r_{i+0.5}} [r_{i+1}H_\phi^{n+0.5}(i + 1, j) - r_iH_\phi^{n+0.5}(i, j)] \quad (37)$$

H_ϕ (represented by crosses in Fig. 57.):

$$H_\phi^{n+0.5}(i, j) = H_\phi^{n-0.5}(i, j) + \frac{\Delta t}{\mu\Delta r} [E_z^n(i + 0.5, j) - E_z^n(i - 0.5, j)] - \frac{\Delta t}{\mu\Delta z} [E_r^n(i, j + 0.5) - E_r^n(i, j - 0.5)] \quad (38)$$

In these equations, σ is the conductivity of the material [S/m], $\varepsilon = \varepsilon_r \varepsilon_0$ is the permittivity [F/m], where ε_r is the relative permittivity and $\varepsilon_0 = 8,85 \cdot 10^{-12}$ is the dielectric constant [F/m], and $\mu = \mu_0$ is the permeability of the material [H/m], where $\mu_0 = 4\pi \cdot 10^{-7}$ is the magnetic constant [H/m].

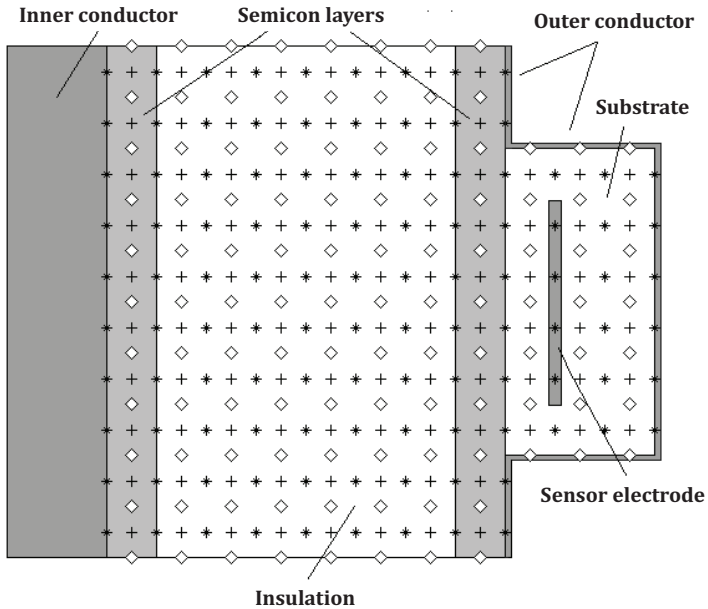


Fig. 57. FDTD grid for HD cable and PD sensor

An impulsive voltage excitation within the coaxial line $U(t) = U_0 \exp(-\alpha^2 t^2)$ is used at the beginning of the coaxial line in combination with an exact absorbing boundary condition (ABC) in order to emulate a matched source at that location. The parameter α is selected so as to change the width of the pulse. The exact ABC is also employed at the end of the coaxial cable.

Such a model can reflect some basic characteristics of the PD pulse, propagating in the cable and on the sensor, such as the dependence of sensitivity on the length of the sensor and on the substrate thickness and permittivity.

Fig. 58. shows the setup that was used to verify the simulation experimentally. Measurements were made in order to investigate the influence of different parameters, e.g. length of the sensor and thickness and material characteristics of the sensor dielectric (substrate).

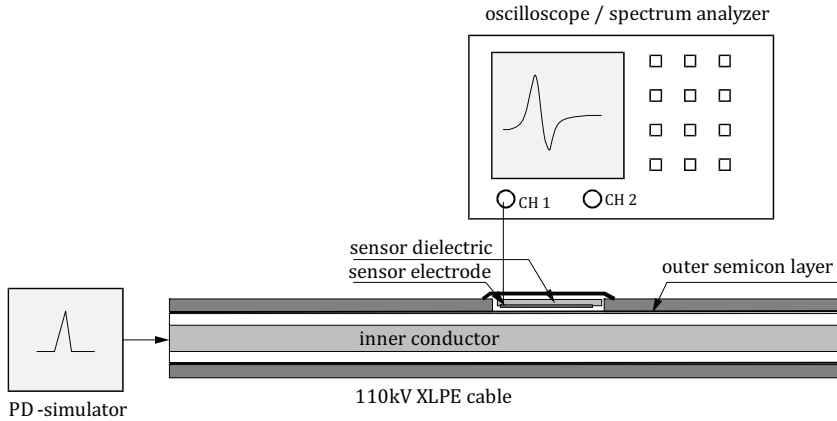


Fig. 58. Measurement setup for experimental optimisation of the sensor

The PD event is simulated by a short Gaussian pulse injected directly into the HV cable. The pulse width is adjustable in the range of a few nanoseconds. The signals are detected using an oscilloscope or spectrum analyzer.

Based on the discrete analogue of Maxwell equations, a computational code was developed that allows calculation of the propagation of an impulsive signal in the XLPE cable as well as the interaction of this signal with the sensor. An FDTD mesh in which $\Delta r = \Delta z = b/2$; $\Delta t = \Delta r / c$, where b is the thickness of the semicon layer was used.

The PD signal was simulated using a Gaussian pulse of duration 1-3 ns.

A physical quantity used to compare simulation with measurement data is the current. The current flowing along the cable or on the electrode of the sensor can be easily measured using an oscilloscope.

The simulation provides the field values at each node of the FDTD grid. Currents can be derived from the H-field. The input current is calculated using the H-field at the beginning of the cable. It is given by the formula: $i_{inp}(t) = 2 \cdot \pi \cdot r \cdot H_{\varphi}(t)$, where r is the distance of a point between the inner and outer conductors where the field component H_{φ} is calculated.

The simulated output current of the sensor is determined by the current on the electrode, which is calculated from the difference between the fields above (H_{φ}^a) and below (H_{φ}^b) the sensor electrode.

$$i_{outp}(t) = 2 \cdot \pi \cdot (r_a H_{\varphi}^a(t) - r_b H_{\varphi}^b(t)) \quad (39)$$

The output current of the sensor is an important parameter for comparison and optimisation. It is used to estimate the sensitivity of the sensor, which is given by the ratio of the output current to the input current of the sensor.

Even a rather coarse grid, like that used in these calculations, gives reasonable results, as shown in Fig. 59. This figure corresponds to a 30 cm-long sensor with a 2 mm-thick substrate, which is excited by a 1 ns pulse. The maximum output signal corresponds to the measurement data with 7% accuracy. The calculated output signal has smaller width, because for the calculation of the dispersive characteristics of the semicon layers, only average values of material constants were used. Besides, in the theoretical model, no special treatment was applied for the edges of the sensor and the outer shield in the vicinity of the sensor.

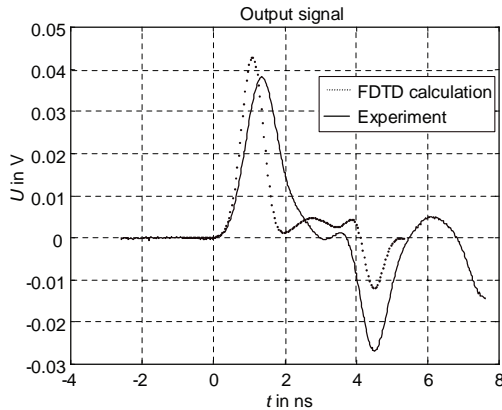


Fig. 59. Output signal of the sensor, simulation and measurement

Fig. 60. shows the dependence of sensitivity on the length of the sensor for 2 mm-thick dielectric and 3 ns pulse width. Measurements were taken for 10, 20 and 30 cm sensor lengths (asterisks).

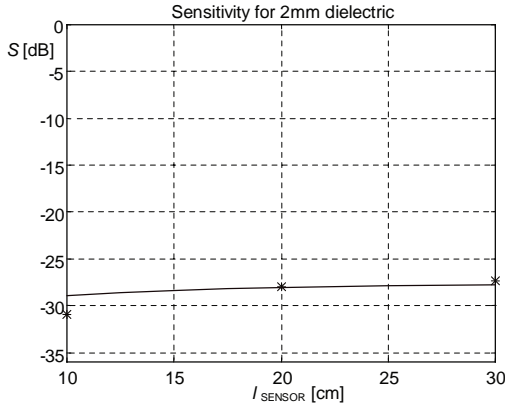


Fig. 60. Sensitivity vs. length of sensor for 3 ns pulse width

The sensitivity increases linearly with the length of the sensor. A longer sensor has a higher inductance, which leads to a higher coupling inductance between the sensor electrode and the inner conductor of the cable, and an increased output signal.

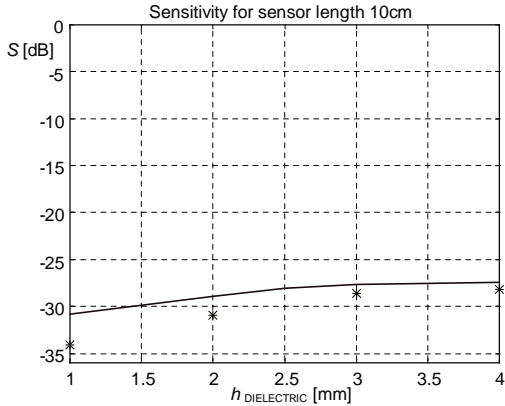


Fig. 61. Sensitivity vs. thickness of the dielectric substrate

Fig. 61. shows the influence of the substrate above the sensor on the sensitivity. The sensitivity increases almost linearly with the thickness of the dielectric substrate. A thicker dielectric substrate leads to a bigger gap between the sensor electrode and the outer shield, thus more energy is coupled in the sensor. The coupling mechanism can be seen in Fig. 62., which shows the H-field (contour plot) in the sensor area for different time steps.

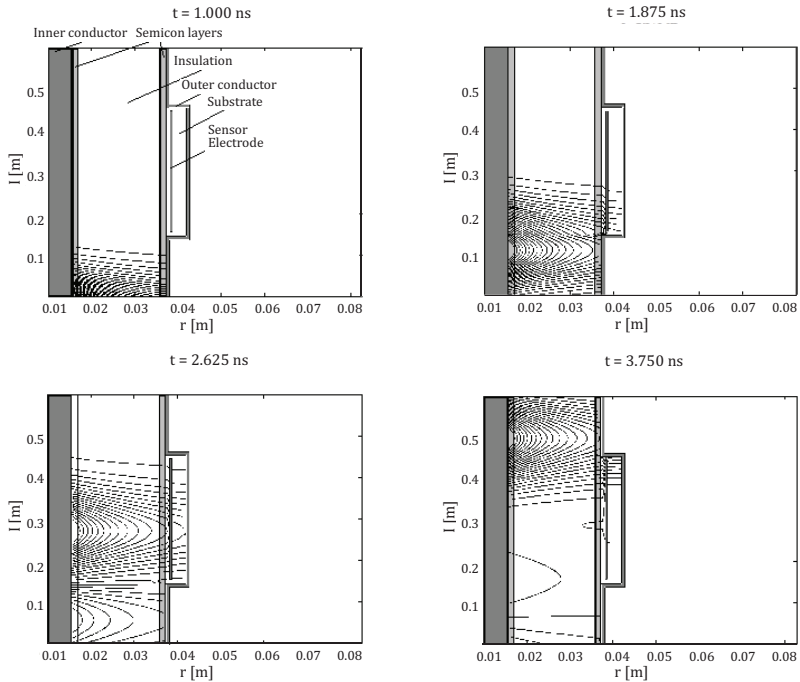


Fig. 62. Contour plot of H-field for different time steps

The pulse signal is applied at the lower end of the cable. After approximately 1.5 ns, the signal reaches the sensor area and the magnetic field couples into the sensor and propagates in the sensor substrate independently from the main signal.

In the frame corresponding to $t = 2.625$ ns, the wave that is reflected from the sensor area starts propagating downwards. After approximately 3.5 ns, the main signal leaves the sensor area and the sensor acts as an attenuated resonator. Such time-dependent field representation gives more insight into the physics of coupling mechanisms.

2.5.3 Conclusions

An FDTD model and an efficient code for the simulation of a radially symmetric PD sensor have been developed. The FDTD code can be used as an additional tool for the development and optimisation of radially symmetric PD sensors as well as for the study of field coupling mechanisms. The dependence of sensitivity on the geometrical characteristics of the sensor has been investigated experimentally and theoretically. The good agreement of simulation and measured data shows that even a relatively simple model can be used to represent important characteristics of the sensor.

2.6 HV Cables for Electric Vehicle Applications

Modelling of cables for HV applications in automobiles is very important since it offers significant benefits in the early stages of system design. It is expected that optimal parameters for the shield structure and the connections of shielded cables to termination devices and vehicle chassis will provide low radiation levels and will be cost effective. This is an area of active development, and the characterisation of shielded cables and installation concepts in automotive HV systems is not yet standardised.

A technique for fast and accurate model generation of HV shielded cables was developed applied these models in order to simulate an electrical power-train system. In this sub-section the validation of the developed methodology by comparison with measurements is presented.

2.6.1 Modelling of a Shielded Power Cable with Single Core: Coroplast 35 mm²

Investigation of the Influence of Shield Parameters

For the investigation of the HV Coroplast FLR2GCB2G 35 mm² shielded cable and the measurement of its shielding performance, the setup shown in Fig. 63. was used. Analysis of the coupling from the HV cable to a single wire is performed in the frequency range 10 kHz to 200 MHz. Corresponding computational models for crosstalk simulation were prepared in EMC Studio, see Fig. 65. and Fig. 66.

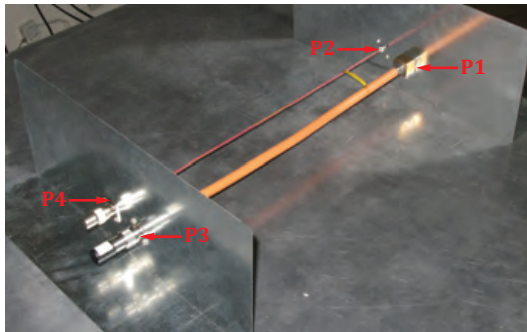


Fig. 63. Measurement setup: single cable and Coroplast 35 mm² cable with adapters



Fig. 64. Measurement sample of Coroplast 35 mm² cable with adapters

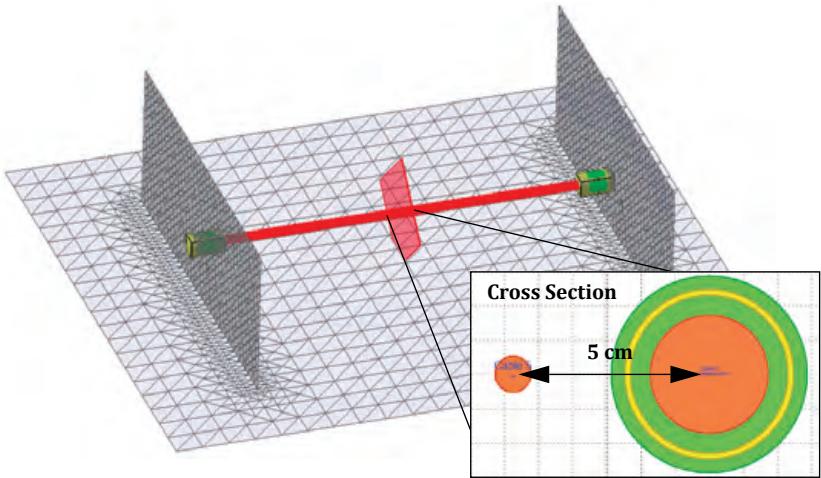


Fig. 65. Computational model for crosstalk analysis using an LCTL scheme of the transmission line

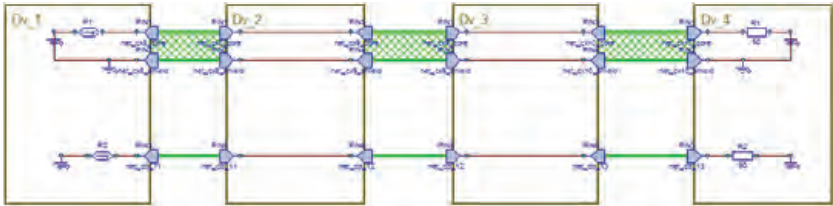


Fig. 66. System diagram for crosstalk calculations



Fig. 67. Layered shield: braided shield with aluminium foil wrapped around it

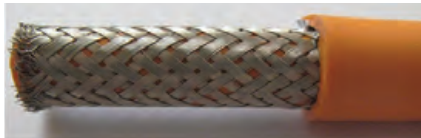


Fig. 68. Braided shield without foil

The HV Coroplast FLR2GCB2G 35.mm² cable has an inner conductor with 35.mm² cross section area and is equipped with a double-layered shield in order to improve shielding effectiveness in the high-frequency range. An aluminium foil on polyethylene (PET) base is wrapped around the main braided copper shield. In order to demonstrate the effect of the foil shield, we considered two Coroplast 35.mm² cable samples: one with a double-layered shield and another one with a braid only, as shown in Fig. 67. and Fig. 68. , respectively. Cable parameters used in the simulation model are listed in Table 5.

Table 5. Parameters of HV cable Coroplast 35.mm²

Inner Conductor	
Number of conductors	1
Radius	4.08 mm
Core material	Copper with 57.6 MS/m
Cable Insulation	
Material: silicon with relative permittivity	3
Loss factor	0.015
Thickness of inner insulation	1.32 mm
Thickness of outer covering	0.75 mm
Layered Shield	
Braided	
Inner diameter of shield	10.8 mm
Thickness of shield	0.3 mm
Filament diameter	0.15 mm
Filaments in carrier	9
Carriers in braid	24
Weave angle	45°
Material	Copper with 57.6 MS/m
Method of transfer impedance calculation	"Kley"
ALU-PET Foil	
Material (aluminium)	20.3 MS/m
Thickness of shield	0.01 mm

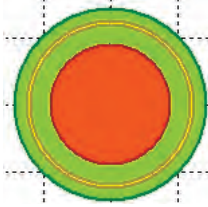


Fig. 69. Cross section of HV cable
Coroplast 35 mm²



Fig. 70. Cable termination with adapter and
N-type connector

Fig. 71. shows the transfer impedance of braided and layered shields, calculated using the Kley model [78].

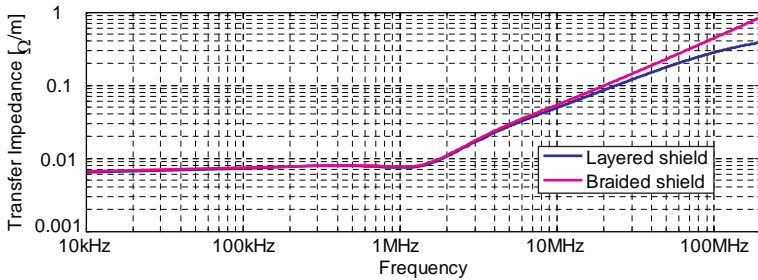


Fig. 71. Transfer impedance of braided and layered shields

Comparison of measurement and simulation results for the transmission coefficients between the HV cable and a single wire is shown in Fig. 72.

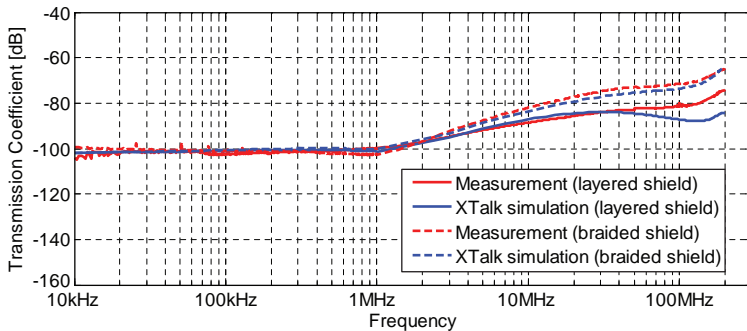


Fig. 72. Transmission coefficient vs. frequency

The results show that in the low frequency range (up to 1 MHz), the coupling to a single wire is constant, is the same for both shields and it depends only on the DC shield resistance. The DC shield resistance depends on the shield material and thickness. Since the braided shield has a much bigger thickness than aluminium foil, this resistance is defined by the braided layer. At higher frequencies the field penetrates through holes in the braid and the coupling to the victim wire increases with frequency (Fig. 72. dashed lines). In this range we can clearly see the influence of the foil shield (Fig. 72. solid lines), which helps to reduce the coupling by 10 dB in the frequency range above 20 MHz.

Investigation of Contact Resistance

Another important factor that affects the shielding performance of the system is the contact resistance between the cable shield and the coaxial connector. This resistance should be as low as possible in order to ensure good electrical contact in the critical radiofrequency (RF) return path from the cable shield to the metallic enclosure. However, ageing of the connector and cable shield leads to increased contact resistance (from 0.01 m Ω up to 100 m Ω , or even higher) and to degradation of the shielding performance. To investigate the influence of contact resistance by measurements, two samples of Coroplast 35mm² cable of the same length and special adapters to N-type connector were prepared (Fig. 73.). In one sample the cable shield was soldered to an adapter box (for both terminations of the cable), providing good 360° contact resistance. In the second sample, for both cable terminations, a 360° slot was cut in the shield and was connected to the adapter box using 16 SMD 1 Ω resistors. These 16 resistors were connected in parallel, giving a total resistance of 62 m Ω . The general measurement setup shown in Fig. 63. was used to measure the coupling to a single cable.

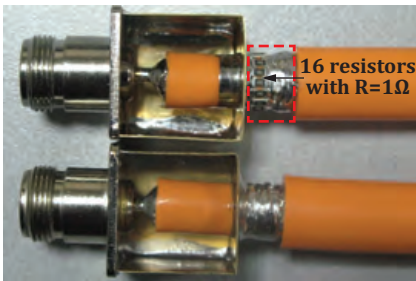


Fig. 73. HV cable samples with perfect and resistive connections between the cable shield and the adapter box

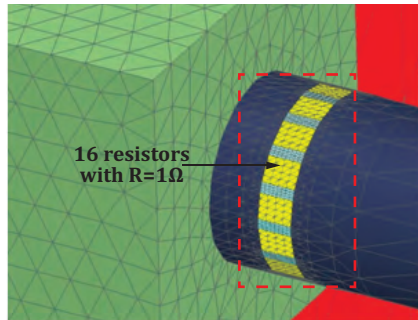


Fig. 74. Model for MoM calculations with solid shield and 16 SMD resistors

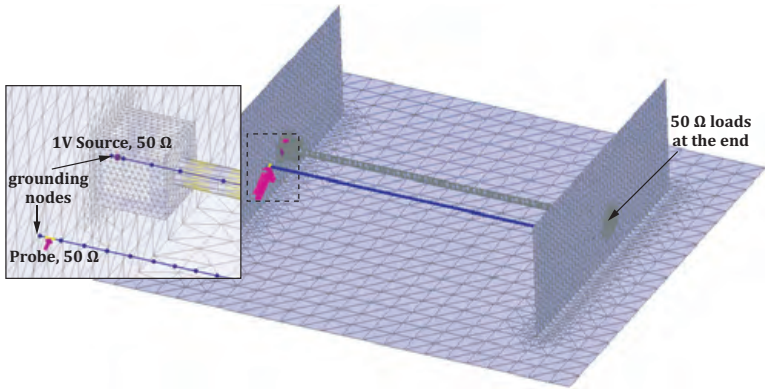


Fig. 75. Model for 3D simulations using MoM

In order to perform simulations of a cable with imperfect (resistive) connection to the shield, a 3D model constructed for full-wave analysis using MoM was considered, as shown in Fig. 75. To model the inner connector of the cable, wire segments of corresponding radius having dielectric coating of corresponding thickness were used. To model the shield, a solid surface represented by triangles was used, and frequency-dependent conductivity, corresponding to the conductivity of a real double-layered shield, was applied to these triangles. SMD resistors (at each termination of the cable) were modelled with 16 triangulated patches with the appropriate surface conductivity in order to obtain $1\ \Omega$ resistance for each patch.

The results of modelling and simulations are presented in Fig. 76.

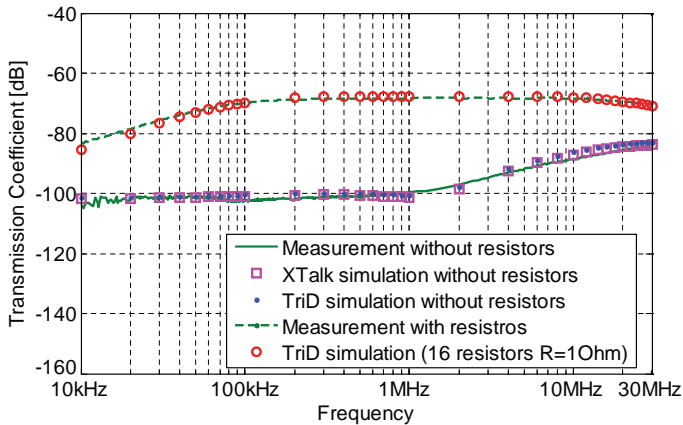


Fig. 76. Influence of contact resistance

Based on the correspondence between measured and simulated values, it was possible to determine the capabilities and accuracy of the simulation models. Comparing signals coupled from a shielded cable with perfect connection and a cable with resistors, we can see that the shielding performance is reduced by 30 dB in the low-frequency range.

2.6.2 Modelling of Shielded Power Cable with Single Core: Coroplast 25 mm²

For the investigation of the Coroplast FLR2GCB2G 25_mm² shielded cable (inner conductor with 25_mm² cross-section area), the same measurement setup and simulation model (with the corresponding parameters of shielded cables) as those shown in Fig. 63. - Fig. 66. are used.

Table 6. Parameters of the HV cable Coroplast 25_mm²

Inner Conductor	
Number of conductors	1
Radius	3.3 mm
Core material	Copper with 57.6 MS/m
Cable Insulation	
Material: silicon with relative permittivity	3
Loss factor	0.015
Thickness of inner insulation	1.1 mm
Thickness of outer covering	0.75 mm
Layered Shield	
Braided	
Inner diameter of shield	8.8 mm
Thickness of shield	0.294 mm
Filaments diameter	0.147 mm
Filaments in carrier	9
Carriers in braid	24
Weave angle	17°
Material	Copper with 57.6 MS/m
Method of transfer impedance calculation	"Kley"

ALU-PET Foil	
Material (Aluminium)	20.3 MS/m
Thickness of shield	0.01 mm

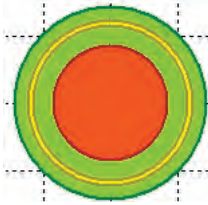


Fig. 77. Cross section of HV cable
Coroplast 25 mm²



Fig. 78. Cable termination with adapter and
N-type connector

The transfer impedance of the cable calculated using the Kley model [78] is shown in Fig. 79.

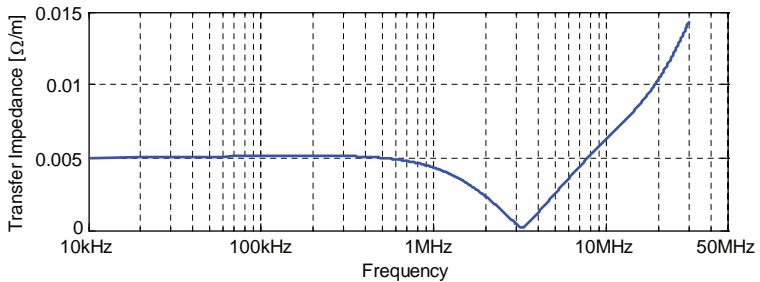


Fig. 79. Transfer impedance of layered shield of the Coroplast 25 mm² cable

In order to validate and evaluate the accuracy of the model, a comparison between the measured and simulated impedances of Coroplast 25 mm² cable sample with 50 Ω termination load is shown in Fig. 80.

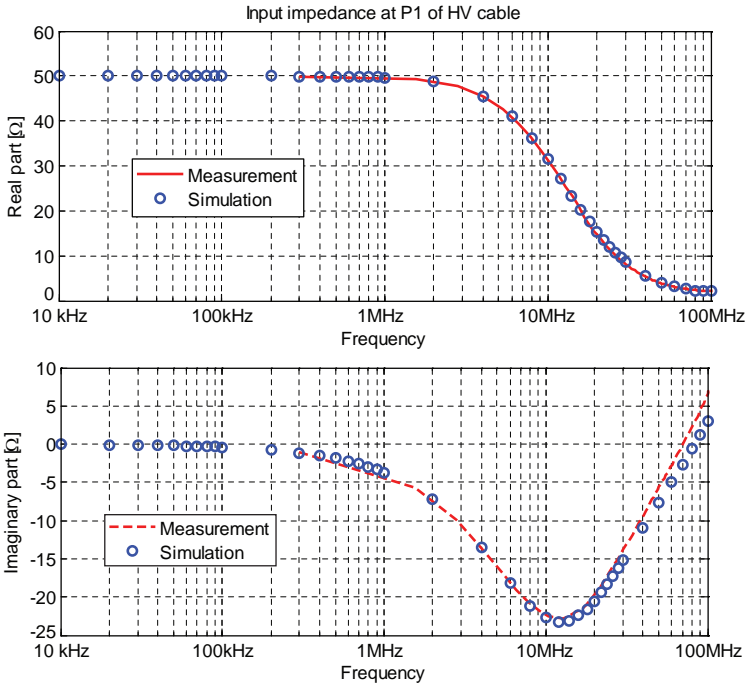


Fig. 80. Input impedance at Port1 of Coroplast 25 mm²

Comparison of measurement and simulation results for the transmission coefficient between an HV cable and a single wire is shown in Fig. 81.

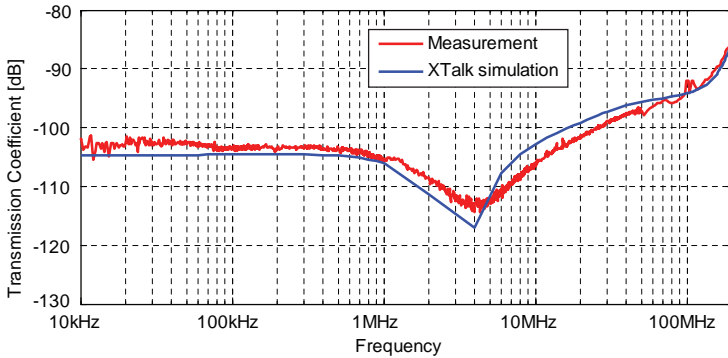


Fig. 81. Transmission coefficient between shielded cable and single wire vs. frequency

Comparing the coupling to victim wire from Coroplast 35 mm² and Coroplast 25 mm² cables, both with double shields (copper braid + aluminium foil on PET base), we can see that, in the low-frequency range, coupling is constant and is the same for both cables.

2.6.3 Conclusions

The results presented here demonstrate the simplicity of model generation and the high accuracy of the approach. The developed models were used in a number of industrial applications.

CHAPTER 3

SIMULATION OF LOW-FREQUENCY MAGNETIC FIELDS IN AUTOMOTIVE EMC PROBLEMS

3.1 Introduction

This chapter presents a study of automotive EMC problems that are dominated by low-frequency magnetic fields with a frequency ranging from DC to several MHz [90]. The geometries of typical vehicles are modelled by complex 3D surfaces. These vehicle bodies are often made of steel, which is highly conductive and has a magnetic permeability that depends on frequency. The steel that is used is often thin relative to the overall vehicle size, ranging from fractions of a millimetre to a few millimetres. At low frequencies the skin depth exceeds the steel thickness, while at higher frequencies the skin depth is smaller than the steel thickness, making it merely difficult to generalise simulations based on a single approximation (e.g., an approximation of the material RF transparency) over a frequency range from DC to several MHz.

In many cases low-frequency automotive EMC problems involve cables and magnetic antennas, including coil antennas, which are used typically for contactless battery charging of electric cars and communication coil-type antennas, which are used for smart entry systems. These antennas usually contain ferrites, which have strongly frequency-dependent permeability and loss. Thus, in many practical EMC problems, thin steel sheets must be considered together with wires and ferrite-containing components.

The choice of the numerical approach for modelling low-frequency automotive EMC problems is influenced by issues relating to the complexity of the following procedures:

- Modelling geometries that have thin dimensions compared to the dimensions of the overall problem.
- Modelling low-frequency fields, from DC to several MHz.
- Modelling materials that have both high conductivity and frequency-dependent complex magnetic permeability.
- Modelling ferrites with high complex permeability that depends on frequency.

- Modelling complex 3D geometries that contain objects that are highly separated in free space.
- Simultaneous modelling of surfaces, wires and magnetic and/or dielectric objects.

Considering these factors, the various accepted approaches of computational electrodynamics have their own individual advantages and disadvantages. For example, methods based on finite-volume or finite-difference schemes can be advantageous for simulations that contain multiple materials, as well as for modelling the properties of electromagnetic materials. However, these methods require the whole space of the problem to be discretised in the computational domain. When applied to automotive EMC problems that contain large-scale models that have thin sheets with many small details, these methods require an inhomogeneous mesh with many cells. Simulating long, bent wires in these methods can also require significant computational resources and does not always lead to a stable solution. In contrast, computational methods based on surface integrals do not require volume discretisation. Instead, these methods require surface meshes and they allow for more natural modelling of thin wires. The solution of the surface integral equations can be obtained in the computational domain using MoM.

Using MoM, the thickness of a material can be accounted for by performing an analytical model reduction, thus removing the need to discretise the volume inside the thin steel sheets [91], [92]. This approach has been used successfully with surface integrals to calculate low-frequency magnetic fields [93] - [102]; these methods have mainly used approaches that consider eddy currents on the surface of the steel sheet. Although magnetic fields dominate in these problems, electric charges are also present when the sources of the magnetic fields are close to edges or gaps in conductive surfaces, as is common in automotive applications. These charges induce electric fields that are essentially decoupled from the magnetic fields. In the presence of charges, obtaining an accurate field solution requires consideration of both the electric and magnetic fields [91], [92], [103], [104]. The accuracy of these solutions can be improved by accounting for the deviation of the electric and magnetic fields near wedges [105]. At low frequencies, decoupling of the electric and magnetic fields causes the 'breakdown' of the solution [106] - [113]. One solution to this low-frequency instability problem is to split unknown currents into solenoidal and non-solenoidal parts [107], [110], [111]. The well-known classical basis functions that separate the solenoidal and non-solenoidal parts are the loop-star basis and loop-tree basis, respectively. Properly normalised, this approach allows one to construct a solution from an adequate, balanced system of linear algebraic equations. The literature (of which a representative sample is cited here) mainly describes cases of applying this approach to perfectly conducting bodies.

The simulations considered in the present chapter formulate the MoM based on a new concept of decomposing single- and double-layer equivalent currents (generating radiation fields from thin sheets) into solenoidal and non-solenoidal components. Surface layers of charges and currents are well known in EM theory and they are closely related to the method of fundamental solutions (MFS) for solving electromagnetic problems.

A review of MFS has been published in [114]. Unlike most approaches to solving low-frequency problems [106] - [113], here the problem is solved in two stages, as described in [111]. A new MoM formulation is presented and used to analyse a variety of boundary conditions. To account for the magnetic and conductive properties of materials with finite thicknesses, Mitzner's boundary conditions are used [91], [92]. For highly conductive materials, Leontovich's impedance conditions are applied. For magneto-dielectric bodies, classical boundary conditions are used for the tangential components of the electric and magnetic fields. For perfect electrical conductors (surfaces and wires), the boundary conditions for the tangential component of the electric field are satisfied. The proposed two-stage solution takes less time to calculate results than traditional solutions while preserving the correct EM phenomena. In applications dominated by magnetic fields, the solenoidal currents are assumed to be the main contributors to the magnetic field. The solenoidal currents are obtained in the first stage of the solution. Determining the electric fields requires solution of a quasi-electrostatic problem, performed in the second stage of the solution. The simulation time can differ significantly between the traditional (full-wave) solution and the two-stage solution. If the full-wave problem is formulated for N triangles, then the two-stage approach used here requires solving two problems, the first problem with $\sim N/2$ unknowns and the second problem with $\sim N$ unknowns. The two-stage solution is approximately three times faster than the full-wave solution. For problems where magnetic fields dominate, the proposed solution is approximately eight times faster than the full-wave solution.

This chapter is organised as follows:

- Paragraph 3.2 gives the details of the proposed method.
- Paragraph 3.3 validates the proposed method and compares it to field solutions with numerical simulations, semi-analytical solutions, and measured data (when available) for thin plates and spherical shells.
- Paragraph 3.4 demonstrates the capabilities of the developed numerical solution in analysing low-frequency magnetic fields emitted by power cables in vehicles. The magnetic fields inside a car cabin near a cable are measured and those measurements are compared to simulated data. The magnetic field distribution near a cable in cars with bodies made from steel, aluminium and carbon are then compared.

- Paragraph 3.5 details investigations of the magnetic fields radiated by ferrite-coil antennas, as commonly used in automotive smart entry systems.
- Paragraph 3.6 presents a methodology for optimising smart entry systems and the advantages of using simulations based on the proposed method.
- Paragraph 3.7 shows that the proposed method is able to quantify the fields radiated by an automotive contactless charging system.

3.2 Theoretical Background

This section considers low-frequency problems involving thin sheets of material along with wires and solid magneto-dielectric bodies. In order to exclude the interior of a thin 3D structure from the computational domain, approximate boundary conditions (BC) are applied, as introduced by Mitzner [91], [92]:

$$-\hat{n} \times E^+ + Z_c \cdot \hat{n} \times (\hat{n} \times H^+) + e^{-\alpha} \cdot [\hat{n} \times E^- - Z_c \cdot \hat{n} \times (\hat{n} \times H^-)] = 0, \quad (40a)$$

$$\hat{n} \times E^- + Z_c \cdot \hat{n} \times (\hat{n} \times H^-) + e^{-\alpha} \cdot [-\hat{n} \times E^+ - Z_c \cdot \hat{n} \times (\hat{n} \times H^+)] = 0, \quad (40b)$$

where \hat{n} is the normal vector to the surface of the sheet, E and H are the total electric and magnetic fields, respectively, and the + and - superscripts indicate the upper and lower sides of the sheet, respectively, i.e., for the sides facing toward the normal \hat{n} (+) and away from it (-).

The material of the sheet is characterised by a wave impedance $Z_c = \sqrt{\mu/\varepsilon}$, where $\varepsilon = \varepsilon_0 \varepsilon_r - \sigma/i\omega$ and $\mu = \mu_0(\mu'_r + i\mu''_r)$ are the complex permittivity and permeability, respectively, ε_r is the relative permittivity, σ is the conductivity, and μ'_r and μ''_r are the real and imaginary parts of the relative permeability, respectively. All of these material parameters may be frequency dependent. The time dependence is assumed to be $\exp(-i\omega t)$. Note that the electric and magnetic fields, E and H in (1), should be calculated only outside the thin sheet since doing so inside the sheet is unnecessary.

The material comprising the sheet can be described by the wave impedance Z_c and the complex attenuation $\alpha = -ikd$, where $k = \omega \cdot (\mu)^{1/2} \cdot (\varepsilon)^{1/2} = k' + ik''$ is the wavenumber of the material, ω is the angular frequency, and d is the thickness of the sheet. By introducing the skin depth of the material $\delta = 1/k''$, Mitzner's BCs in (1) are suitable not only for electrically thin sheets with $d/\delta < 1$, but also for thick sheets with $d/\delta \geq 1$. For highly conductive, thin materials, α can be described as $\alpha = (1-i)d/\delta$, so that the coefficient $e^{-\alpha}$ decays exponentially as d/δ increases. Thus, when the skin depth δ becomes much smaller than the sheet thickness, the fields on both sides of the sheet become independent, reducing Mitzner's BCs in (1) to Leontovich's BC [115]:

$$\begin{aligned} -\hat{n} \times E^+ + Z_c \cdot \hat{n} \times (\hat{n} \times H^+) &= 0, \\ \hat{n} \times E^- + Z_c \cdot \hat{n} \times (\hat{n} \times H^-) &= 0. \end{aligned} \quad (41)$$

For wires, a zero tangential electric field BC on the surface of the wire is used. For magneto-dielectric objects, continuity of the tangential components of both the electric and magnetic fields on the object surface is applied.

The main objective of this chapter is to obtain low-frequency fields that satisfy both the BCs and Maxwell's equations. Following [116] and [100], the fields outside the thin sheet can be represented by single- and double-layer currents inside the sheet. These current types produce electric and magnetic fields that satisfy the corresponding BCs and Maxwell's equations [117], [118]. Additionally, these currents can be assumed equivalent to the surface currents on both sides of the thin sheet.

For thin sheets that form a closed surface, it is possible to decouple the interiors and exteriors of the sheets, and to describe the fields by single-layer electric currents. The electric currents on the + surface J_+ radiate only outward, not inward. Likewise, electric currents on the - surface J_- radiate only inward. These behaviours form the null-field approximation [119], which can also be applied with some accuracy to cases where an open surface can be considered as a 3D model of an infinite surface without any significant edge effects. For example, an infinite plate can be modelled as a sufficiently large finite plate for which the incident sources do not excite edge currents or charges. Applying the null-field approximation in this case supports the idea of decoupling the subspaces that connect the upper and lower surfaces of the plate.

As mentioned earlier, in order to prevent low-frequency breakdown in the field solution, the single- and double-layer electric currents $J^{S,D}$ can be represented as a combination of solenoidal $J_M^{S,D}$ and non-solenoidal (irrotational) $J_E^{S,D}$ components, following [120]:

$$J^{S,D}(\mathbf{r}) = J_M^{S,D} + J_E^{S,D}, \quad (42)$$

where $\nabla \cdot J_M^{S,D} = 0$; $\nabla \times J_E^{S,D} \approx 0$.

Based on (42), the scattered fields can be decomposed into:

$$E^{sc} = E_M^{sc} + E_E^{sc}; \quad H^{sc} = H_M^{sc} + H_E^{sc}. \quad (43)$$

These fields, generated by single- and double-layer currents inside the sheet, can be represented outside the sheet as follows:

$$E^{sc}(\vec{r}) = iZ_0 k_0 \int_S \{ J^S(r') G^S(r, r') + J^D(r') G^D(r, r') \} ds' - \frac{iZ_0}{k_0} \nabla \int_S \{ \nabla' J^S(r') G^S(r, r') + [\nabla' J^D(r')] G^D(r, r') \} ds', \quad (44a)$$

$$H^{sc}(\vec{r}) = \int_S [J^S(r') \times \nabla G^S(r, r') + J^D(r') \times \nabla G^D(r, r')] ds', \quad (44b)$$

where the single-layer Green's function $G^S(r, r')$ and the double-layer Green's function $G^D(r, r')$ are defined as follows:

$$G^S(r, r') = \frac{1}{4\pi R} e^{ik_0 R}, \quad G^D(r, r') = \frac{1}{4\pi} \frac{\partial}{\partial n} \left(\frac{e^{ik_0 R}}{R} \right), \quad (45)$$

where $R = |r - r'|$, r is the position vector of the observation point, r' is the position vector of the source point located in the middle of the upper and lower surfaces, and $k_0 = \omega \sqrt{\varepsilon_0 \mu_0}$ is the free-space wavenumber. The superscripts S and D denote the single and double layers, respectively.

Substituting the total fields $\mathbf{E} = \mathbf{E}_{inc} + \mathbf{E}^{SC}$ and $\mathbf{E} = \mathbf{H}_{inc} + \mathbf{H}^{SC}$ into the relevant BCs, we obtain a system of integral equations for the unknown currents \mathbf{J}_M and \mathbf{J}_E . The basis and testing functions for the MoM solution can be constructed as described in [106]. Following this MoM scheme, we assume that the sheet surface is divided into N patches and that the objective is to obtain the solenoidal and irrotational components of the current \mathbf{J}_v^p for each patch, where $p = S, D$ (for the single- and double-layer equivalent currents) or $p = +, -$ (for the currents on the surfaces of the sheet), and $v = M, E$.

The corresponding currents are now represented as:

$$\mathbf{J}^p(\vec{r}) = \sum_{i=1}^{N_s} I_M^p(i) \cdot \mathbf{J}_M^p(i) + \sum_{i=1}^{N_l} I_E^p(i) \cdot \mathbf{J}_E^p(i), \quad (46)$$

where $\mathbf{J}_M^p(i)$ and $\mathbf{J}_E^p(i)$ are the vector basis functions, tangential to the surface of the sheet, and N_s, N_l are numbers of solenoidal and irrotational currents, respectively. The general requirements for constructing \mathbf{J}_M and \mathbf{J}_E are described in [106]. In (46), I_M^p and I_E^p are unknown coefficients that must be determined. Rewriting the corresponding integral equations in a linear MoM system of algebraic equations, we obtain:

$$\begin{bmatrix} \mathbf{Z}_{MM} & \mathbf{Z}_{ME} \\ \mathbf{Z}_{EM} & \mathbf{Z}_{EE} \end{bmatrix} \cdot \begin{bmatrix} \mathbf{I}_M \\ \mathbf{I}_E \end{bmatrix} = \begin{bmatrix} \mathbf{V}_M \\ \mathbf{V}_E \end{bmatrix}. \quad (47)$$

Each block matrix \mathbf{Z}_{uv} in (47) represents the self- or mutual-influence of the solenoidal and non-solenoidal currents, where the subscript uv may take any of the values MM, ME, EM or EE . The block matrices can also be written as:

$$\mathbf{Z}_{uv} = \begin{bmatrix} \mathbf{Z}_{uv}^{1s} & \mathbf{Z}_{uv}^{1d} \\ \mathbf{Z}_{uv}^{2s} & \mathbf{Z}_{uv}^{2d} \end{bmatrix}. \quad (48)$$

For Mitzner's BC (40), the submatrices in (47) have the following elements:

$$\begin{aligned} Z_{uv}^{tp}(i, j) = & (-1)^t e_{uv}^{+p}(i, j) + Z_c(i) h_{uv}^{+p}(i, j) \\ & + e^{-\alpha(i)} \cdot [(-1)^{(t-1)} e_{uv}^{-p}(i, j) - Z_c(i) h_{uv}^{-p}(i, j)] \end{aligned} \quad (49)$$

where the superscript $t = 1, 2$ is used to distinguish the two equations in (1).

$e_{uv}^{\pm p}(i, j)$ and $h_{uv}^{\pm p}(i, j)$ are represented by:

$$e_{uv}^{\pm p}(i, j) = \langle w_u(i), \hat{n}(i) \times E_v^{\pm p}(i, j) \rangle, \quad (50)$$

$$h_{uv}^{\pm p}(i, j) = \langle w_u(i), \hat{n}(i) \times (\hat{n}(i) \times H_v^{\pm p}(i, j)) \rangle, \quad (51)$$

where $E_v^{\pm p}(i, j)$ and $H_v^{\pm p}(i, j)$ are the electric and magnetic fields calculated on the + or - sides of the i -th patch, produced by the solenoidal ($v = M$) or non-solenoidal ($v = E$) components of the single-layer ($p = s$) or double-layer ($p = d$) currents, while $w_u(i)$ is the appropriate testing function. The fields are integrated over the surface S of the j -th patch as follows:

$$\langle A(r), B(r) \rangle = \int_S A(r) \cdot B(r) ds. \quad (52)$$

The voltage subvectors on the right-hand side of (8) are calculated as follows:

$$V_u = \begin{bmatrix} V_u^1 \\ V_u^2 \end{bmatrix}, \quad (53)$$

where the superscripts 1 and 2 are used to distinguish between the two equations in (40), which produce appropriate matrix elements. For example,

$$\begin{aligned} V_u^1(i) = & \langle w_u(i), \hat{n}(i) \times E_{inc}^+(i) \rangle + \\ & Z_c(i) \cdot \langle w_u(i), \hat{n}(i) \times (\hat{n}(i) \times H_{inc}^+(i)) \rangle - \\ & e^{-\alpha(i)} [\langle w_u(i), \hat{n}(i) \times E_{inc}^-(i), \rangle \\ & Z_c(i) \cdot \langle w_u(i), \hat{n}(i) \times (\hat{n}(i) \times H_{inc}^-(i)) \rangle] \end{aligned}$$

The unknown coefficients in (47) form the vectors

$$I_v = \begin{bmatrix} I_v^s \\ I_v^d \end{bmatrix}. \quad (54)$$

For closed thin shells, the single-layer electric currents \mathbf{J}_+ and \mathbf{J}_- are used, which radiate toward and away from the normal, respectively. For a closed surface that represents the outer surface of a voluminous object, two possible cases are considered. For the

first case, where the voluminous object is highly conductive, Leontovich's BC is . PLEASE CHECK] applied and only single-layer electric currents radiating outside the object are assumed. For the second case, where the voluminous object is slightly conductive or insulating, single-layer electric and magnetic currents are used.

When the free-space wavenumber is sufficiently small, according to [111] the following two problems must be solved:

Problem 1.

$$\begin{bmatrix} Z_{MM}^{1S} & Z_{MM}^{1D} \\ Z_{MM}^{2S} & Z_{MM}^{2D} \end{bmatrix} \cdot \begin{bmatrix} I_M^S \\ I_M^D \end{bmatrix} = \begin{bmatrix} V_M^1 \\ V_M^2 \end{bmatrix}. \quad (55)$$

The superscripts 1 and 2 are used to distinguish the two equations in (40). The solenoidal currents are solved in the system of equations in (55). These currents are substituted as known currents into *Problem 2*.

Problem 2.

$$\begin{bmatrix} Z_{EE}^{1S} & Z_{EE}^{1D} \\ Z_{EE}^{2S} & Z_{EE}^{2D} \end{bmatrix} \cdot \begin{bmatrix} I_E^S \\ I_E^D \end{bmatrix} = \begin{bmatrix} V_E^1 \\ V_E^2 \end{bmatrix} - \begin{bmatrix} Z_{EM}^{1S} & Z_{EM}^{1D} \\ Z_{EM}^{2S} & Z_{EM}^{2D} \end{bmatrix} \cdot \begin{bmatrix} I_M^S \\ I_M^D \end{bmatrix}. \quad (56)$$

Equation (55) is sufficient when only considering the magnetic fields, in which case the number of unknowns is much smaller than the number of unknowns in the full solution for (47). When also considering the electric fields, (56) should also be solved. Note that solving (55) and (56) separately is more efficient than solving (47) directly. In the current implementation of (55) and (56), the basis functions for J_M are used, as described in [120]. For J_E the tree basis functions are used, as described in [109] - [113], [121]. The testing functions are chosen to be the same as the basis functions.

The proposed method was tested in the commercial solver LFMF, which is part of the EMC Studio software package [1].

3.3 Method Validation

3.3.1 Investigation of Shielding Effectiveness with an Infinite Plane

The accuracy and applicability of the developed approach was validated in several configurations. In this subsection, the shielding effectiveness of an infinite plane is calculated.

Consider the configuration defined by Moser in [122], which defines analytical integral expressions for the low-frequency EM field of a circular loop. The loop is located beside an infinite thin-plane metal sheet (see Fig. 82.). According to [122], the shielding effectiveness of the metal sheet is defined as a voltage drop (in decibels) induced by placing the shield between the two loops:

$$\text{Shielding Effectiveness} = 20 \cdot \log_{10} \left(\frac{V_2'}{V_2} \right), \quad (57)$$

where V_2' is the voltage measured in Loop 2 upon removing the shield and V_2 is the voltage measured in Loop 2 in the presence of the shield (see details in [122] - [124]).

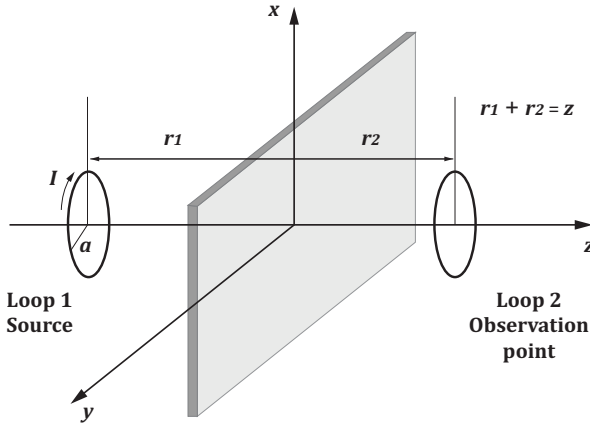


Fig. 82. Coaxial loops separated by an infinite plane [122]

Consider a case where the sheet is made from an aluminium alloy with conductivity $\sigma_{Al} = 0.35 \cdot \sigma_{Cu}$, where the copper conductivity σ_{Cu} is 5.8 MS/m. The thickness of the sheet is $t = 1.5875$ mm. The incident loop is located at distance $r_1 = 5$ cm from the shield, and $r_2 = r_1$. The radius of each loop is $a = 3.5$ cm.

In order to solve the shielding problem of Fig. 82., three numerical techniques are considered. In all of these simulations, the size of the shield is $1.22 \text{ m} \times 1.22 \text{ m}$, which corresponds to the measurement setup described in [122]. This setup allows the detection of data contamination due to edge effects. In the numerical simulations, the plate is meshed with equilateral triangles of edge length 1.0 cm, chosen from the results of convergence studies for each applied method. The first technique is the low-frequency magnetic field (LFMF) approach, which uses the solution of (55). The second technique is the LFMF null-field solution, described in the previous section. The third method is the full-wave MoM solution [1], applied to the surface of an infinitely thin perfect electric conductor (PEC), which is used as a reference at frequencies where the skin depth is smaller than the thickness of the plate.

Fig. 83. compares the results of simulations with Moser's data from [122], showing Moser's analytical solution with a solid line and the measurements from [122] with circles; the crosses show the results obtained by the LFMF approach, and the dotted

line shows the LFMF null-field solution. Fig. 83. also shows the full-wave MoM solution, represented by the dashed line.

The LFMF null-field approach accurately reproduces Moser's results (Fig. 83.). The LFMF approach matches the analytical solution at frequencies below 10 kHz; above 100 kHz this approach yields values of the same order of magnitude as those obtained by the full-wave MoM solver for the PEC surface. At ~ 5 kHz the skin depth is equal to the thickness of the aluminium sheet; at higher frequencies the currents on the lower and upper sides of the surface are partially independent. Additional simulations showed that increasing the size of the plate does not significantly influence the computations of the shielding effectiveness. Calculating the shielding effectiveness using the LFMF or full-wave MoM approach yields values that depend on the discretisation of the plate, making the null-field LFMF solution preferable.

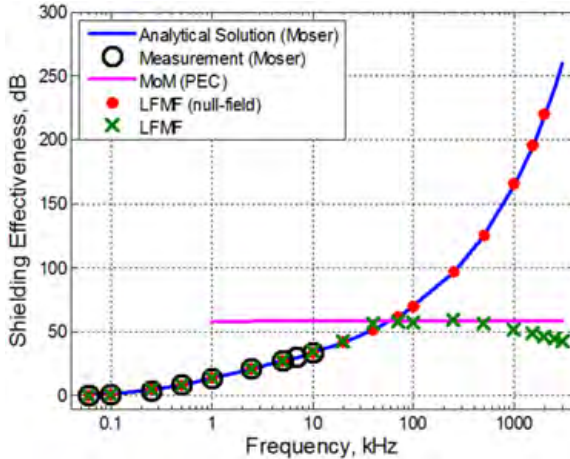


Fig. 83. Shielding effectiveness vs. frequency for a plate made of an aluminium alloy. An infinite plane is used for the analytical solution. For measurement and numerical simulations, the plate has dimensions $1.22 \text{ m} \times 1.22 \text{ m}$ and is comprised of a triangular mesh with edge lengths of 1 cm

3.3.2 Vertical Loop Near a Finite Plate

Consider a vertical loop located near a finite PEC plate, fed by a 1V voltage source, as shown in Fig. 84. The plate has dimensions 50×25 cm. The radius of the loop is 5 cm, and the centre of the loop is located 10 cm above the plate. The edges of the plate accumulate charges, necessitating the use of the two-step solution in order to find the correct field values.

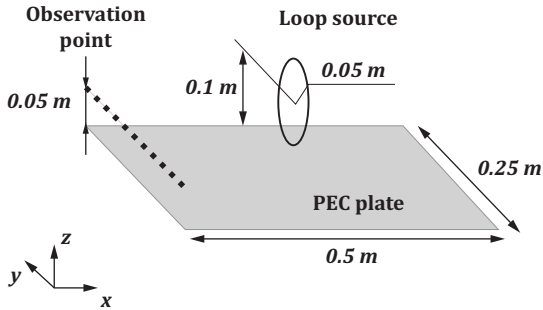


Fig. 84. A vertical loop above a finite plate

Fig. 85. shows the total electric field at various observation points (field probes) located above the edge of the plate (see Fig. 84.). In this case the field solution based only on solenoidal currents is incomplete, especially when compared to the full-wave solution produced by EMC Studio [1]. When irrotational currents are also taken into account, as in the second step of the total solution, the electric fields agree with those produced by the full-wave solution. In this case the plate was meshed with triangles with edge lengths of 1.5 mm. This discretisation yielded sufficiently good results, even without considering special basis functions for the edges [105].

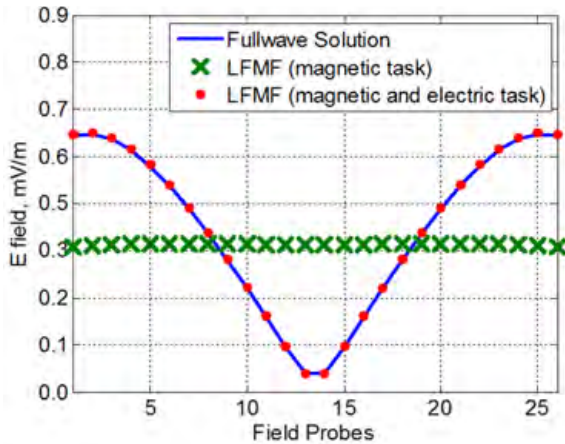


Fig. 85. Total electric E-field at various observation points, located above the edge of a plate (frequency = 10 kHz)

3.3.3 Spherical Shield

For the next example consider a spherical steel shell of radius 0.5 m, thickness 0.1 mm, $\sigma_{al} = 0.35 \cdot \sigma_{cw}$ and $\mu'_r = 112$, $\mu''_r = 0$. The origin of the Cartesian coordinate system is the centre of the sphere. The loop source, which produces a semi-homogeneous field near the sphere, is centred on the z-axis, has radius 0.5 m, and is located 9 m away from the surface of the shell on the XY plane. The observation point of the field is located at the centre of the spherical shell. Fig. 86. compares the shielding effectiveness of the shell calculated using the LFML null-field approach with that calculated by the analytical approach from [125]. Again, the results calculated by these methods are in good agreement.

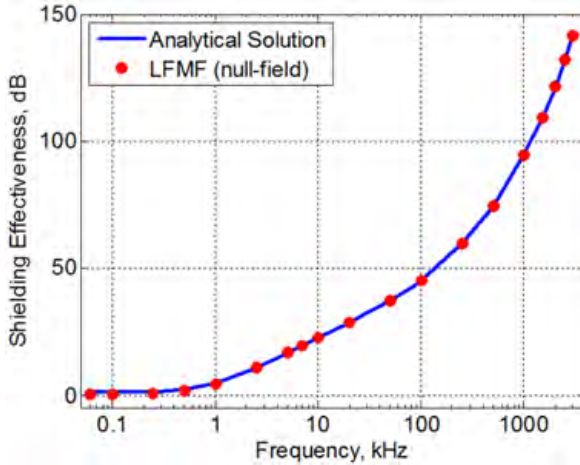


Fig. 86. Shielding effectiveness vs. frequency for a spherical shell

3.4 Magnetic Fields Radiated by an Automotive Power Cable

The magnetic field distribution from a power-supply cable in the presence of a car body made of steel is considered in this section. It is assumed that the permeability for steel depends on frequency according the relaxation model given in [126]:

$$\mu(\omega) = \frac{\mu'(0) - \mu'(\infty)}{1 - i\omega\tau(\omega)} + \mu(\infty), \quad (58)$$

where $\mu'(0)$ and $\mu'(\infty)$ are the low- and high-frequency real relative permeabilities for the relaxation process, respectively, and $\tau(\omega)$ represents a relaxation time that may be complex, which can be obtained by the Cole-Cole representation:

$$\tau(\omega) = \omega^{-\nu} t^{1-\nu} e^{i\nu\pi/2}. \quad (59)$$

In (58)–(59) the following parameters were used: $\mu'(0) = 279$, $\mu'(\infty) = 78$, $1/(2\pi t) = 5$ kHz, $\nu = 0.4$. The electrical conductivity of this steel alloy is $\sigma = 7.18$ MS/m.

In this model, the wire is routed along a typical path close to the driver-side sill board (Fig. 87.). The cable is fed by a 5 A current source. The frequency range is 10 Hz to 150 kHz. The distance from the cable to the car body is 2.5 cm. A field probe is located 9.3 cm away from the cable inside the vehicle cabin. The thickness of the car chassis is 1 mm.

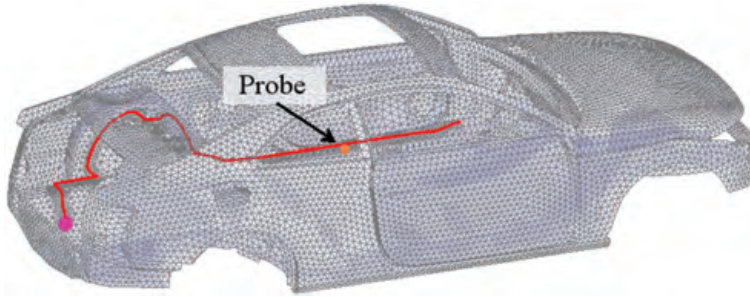


Fig. 87. A model of a car body with a power-supply cable

Car bodies were simulated as being made from four materials: steel, aluminium, carbon and a PEC. For aluminium and carbon, conductivity values $\sigma = 2.03$ MS/m and $\sigma = 1000$ S/m were used, respectively. Fig. 88. compares the simulated and measured results.

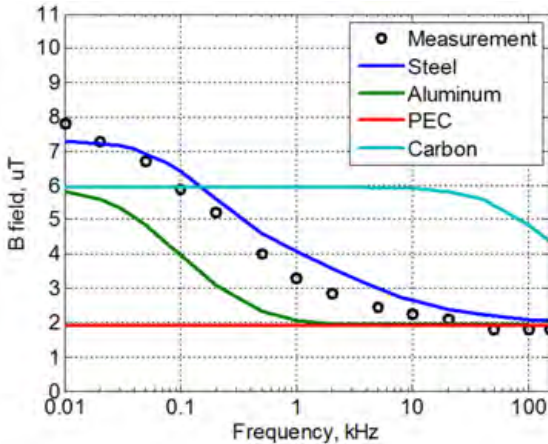


Fig. 88. Comparison of measured and calculated B-field in a car

For the steel body, the simulation data follow the measured data, converging to the PEC results at high frequencies. The simulation of aluminium also begins to converge to the PEC results at high frequencies, where the car body can be considered to be a perfect conductor. The differences between the simulation and measured results of the steel body are caused by two factors: (i) uncertainties in the position of the field probe in the experiment (for a detailed description of the field probe and its modelling, see [101]) and (ii) uncertainties in the thickness of the material.

In order to analyse how making the car body from carbon influences the magnetic field, the near-field magnetic field distribution was calculated at 10 Hz; Fig. 89. shows the distribution of the B-field in the cross section of a car. At low frequencies, the magnetic field penetrates the carbon surfaces. At frequencies higher than several hundreds of kHz, the eddy currents can be significant. For these frequencies the field distributions look similar to those generated for car bodies that are built from a PEC.

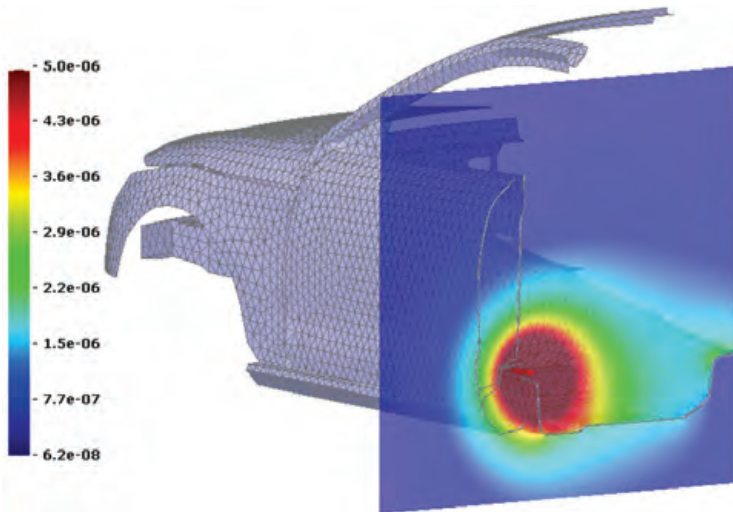


Fig. 89. Distribution of the B-field in the cross section of a carbon car body (frequency = 10 Hz)

3.5 Magnetic Field of a Ferrite-Coil Antenna Near Metallic Structures

In this section the developed methodology is applied to analyse antennas used in an automotive smart-entry system. Smart-entry systems allow the user to remotely open doors, activate electronics and to start the vehicle engine from outside the vehicle without using a mechanical key. A smart-entry system consists of several antennas that transmit and receive information. Some on-board antennas radiate outward from the vehicle, while others radiate toward the operator inside the vehicle. The smart-entry key itself also contains receiving and transmitting antennas. Smart-entry systems are usually operated at two frequencies: (i) low frequency (i.e., 20/125 kHz) for communication from the car (transmitting) to the key (receiving) and (ii) radio frequency (i.e., 315 MHz in USA and Japan; 433/868 MHz in Europe) for communication from the key (transmitting) to the car (receiving). Original equipment manufacturers (OEMs) of automotive vehicles are currently investigating using other additional frequency bands. This section focusses on problems of operating low-frequency on-board antennas located near metallic surfaces.

3.5.1 Ferrite-Coil Antenna in Free Space

Fig. 90. shows a typical low-frequency on-board transmitting coil antenna with a ferrite core used in a smart-entry system. In order to tune the antenna to a resonance frequency of 21.3 kHz, a $0.33 \pm 10\% \mu F$ capacitor is connected in series to the coil.

This antenna was modelled by representing the ferrite as a material with relative permeability $\mu = 2400 + j \cdot 45$ at 21.3 kHz. The field strength inside this material is low enough to neglect saturation effects. The model consists of a ferrite rod with dimensions $7.5 \times 10.0 \times 88.75$ mm and a wire coil with 0.2 mm radius. The distance between the coil and the surface of the ferrite core is 2.5 mm.

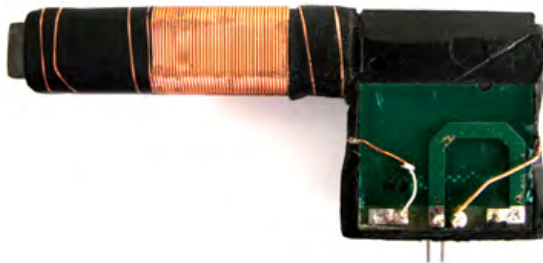


Fig. 90. Coil antenna of a smart-key system

In the test setup, the antenna is fed by a sinusoidal voltage source. The amplitude of this source is regulated in order to obtain a nominal peak-to-peak magnitude (I_{pp}) of

1.1 A for an antenna located in free space. The magnetic field components were detected with a three-axis measuring probe. The diameter of each receiving coil was 10 cm. In order to measure each component of the field independently, the output of each coil was connected to the oscilloscope input. Fig. 91. and Fig. 92. show the measurement setup. Two field components (ρ and φ) were measured. Because the measurement probe was large compared to the distance to the source (95 cm), and because the measured fields were inhomogeneous, the fields were calculated from many observation points inside the probe and integrated over an appropriate surface [101]. The antenna model was constructed according to the sample shown in Fig. 90. In the simulation model, the plastic parts of the antenna and the environment of the experimental setup are neglected.

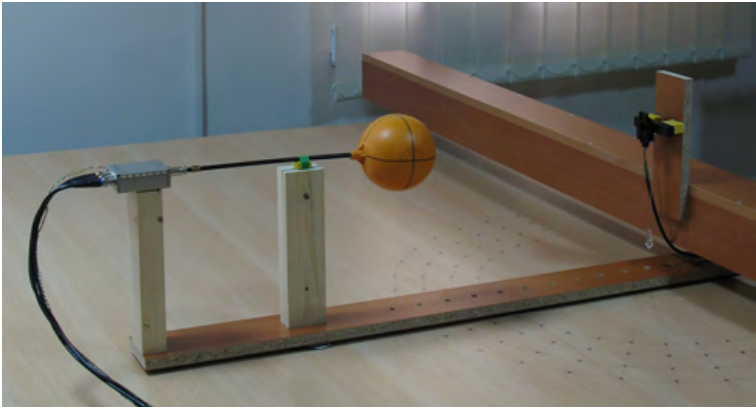


Fig. 91. Measurement setup with antenna in free space

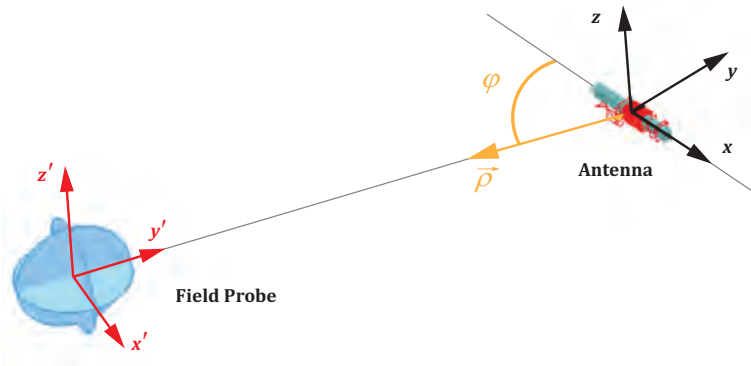


Fig. 92. Transmitting antenna in free space

Fig. 93. and Fig. 94. compare the results of the simulation and measurement with the field probe and antenna centre separated by 95 cm. The difference in the results between the measurements and simulations is less than 3 dB.

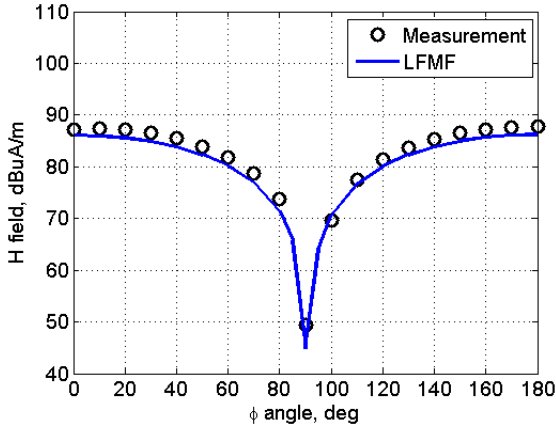


Fig. 93. H-field for antenna in free space, ρ -component

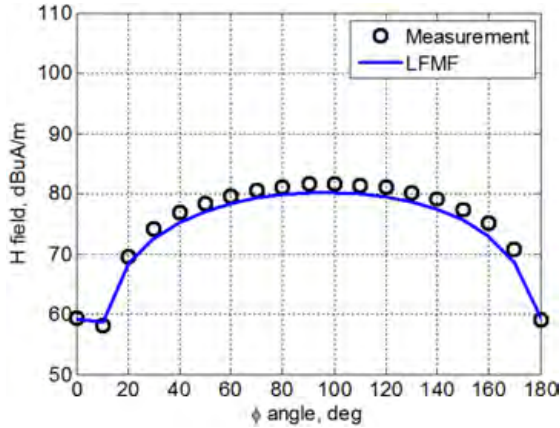


Fig. 94. H-field for antenna in free space, ϕ -component

3.5.2 Antenna with Aluminium Shield: Edge Effect

In the next setup, an aluminium shield ($100\text{ cm} \times 54\text{ cm} \times 6\text{ mm}$) was placed between the transmitting antenna and the field probe. The distance between the antenna and the shield was 5 cm . In this experiment, the antenna was placed near the edge of the shield. The distance from the edge to the centre of the antenna was 5 cm , as shown in Fig. 95.

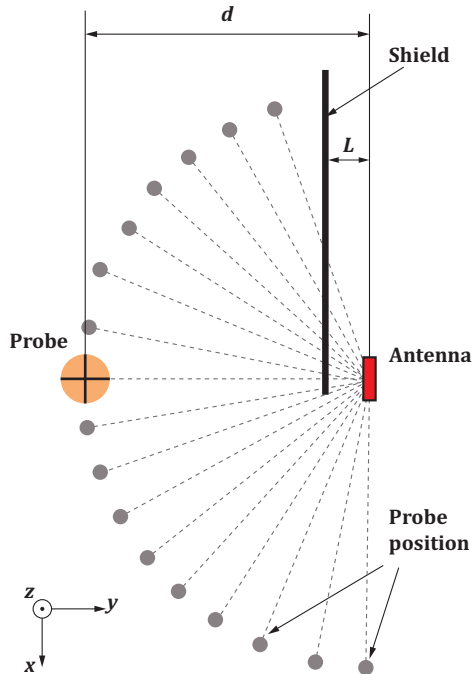


Fig. 95. A transmitting antenna with aluminium shield. Position of the shield: $L=5\text{ cm}$ from the antenna centre. Position of the field probe: $d=95\text{ cm}$ from the antenna centre

Fig. 96. and Fig. 97. compare the results of the measurement and simulation.

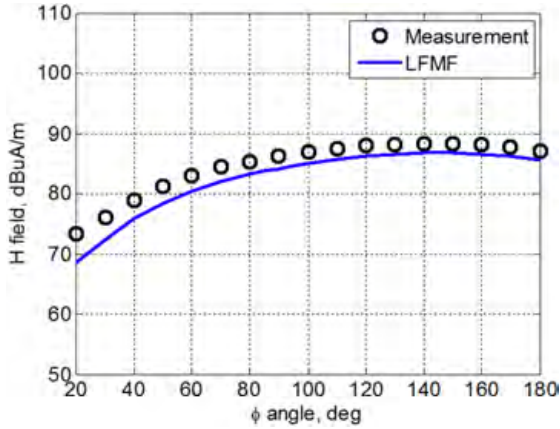


Fig. 96. H-field for the antenna located near the edge of the aluminium shield, ρ -component

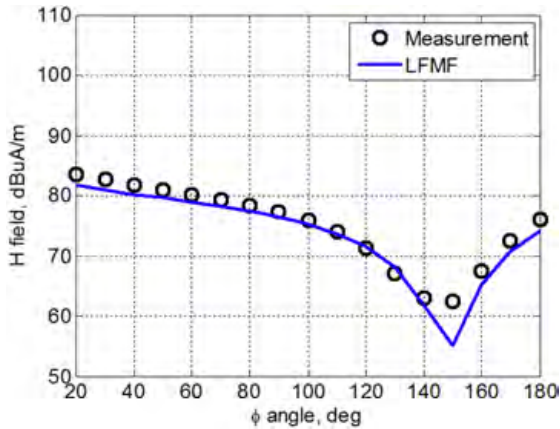


Fig. 97. H-field for the antenna located near the edge of the aluminium shield, ϕ -component

3.6 Analysis and Optimisation of Smart-Entry System Performance

The coverage area of smart-entry systems inside and outside a vehicle can be analysed by using simulation of electromagnetic fields. A typical car has at least three antennas for external coverage (e.g., in both front doors and in the boot) and at least one additional antenna for internal coverage. In order to obtain the best coverage with the smallest number of antennas, the structure and the position of the antennas should be optimised. For external coverage, the objective is to determine the area around a car in which the magnetic field level of each antenna corresponds to a key sensitivity. For internal coverage, it is important to determine the field strength of each antenna inside the car, where the magnetic field amplitude is equal to the key sensitivity. Ideally, a field distribution should have no 'holes' within the cabin and the fields should decay rapidly outside the cabin.

3.6.1 Operation of External Smart-Entry System

For this simulation, several antennas are placed inside the car model, as shown in Fig. 98. Antenna 1 is located in the left hand-side door of the car, Antenna 2 is located in the right hand-side door, and Antenna 3 is located in the rear bumper.

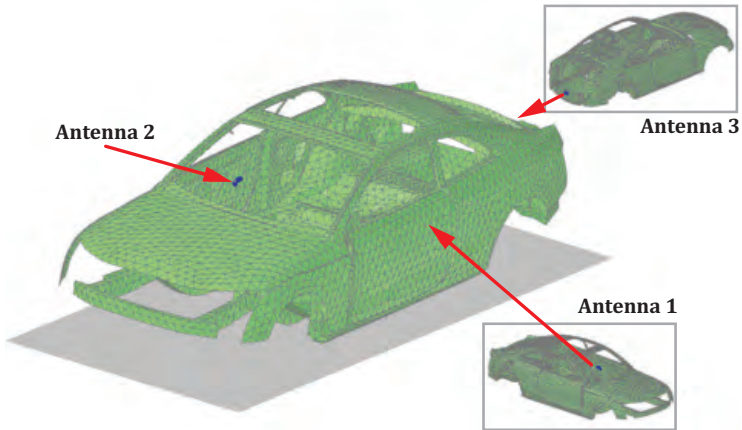


Fig. 98. Positions of three ferrite-rod antennas inside a car model

The typical sensitivity of a receiving antenna is ~ 1 nT, which corresponds to a magnetic field of $H = 0.79$ mA/m. In these simulations, the magnitude of the magnetic field can be calculated in a pre-defined range around the car model, allowing estimation of the area of signal coverage for different car/antenna configurations.

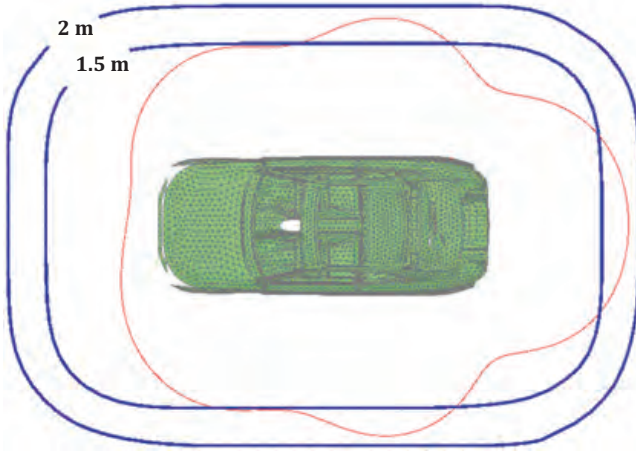


Fig. 99. Isoline representation of the B-field at 1 nT

Fig. 99. shows the isolines for the B-field of three antennas operating at a sensitivity of 1 nT. The blue lines show the maximum operating range for a smart-entry key, which, for this model, is 1.5 – 2 m from the car. In these simulations, each antenna is fed initially by a 1 V voltage source. In order to achieve the necessary field levels, the fields generated by the source are processed; the current magnitude and phase in each of the antennas are then varied.

Next, internal coverage is assessed by calculating the area of effective coverage inside a 3D model of a car. Fig. 100. shows the isosurface of a 1 nT B-field in the presence of a car. This isosurface shows a boundary between the region in space where the field is < 1 nT (outside the surface) and the region where the field is > 1 nT. The isosurface is coloured red from the inside and blue from the outside.

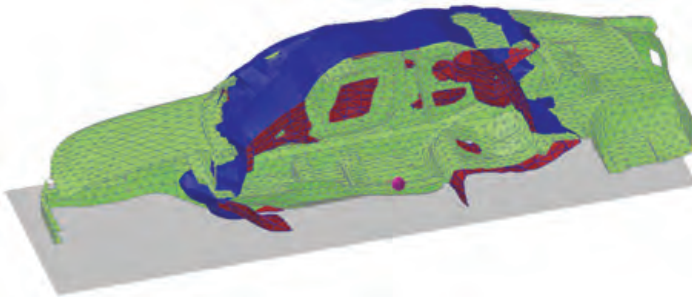


Fig. 100. Isosurface at a 1 nT B-field for an internal antenna

The results of this analysis demonstrate that it is possible to optimise the antennas of a smart-entry system by using simulations.

3.7 Investigation of Inductive Charging System

One technology that can address the issue of charging in electric vehicles (EV) and hybrid vehicles (HV) is wireless power transmission, also known as inductive charging. This system consists of an underground primary coil, which is connected to a contactless charging station. The electric current passing through the primary coil creates an EM field, which generates a current in the secondary coil (typically 8 – 15 cm from the primary coil) to charge the battery of the EV or HV. The EM fields generated by this system must meet certain international standards. This section investigates the magnetic fields radiated by an inductive charging system in the presence of a car. The radiating coil can consist of many loops and a ferrite structure in order to concentrate the fields. For this analysis, the configuration shown in Fig. 101. was used, which consists of a ten-loop coil inside a ferrite structure. Using a frequency sweep around the operating frequency of 150 kHz, a capacitance was found that produced resonance at the operating frequency. The input power of the transmitting antenna was 3 kW. Fig. 102. shows the distribution of the magnetic near-field generated by the transmitting coil under the centre of a car.

In this setup, the stray field outside the car body was higher than that inside the car body. A more precise representation of the field distribution can be obtained by considering more details of the car body and accounting for the properties of the surrounding space (i.e., possible metallic structures on the ground). Note how these fields interact with the electronic systems in the car, especially if they are located under the car body (e.g., sensors of the power train).

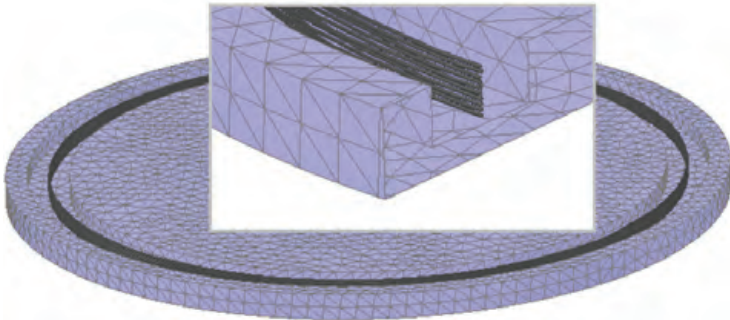


Fig. 101. Model details of the transmitting coil of an inductive charging system

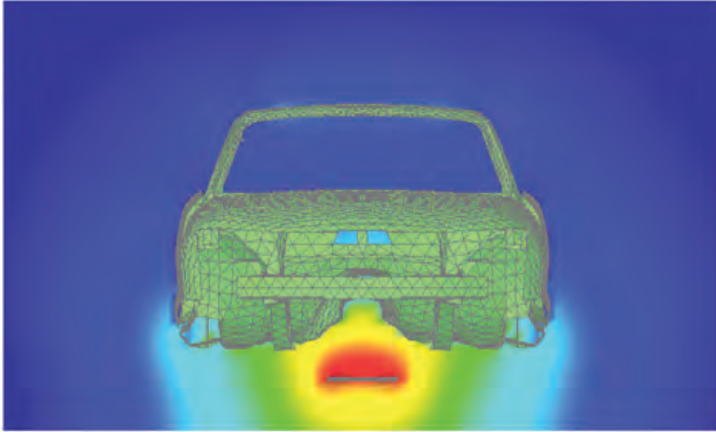


Fig. 102. Near-field distribution of the B-field (frequency = 150 kHz, power = 3 kW)

3.8 Conclusions

MoM was used to numerically solve problems with low-frequency magnetic fields interacting with 3D voluminous objects and/or objects made of thin sheets with combined magnetic and resistive properties. The presence of wires and their connection to conducting surfaces was considered in the analysis. Different approximate BCs were also considered along with a quasi-static field approximation. The low-frequency behaviour of the equivalent surface currents was accounted for by decomposing the currents into solenoidal and non-solenoidal parts, which allowed more rapid calculation of the magnetic fields than by using a full-wave method. The numerical simulations agreed with semi-analytical approaches for a thin plate and a spherical shell, as well as with experimental measurements.

CHAPTER 4

FULL-WAVE MOM SIMULATIONS OF EM INTERACTIONS IN EMC FILTERS FOR POWER APPLICATION

4.1 Introduction

This chapter introduces a simulation methodology for accurate prediction of the coupling between components of electromagnetic interference (EMI) filters for power electronics applications [127]. Full-wave MoM is applied. The developed models take into account the parasitic elements of the components as well as 3D EM coupling between them. This procedure is advantageous compared to FEM since only surface discretisation is needed. Modelling of wires is also better suited in MoM than in FEM. Compared to a partial element equivalent circuit (PEEC) solution [128]-[130], MoM gives more accurate results for high frequencies.

The first part of this chapter will describe a procedure to model voluminous components, such as common-mode (CM) chokes, differential-mode (DM) inductances and film capacitors. The accuracy of the models is verified by comparison with measurements. The second part of the chapter focuses on modelling an EMI filter taking into account interactions between voluminous components. First, the CM and DM transfer functions of the filter are considered. Near-field magnetic emissions are then considered. Simulation results are in good agreement with measurements in the frequency range 10 kHz to 50 MHz. Once power electronics engineers have designed a filter, the present work will help to optimise the layout of the components in order to improve the high-frequency behaviour of the filter (typically above 1 MHz) and to pass the RF emission tests on the first try, especially when space availability is very limited.

4.2 Validation of 3D MoM Models for Filter Components

Three important passive components of EMC filters must be considered in 3D modelling: voluminous film capacitors, CM chokes and DM inductors. In order to predict the RF behaviour of EMI capacitors, it is necessary to construct a 3D model based on the dimensions of the metalised film roll and its connectors [131]. The measurement setup with two 2.2 μF capacitors and their 3D models is shown in Fig. 103.

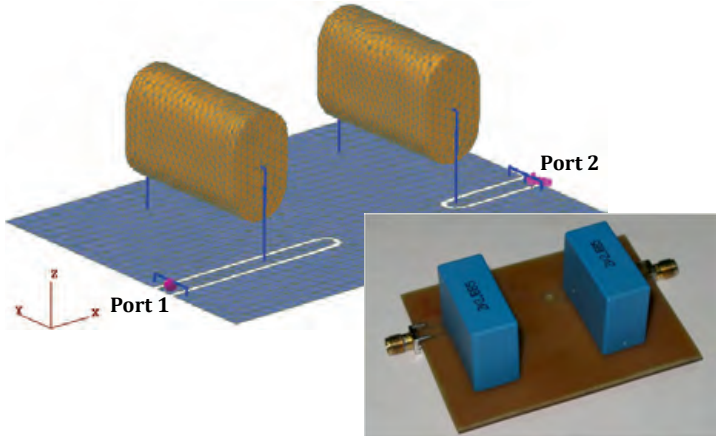


Fig. 103. Modelling of film capacitor

The geometry of the metalised film rolls of EMC capacitors can be obtained by visual examination of split samples. A metalised film roll can be described by its width, length and height; the dimensions of the model elements are listed in Table 7.

Table 7. Model element dimensions

Parameter	Value
Metalised film roll: x-width	12.0 mm
Metalised film roll: y-length	25.5 mm
Metalised film roll: z-height	20.0 mm
Gap size:	6.5 mm
Distance between centres of film rolls:	40.0 mm

Positioning on the printed circuit board (PCB) is defined by the distance between the centres of the rolls.

Film rolls are modelled by the outer surface and a $2.2 \mu\text{F}$ nominal capacitance in series with a $17 \text{ m}\Omega$ resistance inserted as lumped elements. The computational MoM model contains 4,276 triangular and 76 wire elements.

Fig. 104. represents the frequency dependence of the transmission coefficient between the ports. For frequencies below 10 kHz, the standard MoM formulation might exhibit instabilities; these instabilities are caused by well-known low-frequency break-downs [132]. In the frequency range from several tens of kHz up to 1 GHz, simulation and measurement data coincide with an accuracy of approximately 2 dB.

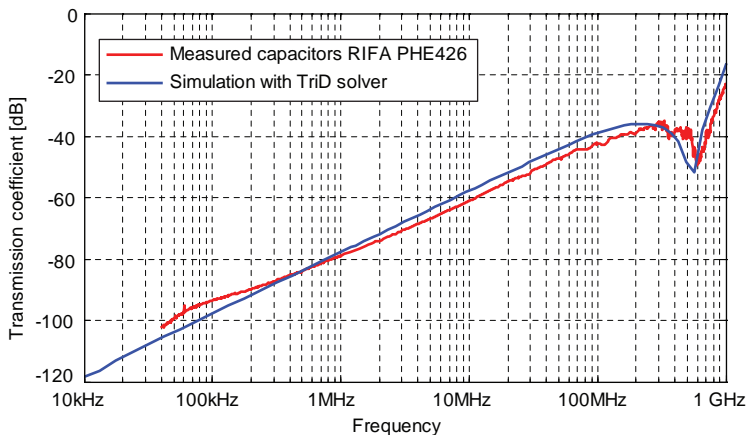


Fig. 104. Transmission coefficient

In order to design models of inductive elements, such as CM or DM chokes, it is necessary to define the core geometry and coil winding. Moreover, the complex and frequency-dependent permeability and permittivity of the ferrite material are critical input parameters for the construction of the core models. This information can be obtained either from manufacturers for specific cores or by applying special methods for retrieving dimension-independent material parameters [132].

The input impedance of the inductor, shown in Fig. 105., was simulated and measured in the frequency range 100 Hz to 100 MHz using a Wayne Kerr 65120B impedance analyser in order to validate the inductive element model. The winding is constructed from fifteen turns of copper wire coiled around a toroidal core made of N30 material (EPCOS AG, Part No. B64290L0082X830). The dimensions of the toroidal core are given in Table 8.

Table 8. Toroidal core dimensions

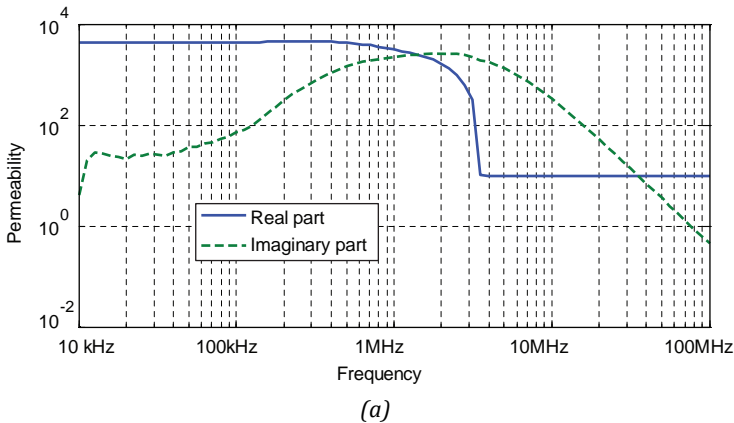
Outer diameter	Inner diameter	Height
50 mm	30 mm	20 mm

The toroidal core is modelled by MoM using a surface-integral approach [1] and it is represented by a bulk dielectric object that is described by its outer surface (the discretised mesh contains approximately 1,600 triangular elements). The winding is represented by 623 wire segments. This approach makes it possible to consider directly the influence of the frequency-dependent complex material parameters of the ferrite material on the inductance of the coil, as well as the influence of the capacitance between the windings and the capacitance of the windings to the core.



Fig. 105. Measured sample and model of coil

The frequency dependence of the electrical and magnetic properties of EPCOS N30 MnZn-based ferrite material are shown in Fig. 106.



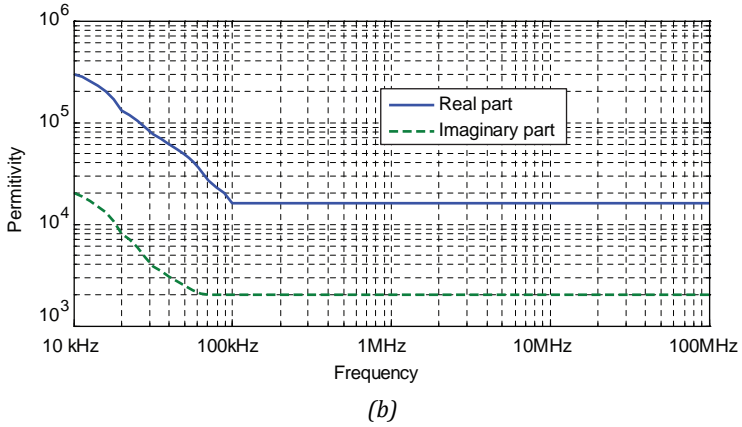


Fig. 106. Frequency dependence of the complex permeability and permittivity of EPCOS N30 ferrite material

The simulated real and imaginary parts of the coil impedance are compared with the measured values in Fig. 107., where it can be seen that they are in good agreement. This demonstrates the accurate determination of the inductance and winding capacitance of the coil element in the frequency range 10 kHz to 100 MHz.

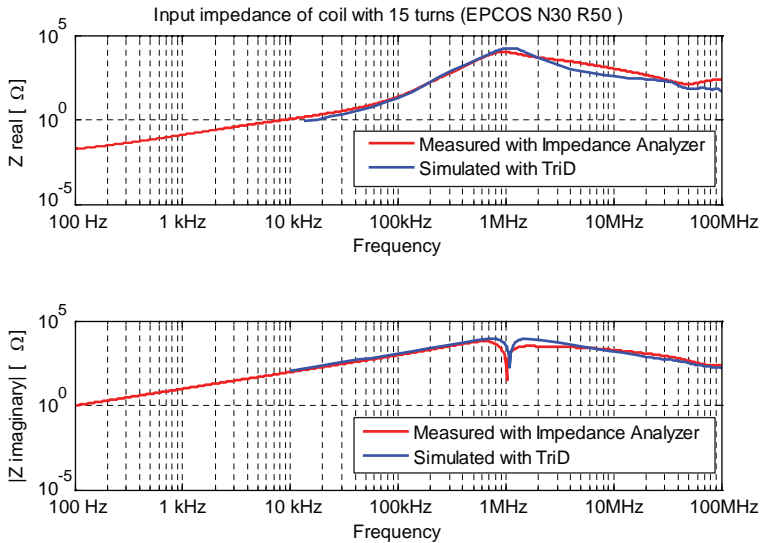


Fig. 107. Coil impedance

4.3 Modelling of the 3D Layout Influence on Filter Performance

For the investigation of the RF behaviour of the voluminous components and the influence of their layout on filter performance, a typical filtering circuit for a single-phase application is considered (Fig. 108.).

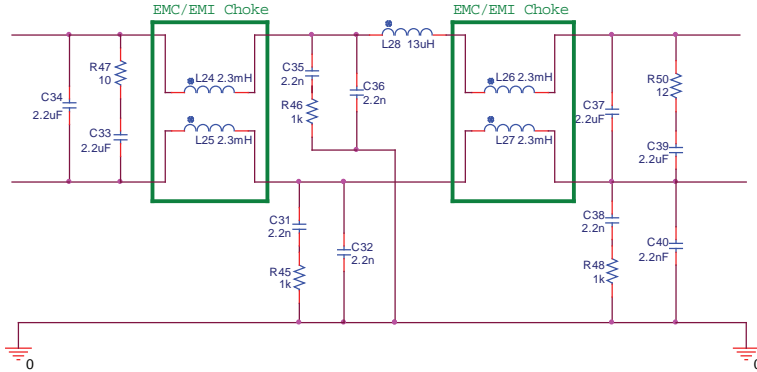


Fig. 108. Schematic of the filter under study

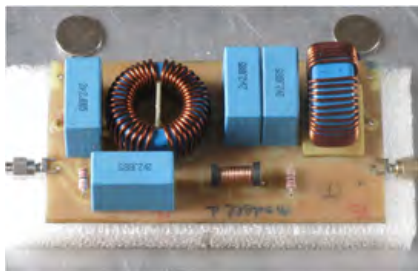
Two variants of the filter with different component placements are shown in Fig. 109. (a) and (b), and their 3D models are shown in Fig. 110. (c) and (d).

The following voluminous components were used in filter construction and were represented by 3D models: (i) four 2.2 μF film X-capacitors (discussed in Section 4.2; (ii) two CM chokes, realised as two coils (each has 2.3 mH inductance with a tolerance of 0.1 mH) on an EPCOS toroid core (modelled in Section 4.2) and (iii) one 13 μH DM inductor coiled on a bobbin-type core having 19 mm length and made of an MnZn-based ferrite material (Fair-Rite Products Corp., Part No. 9677001015).

Other elements of the filter structure, such as 2.2 nF Y-capacitors and resistors, were relatively small surface-mount technology (SMD) components and they were modelled as lumped elements applied to wire segments.

All elements were arranged on a 13 cm x 7 cm PCB, which was as compact as possible while still providing sufficient space to change the position and orientation of the voluminous components without needing to increase the dimensions of the PCB.

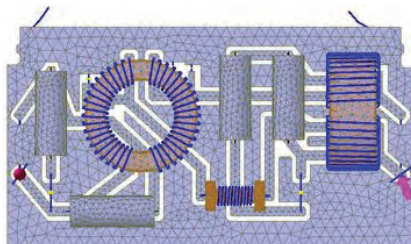
It should be noted that the filters were tested under low-current conditions, so that the temperature dependence and saturation effects of the ferrite materials did not affect their performance and did not need to be taken into account in the simulation models.



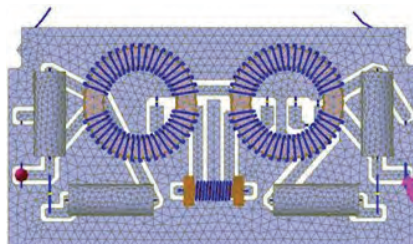
(a) Filter Model 1



(b) Filter Model 2



(c) Simulation of Model 1



(d) Simulation of Model 2

Fig. 109. Filter layouts and corresponding 3D models

The transfer function between the load and mains connectors was measured for both filter samples using a Hewlett-Packard HP8546A EMI test receiver in the frequency range 10 kHz to 50 MHz, in both CM and DM. In order to measure the CM transfer functions, both lines were connected in parallel with respect to the ground. For measurements of the DM transfer function, active balun circuits were designed and used at the input and output connectors of the filters (Fig. 110.).

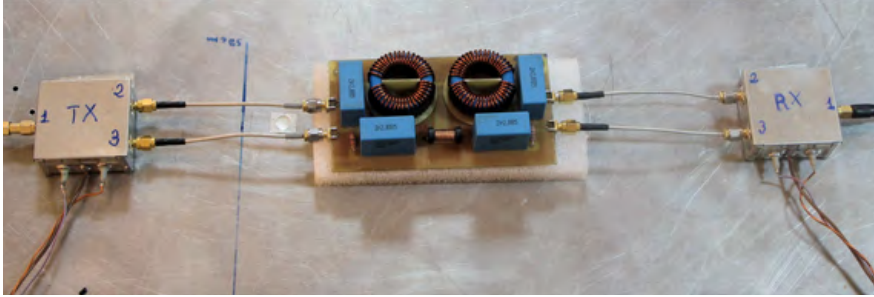


Fig. 110. Measurement of the DM transfer function

The balun circuits provide an accurate symmetrical split of the signal from the generator and a symmetrical addition of the signals at the output lines of the filter. The corresponding simulation model is shown in Fig. 111.

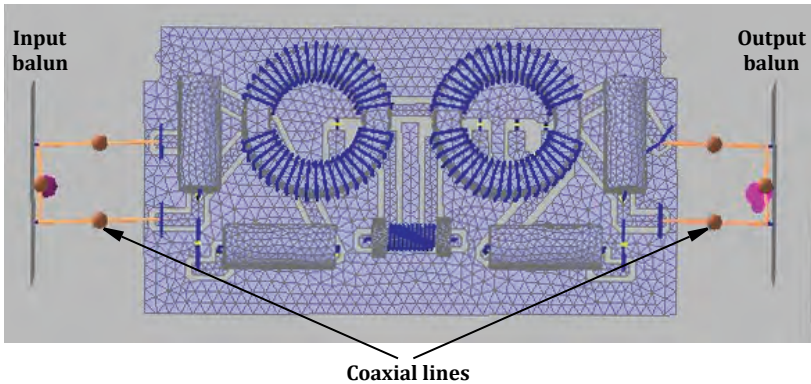


Fig. 111. Simulation model with baluns and coaxial lines

Baluns were incorporated into the MoM model as 3-port network elements described by the measured S-parameter matrices [33]. Coaxial lines were modelled in the MoM model as non-radiating transmission-line elements.

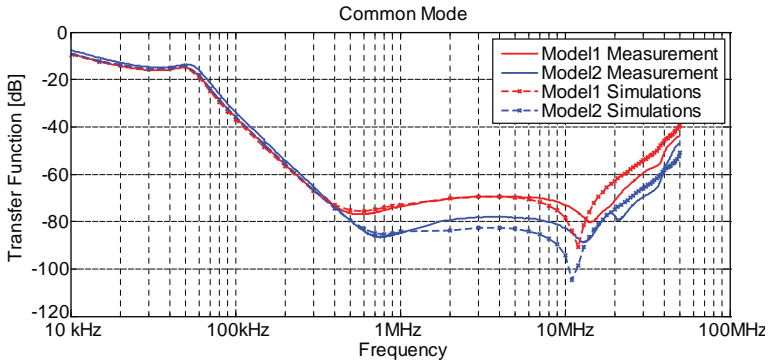


Fig. 112. Simulated and measured CM transfer functions

Fig. 112. compares the CM transfer functions for the two filter models described above. For frequencies below 400 kHz, the performance of the filter is not affected by 3D coupling effects and it is independent of component placement. Coupling effects play an important role above 400 kHz, where there is an approximate 10 dB difference in filter attenuation.

Discrepancies between the simulated and measured CM performance of the filter, such as displacement and difference in depth of resonances around 10 MHz, are caused by uncertainties in the dimensions and placement of the 3D components.

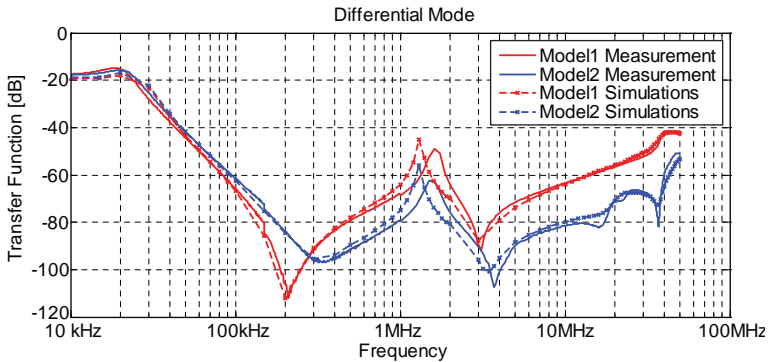


Fig. 113. Simulated and measured DM transfer functions

Measured and simulated DM transfer functions are compared for both filter models. It can be seen that the RF coupling between components affects the filter characteristics at frequencies greater than 100 kHz; this is especially important at frequencies greater than 3 MHz, and it changes DM filter performance by 20 dB.

The simulations demonstrate the accurate prediction of the measured performance of the filters. The displacement between the measured and simulated resonances around 1.5 MHz for DM is due to tolerances of ferrite core materials and uncertainties in wire coil construction. Parasitic capacitance is very sensitive to distance between wire turns, especially for tight windings. Furthermore, uncertainties in the determination of the distance to core and total wire length both affect the accuracy of the simulated results.

4.4 Modelling of Radiated EM Fields

Observation of the radiated EM field distribution around the filter components can provide important information about the coupling between the components as well as help in the optimisation of the filter layout or of its placement relative to nearby electronic devices. This section will describe the measurement and simulation of the B-field distribution in the horizontal observation plane, located above the filter components (50 mm from the ground level), for both filter models (Fig. 114.).

The B-field distribution was measured with a 5 mm spatial resolution using a small loop probe. CM connection of the filter was considered.

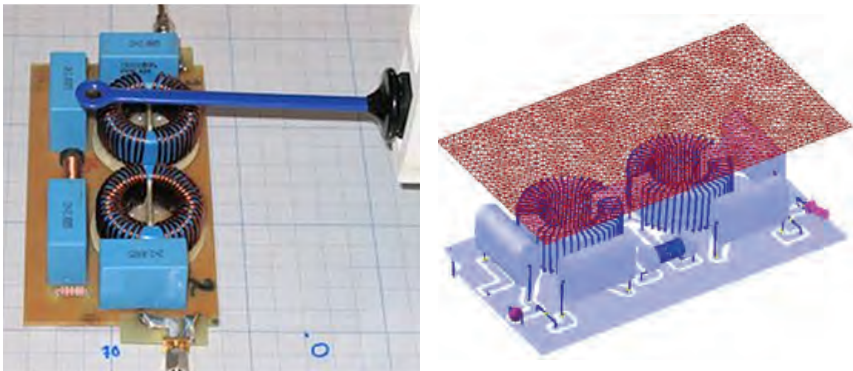


Fig. 114. Observation of B-field distribution (example of filter Model 2)

The measured and simulated distribution of the normalised vertical component of the B-field at 1 MHz for a filter model with horizontal positioning of CM chokes (filter model 2) is shown in Fig. 115. Fig. 116. shows the simulated vertical component of the B-field corresponding to a 1 V feeding source.

The qualitative analysis of these results shows that the simulated field structure describes the measured field distribution accurately.

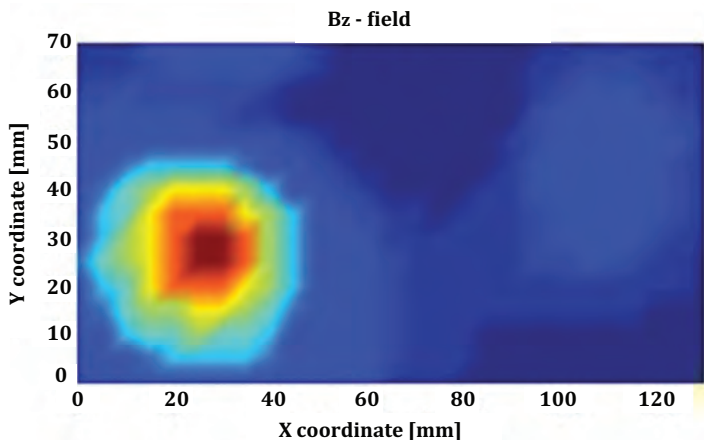


Fig. 115. Measured vertical component of the B-field at 1 MHz for filter Model 2

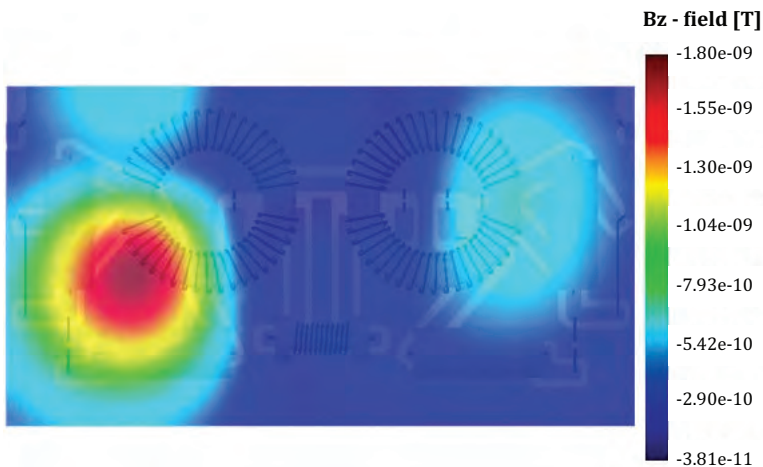


Fig. 116. Simulated vertical component of the B-field at 1 MHz for filter Model 2

Fig. 117. shows the distribution of the vertical component of the B-field simulated at 1 MHz for filter Model 1 with a vertical CM choke in the output cascade, and assuming a 1 V feeding source.

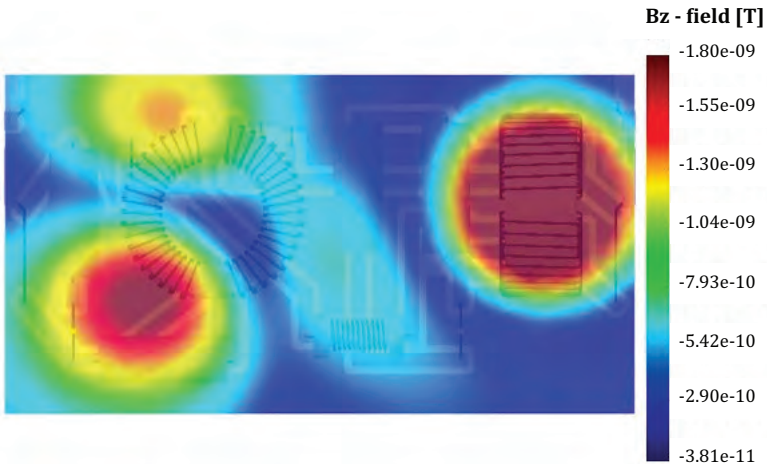


Fig. 117. Simulated vertical component of the B-field at 1 MHz for filter Model 1

Comparing the component layouts for both filter models, it can be seen that the wire winding of the vertical CM choke of Model 1 is located closer to the considered observation plane than the horizontally placed coil of Model 2. This results in a larger observed B-field magnitude compared to the output cascade of filter Model 2.

The presented results show that it is possible to predict the near-field magnetic radiation of a complex EMI filter layout. These 3D full-wave simulations may also present a useful and flexible method for further visual analysis of the volume distribution of EM fields and coupling paths that can be used to develop easy-to-use design rules for the optimisation of filter structure and layout of components.

4.5 Conclusions

In this chapter, MoM was applied for the prediction of 3D EM interactions that affect the performance of EMC filters for power applications. Simulations were performed for EMC power filters in the frequency range 10 kHz to 50 MHz; the simulations were in good agreement with the measurements regarding CM and DM transfer functions. Near-field magnetic radiation was also studied and simulations showed good qualitative agreement with measurements.

This work should help to optimise EMI filter layout and placement in order to improve high-frequency EMC behaviour once power electronics engineers have designed the circuit from its low-frequency functional specifications.

Conclusions

This thesis presented the development of efficient techniques for simulation of EMC problems in automotive vehicles, specifically:

- A novel hybrid MoM scheme for modelling automotive glass antennas was developed. This scheme was validated by comparison of the measured and simulated EMC characteristics of a full vehicle model with rear-window glass antenna. Multiport networks were also considered; this allowed modelling of complex linear electronic systems (such as linear amplifiers) together with antennas [36] - [37].
- A novel methodology for the design and optimisation of automotive glass antennas was developed. This methodology was applied successfully in a selection of automotive OEMs [36] - [37].
- A new hybrid MTL/MoM technique was developed for the simulation of crosstalk, signal integrity, radiation and susceptibility problems in complex cable-harness systems, embedded into a 3D environment [74].
- A simulation approach and new model-generation technique were developed for HV cables used in power electronics and in electrical vehicles [84].
- A computationally efficient method was developed for solving low-frequency EMC problems by using integral equations. The proposed numerical solution is unique in its representation of equivalent currents as the sum of solenoidal and non-solenoidal components, found using MoM in two steps: first, the solenoidal currents are determined using loop basis functions, and then the non-solenoidal currents are found. The method was applied to industrial problems [90].
- A comprehensive simulation methodology for accurate prediction of the coupling between components of EMI filters for power electronics applications was developed. The developed models take into account the parasitic elements of the components as well as the 3D EM coupling between them. Simulations are performed for EMC power filters in the frequency range 10 kHz to 50 MHz and the results are in a good agreement with measurements. The developed methodology accelerates significantly the design of EMC filters used in power applications [127].

Results of investigations have been published in eighteen papers and most of the methods have been implemented in commercial software packages.

Reference

- [1] EMC Studio, Users Manual, EMCoS Ltd. Available at: www.emcos.com.
- [2] R. Jobava, S. Frei, F. Bogdanov, A. Gheonjian, R. Kvaratskhelia and Z. Sukhiashvili, "Pre-processing of 3D CAD data for electromagnetic simulations by the method of moments," in *Proc. 6th Int. Seminar/Workshop Direct and Inverse Problems of Electromagnetic and Acoustic Wave Theory, 2001. DIPED 2001*, Lviv, Georgia, 2001, pp. 191-194.
- [3] ReMesh, Users Manual, EMCoS Ltd. Available at: www.emcos.com.
- [4] F. Haslinger, B. Unger, M. Maurer, M. Troscher and R. Weigel, "EMC modeling of nonlinear components for automotive applications," in *Proc. 14th Int. Zurich Symp. on EMC*, Zurich, Switzerland, 2001.
- [5] I. Chahine, X. Bunlon, F. Lafon, F. De Daran and P. Matossian, "An original approach based on data exchange between car manufacturers and suppliers to estimate susceptibility threshold by numerical simulation at early design stage," *IEEE Trans. Electromagn. Compat.*, vol. 55, no. 2, pp. 342-352, Apr. 2013.
- [6] I. Oganezova, X. Bunlon, A. Gheonjian, I. Chahine, B. Khvitia and R. Jobava, "A new and easy approach to create BCI models," in *2014 IEEE Int. Symp. Electromagnetic Compatibility (EMC)*, Raleigh, NC, 2014, pp. 91-96.
- [7] A. Gheonjian, X. Bunlon, I. Oganezova, I. Chahine, B. Khvitia and R. Jobava, "Modeling of BCI test setup applied to common rail pressure control system," in *2014 IEEE Int. Symp. Electromagnetic Compatibility (EMC)*, Gothenburg, Sweden, 2014, pp. 196-201.
- [8] Harness Studio, Users Manual, EMCoS Ltd. Available at: www.emcos.com.
- [9] V. Rabinovich, N. Alexandrov and B. Alkhateeb, *Automotive Antenna Design and Applications*. Boca Raton, FL: CRC Press/Taylor & Francis, 2010.
- [10] T. H. Hubing, "Survey of numerical electromagnetic modeling techniques," Dept. Elect. Eng., Univ. Missouri, Rolla, Tech. Rep. TR91-1-001.3, Sept. 1, 1991.
- [11] R. F. Harrington, *Field Computation by Moment Methods*. New York, NY: Macmillan, 1968.
- [12] F. Bogdanov, R. Jobava and S. Frei, "Estimating accuracy of MoM solutions on arbitrary triangulated 3-D geometries based on examination of boundary conditions performance and accurate derivation of scattered fields," *J. Electromagnet. Wave.*, vol. 18, no. 7, pp. 879-897, 2004.

-
- [13] D. R. Lynch and K. D. Paulsen, "Origin of vector parasites in numerical Maxwell solutions," *IEEE Trans. Microw. Theory Tech.*, vol. 39, no. 3, pp. 383-394, Mar. 1991.
- [14] K. D. Paulsen and D. R. Lynch, "Elimination of vector parasites in finite element Maxwell solutions," *IEEE Trans. Microw. Theory Tech.*, vol. 39, no. 3, pp. 395-404, Mar. 1991.
- [15] A. Taflove, *Computational Electrodynamics: The Finite-Difference Time-Domain Method*. Boston, MA: Artech House, 1995.
- [16] R. Holland, V. P. Cable and L. C. Wilson, "Finite-volume time-domain (FVTD) technique for EM scattering," *IEEE Trans. Electromagn. Compat.*, vol. 33, no. 4, pp. 281-294, Nov. 1991.
- [17] N. Koch, "Antennas for automobiles," in *New Advances in Vehicular Technology and Automotive Engineering*, J. P. Carmo and J. E. Ribeiro, Eds. Rijeka, Croatia: InTech, 2012, pp. 410, DOI: 10.5772/2617. Available at: <http://www.intechopen.com/books/new-advances-in-vehicular-technology-and-automotive-engineering>
- [18] B. D. Pell, E. Sulic, W. S. T. Rowe, K. Ghorbani and S. John, "Advancements in automotive antennas," in *New Trends and Developments in Automotive System Engineering*, M. Chiaberge, Ed. Rijeka, Croatia: InTech, 2011, DOI: 10.5772/13368. Available at: <http://www.intechopen.com/books/new-trends-and-developments-in-automotive-system-engineering/advancements-in-automotive-antennas>
- [19] H. L. Blöcher, G. Rollmann and S. Gärtner, "Trends in automotive RF wireless applications and their electromagnetic spectrum requirements," in *2005 German Microwave Conf. (GeMiC)*, Ulm, Germany, 2005, pp. 148-151.
- [20] E. K. Walton, Y. Horiki and M. Rosin, "Layout for automotive window antenna", U.S. Patent 6 693 597, February 17, 2004.
- [21] N. F. Bally K. Yegin, R. J. Snoeyink and W. R. Livengood, "AM/FM dual grid antenna," U.S. Patent 7 038 630, May 2, 2006.
- [22] Y. Nagayama and M. Maegawa, "Glass antenna for side windshield of automotive vehicle," U.S. Patent 6 384 790, May 7, 2002.
- [23] H. K. Lindenmeier, Ed., *Mobile Antenna Systems Handbook*. Boston, MA: Artech House, 1994, pp. 293.
- [24] R. Abou-Jaoude and E. K. Walton, "Numerical modeling of on-glass conformal automobile antennas," *IEEE Trans. Antennas Propag.*, vol. 46, no. 6, pp. 845-852, Jun. 1998.
- [25] Y. Kim and E. K. Walton, "Effect of body gaps on conformal automotive antennas," *Electron. Lett.*, vol. 40, pp. 1161-1162, 2004.
-

- [26] L. Low and R. Langley, "Modeling automotive antennas," *IEEE Int. Symp. Antenna Propagation Dig.*, vol. 3, pp. 3171-3174, Jun. 2004.
- [27] R. Langley and J. Batchelor, "Hidden antenna for vehicles," *Electron. Commun. Eng.*, vol. 14, pp. 253-262, 2002.
- [28] J. Batchelor, R. Langley and H. Endo, "On-glass mobile antenna modeling," *IEE Proc. Microw., Antennas Propag.*, vol. 148, no. 4, pp. 233-238, Aug. 2001.
- [29] J. C. Batchelor, R. J. Langley, H. Endo and M. Saito, "Modeling of vehicles with integrated antennas," *MOTL*, vol. 27, Issue 6, pp. 404-407, 2000.
- [30] F. G. Bogdanov and R. G. Jobava, "Examination of boundary conditions performance for estimating accuracy of MoM solutions on square plate benchmark geometry using triangle doublet basis functions," *Microw. Opt. Techn. Let.*, vol. 39, no. 3, pp. 193-196, Nov. 2003.
- [31] F. G. Bogdanov, R. G. Jobava and S. Frei, "Scheme of improving accuracy of MoM solutions based on analysing boundary conditions performance," in *Proc. East-West Workshop Advanced Techniques in Electromagnetics, ATE-2004*, Warszawa, Poland, pp. 217-224, May 2004.
- [32] F. G. Bogdanov, R. G. Jobava and S. Frei, "Estimating accuracy of MoM solutions on arbitrary triangulated 3-D geometries based on examination of boundary conditions performance and accurate derivation of scattered fields," *J. Electromagnet. Wave.*, vol. 18, no. 7, pp. 879-897, 2004.
- [33] R. Jobava, F. G. Bogdanov, A. Gheonjian and S. Frei, "Application of adaptive scheme for the method of moments in EMC automotive problems," in *Proc. 16th Int. Zurich Symp. on EMC*, Zurich, Switzerland, pp. 131-136, Feb. 2005.
- [34] F. G. Bogdanov, R. G. Jobava, A. L. Gheonjian, E. A. Yavolovskaya, N. G. Bondarenko, and T. N. Injgia, "Development and application of an enhanced MoM scheme with integrated generalized N-port networks," *Prog. Electromagn. Res. M*, vol. 7, pp. 135-148, 2009.
- [35] F. G. Bogdanov, D. D. Karkashadze, R. G. Jobava, A. L. Gheonjian, E. A. Yavolovskaya and N. G. Bondarenko, "Advantage of a hybrid MoM scheme with approximate Green function to model integrated glass antennas," *Microw. Opt. Techn. Let.*, vol. 52, no. 2, pp. 351-354, Feb. 2010.
- [36] F. G. Bogdanov, D. D. Karkashadze, R. G. Jobava, A. L. Gheonjian, E. A. Yavolovskaya, N. G. Bondarenko and C. Ullrich, "Validation of hybrid MoM scheme with included equivalent glass antenna model for handling automotive EMC problems," *IEEE Trans. Electromagn. Compat.*, vol. 52, no. 1, pp. 164-172, Feb. 2010.

-
- [37] F. Bogdanov, R. Jobava, D. Karkashadze, P. Tsereteli, A. Gheonjian, E. Yavolovskaya, D. Schleicher, C. Ullrich and H. Tazi, "Computational techniques for automotive antenna simulations," in *New Trends and Developments in Automotive System Engineering*, M. Chiaberge, Ed. Rijeka, Croatia: InTech, 2012, pp. 585-610.
- [38] R. F. Harrington and J. R. Mautz, "An impedance sheet approximation for thin dielectric shells," *IEEE Trans. Antennas Propag.*, vol. 23, no. 4, pp. 531-534, Jul. 1975.
- [39] B. D. Popović, *CAD of Wire Antennas and Related Radiating Structures*. New York, NY: Research Studies Press - John Wiley & Sons, 1991.
- [40] R. Abou-Jaoude and E. K. Walton, "Numerical modelling of on-glass conformal automobile antennas," *IEEE Trans. Antennas Propag.*, vol. 46, no. 6, pp. 845-852, Jun. 1998.
- [41] L. Low, R. Langley and J. Batchelor, "Modelling and performance of conformal automotive antennas," *IET Microw. Antennas Propag.*, vol. 1, no. 5, pp. 973-979, Oct. 2007.
- [42] A. R. Ruddle, H. Zhang, L. Low, J. Rigelsford and R. J. Langley, "Numerical investigation of the impact of dielectric components on electromagnetic field distributions in the passenger compartment of a vehicle," in *Proc. 20th Int. Zurich Symp. on EMC*, Zurich, Switzerland, 2009, pp. 213-216.
- [43] R. F. Harrington and J. R. Mautz, "An impedance sheet approximation for thin dielectric shells," *IEEE Trans. Antennas Propag.*, vol. 23, no. 4, pp. 531-534, Jul. 1975.
- [44] E. H. Newman, "A user's manual for electromagnetic surface patch code: version V (ESP5)," The Ohio State University Electroscience Laboratory, Columbus, OH, Oct. 1998.
- [45] Computer Simulation Technology. Available at: <http://www.cst.com>.
- [46] TriD, User's Manual, EMCoS Ltd., Available at: www.emcos.com
- [47] C. H. Stoyer, "Electromagnetic fields of dipoles in stratified media," *IEEE Trans. Antennas Propag.*, vol. 25, no. 4, pp. 547-552, Jul. 1977.
- [48] Y. L. Chow, J. J. Yang, D. F. Fang and G. E. Howard, "Closed form spatial Green's function for the thick substrate," *IEEE Trans. Microw. Theory Tech.*, vol. 39, pp. 588-592, Mar. 1991.
- [49] G. Dural and M. I. Aksun, "Closed-form Green's function for general sources and stratified media," *IEEE Trans. Microw. Theory Tech.*, vol. 43, pp. 1545-1552, Jul 1995.
-

- [50] M. I. Aksun and G. Dural, "Clarification of issues on the closed-form Green's functions in stratified media," *IEEE Trans. Antennas Propag.*, vol. 53, no. 11, pp. 3644-3653, Nov 2005.
- [51] A. Sommerfeld, *Partial Differential Equations in Physics*. New York, NY: Academic Press, 1949.
- [52] R. Mittra, P. Parhami and Y. Rahmat-Samii, "Solving the current element problem over lossy half-space without Sommerfeld's integrals," *IEEE Trans. Antennas Propag.*, vol. 27. pp. 778-782, Nov. 1979.
- [53] W. C. Kuo and K. K. Mei, "Numerical approximations of the Sommerfeld integral for fast convergence," *Radio Sci.*, vol. 13. no. 3, pp. 407-415, 1979.
- [54] S. Singh and R. Singh, "Computation of Sommerfeld integrals using tanh transformation," *Microw. Opt. Techn. Let.*, vol. 37, no.3, pp. 177-180, 2003.
- [55] J. R. Wait, "Image theory of a quasi-static magnetic dipole over a dissipative half-space," *Electron. Lett.*, vol. 5, pp. 281-282, 1969.
- [56] S. F. Mahmoud and A. D. Metwally, "New image representations for dipoles near a dissipative earth. I. Discrete images," *Radio Sci.*, vol. 16, no. 6. pp. 1271-1275, 1981.
- [57] P. R. Bannister, "Applications of complex image theory," *Radio Sci.*, vol. 21, no. 4, pp. 605-616, 1986.
- [58] J. R. Wait, "Complex image theory - revisited," *IEEE Antennas Propagat. Mag.*, vol. 33, no. 4, pp. 27-29, 1991.
- [59] E. K. Miller, A. J. Poggio, G. J. Burke and E. S. Selden, "Analysis of wire antennas in the presence of a conducting half-space: Part I. The vertical antenna in free space; Part II: The horizontal antenna in free space," *Can. J. Phys.*, vol. 50, pp. 879-888, 2614-2627, 1972.
- [60] R. G. Olsen and M. C. Willis, "A comparison of exact and quasi-static methods for evaluating grounding systems at high frequencies," *IEEE Trans. Power Del.*, vol. 11, no. 2, pp. 1071 - 1081, Apr. 1996.
- [61] D. Poljak and V. Doric, "Wire antenna model for transient analysis of simple grounding systems, Part I: the vertical grounding electrode," *Prog. Electromagn. Res.*, vol. 64, pp. 149-166, 2006. "Part II: the horizontal grounding electrode," *ibid*, pp. 167-189.
- [62] G. Ala and M. L. Di Silvestre, "A simulation model for electromagnetic transients in lightning protection systems," *IEEE Trans. Electromagn. Compat.*, vol. 44, no. 4, pp. 539-554, Nov. 2002.
- [63] P. Jacqmaer, C. Geuzaine and J. Driesen, "Modelling earthing systems and cables with Moment Methods," in *Proc. 13th Int. IGTE Symp. Num. Field Calc. Elect. Eng.*, Graz, Austria, 2008.

-
- [64] E. Yamashita and S. Yamazaki, "Parallel-strip line embedded in or printed on a dielectric sheet," *IEEE Trans. Microw Theory Tech.*, vol. 16, pp. 972-973, Nov. 1968.
- [65] M. Leone, H. Brüns and H. Singer, "Fast EMC analysis for printed circuit boards using an equivalent wire method of moments," in *Proc. Int. Symp. on EMC'98*, Rome, Italy, 1998, pp. 7-12.
- [66] M. Leone, H.-D. Brüns and H. Singer, "Effiziente simulation der abstrahlung von leiterplatten auf geräteebene," *EMV2000 8. Intern. Fachmesse u. Kongreß*, Düsseldorf, 2000, S. 429-436.
- [67] U. Jakobus, N. Berger and F. M. Landstorfer, "Efficient techniques for modelling integrated windscreen antennas within the method of moments," *Millennium Conf. Antenna Propag. AP-2000*, Davos, Switzerland, 2000.
- [68] F. G. Bogdanov, D. D. Karkashadze and R. G. Jobava, "Efficient MoM-based technique for fast analysis of layered microstrip geometries using equivalent glass antenna model," in *Proc. 13th Int. Seminar/Workshop on Direct and Inverse Problems of Electromagnetic and Acoustic Wave Theory, 2008. DIPED 2008*, Tbilisi, Georgia, 2008, pp. 114-118.
- [69] F. G. Bogdanov, D. D. Karkashadze, R. G. Jobava, E. Yavolovskaya and N. Bondarenko, "Hybrid MoM scheme with integrated finite sized equivalent glass antenna model in application to automotive EMC problems," in *Proc. 13th Int. Seminar/Workshop on Direct and Inverse Problems of Electromagnetic and Acoustic Wave Theory, 2008. DIPED 2008*, Tbilisi, Georgia, 2008, pp. 82-86.
- [70] F. Bogdanov, D. Karkashadze, R. Jobava, A. Gheonjian, E. Yavolovskaya, and N. Bondarenko, "Hybrid MoM scheme with incorporation of equivalent glass antenna model in application to automotive EMC problems," in *Proc. 20th Int. Zurich Symp. on EMC*, Zurich, Switzerland, pp. 217-220, Jan. 2009.
- [71] A. Erteza and B. Park, "Nonuniqueness of resolution of Hertz vector in presence of a boundary, and a horizontal dipole problem," *IEEE Trans. Antennas Propag.*, vol. 17, no. 3, pp. 376-378, May 1969.
- [72] K. A. Michalski, "On the scalar potential of a point charge associated with a time-harmonic dipole in a layered medium," *IEEE Trans. Antennas Propag.*, vol. 35, no. 11, pp. 1299-1301, Nov. 1987.
- [73] C. R. Paul, *Analysis of Multiconductor Transmission Lines*. New York: John Wiley & Sons, 1994.

- [74] H. Chobanyan, I. Badzagua, T. Injgia, A. Gheonjian and R. Jobava, "Application of hybrid MoM/MTL method to simulation of interaction between cable harness and antennas", in *Proc. 14th Int. Seminar/Workshop Direct and Inverse Problems of Electromagnetic and Acoustic Wave Theory, 2009*. DIPED 2009, Lviv, Ukraine, pp. 33-38.
- [75] D. Karkashadze, R. Jobava, S. Frei and B. Soziashvili, "A fast method of auxiliary source based calculation of capacitance and inductance matrices," in *Proc. 6th Int. Seminar/Workshop Direct and Inverse Problems of Electromagnetic and Acoustic Wave Theory, 2001*. DIPED 2001, Lviv, Ukraine, pp. 187-190.
- [76] K. L. Kaiser, *Electromagnetic Compatibility Handbook*. Boca Raton, FL: CRC Press, 2005, ch. 5.
- [77] S. A. Schelkunoff, "Theory of lines and shields", *Bell Syst. Tech. J.*, v. 13, no. 4, pp. 532-579, 1934.
- [78] F. M. Tesche, M. V. Ianoz, and T. Karlsson, *EMC Analysis Methods and Computational Models*. New York: John Wiley & Sons, 1997, Part V Shielding Models.
- [79] D. Pommerenke, I. Krage, W. Kalkner, E. Lemke and P. Schmiegel, "On-site PD measurement on high voltage cable accessories using integrated sensors," in *Proc. 9th Int. Symp. High Voltage, ISH 1995*, Graz, Austria, 1995.
- [80] D. Pommerenke, T. Strehl and W. Kalkner, "Directional coupler sensor for partial discharge recognition on high voltage cable systems," in *Proc. 10th Int. Symp. High Voltage, ISH 1997*, Montreal, Canada, 1997.
- [81] K. Fukunaga, M. Tan and H. Takehana, "New partial discharge detection method for live UHV/EHV cable joints", *IEEE Trans. Electr. Insul.*, vol. 27, no.3, pp. 669-674, Jun. 1992.
- [82] E. Pultrum and M. J. M. Van Riet, "HF partial discharge detection of HV extruded cable accessories", in *Proc. 4th Int. Conf. Power Insulated Cables, JICABLE'95*, Versailles, France, 1995, pp. 662-665.
- [83] R. Heinrich, R. Jobava, W. Kalkner and A. Gheonjian, "Investigation and optimization of a sensor for partial discharge detection on high voltage XLPE cables", in *Proc. 3rd Int. Seminar/Workshop Direct and Inverse Problems of Electromagnetic and Acoustic Wave Theory, 1998*. DIPED-98, Tbilisi, Georgia, 1998, pp. 134-137.
- [84] R. Heinrich, R. Jobava, W. Kalkner and A. Gheonjian, "Numerical modeling for investigation and optimization of a sensor for sensitive partial discharge detection on high-voltage XLPE cables", *Euro Trans. Electr. Power*, vol. 10, no. 3, pp. 161-166, 2000.

-
- [85] R. Heinrich, W. Kalkner, R. Jobava and A. Gheonjian, "Numerical model for radial symmetric sensors for partial discharge detection on XLPE-insulated high voltage cables", in *Proc. 5th Int. Conf. Power Insulated Cables, JICABLE'99*, Versailles, France, 1999, pp. 7-11.
- [86] A. I. Medalia, "Electrical Conduction in Carbon Black Composites", *Rubber Chem. Technol.*, vol. 59, no. 3, pp. 432-454, 1986.
- [87] G. C. Stone and S. A. Boggs, "Propagation of partial discharge pulses in shielded power cable", in *1982 Annu. Rep. Conf. Electr. Insulation Dielectric Phenomena (CEIDP)*, Washington DC, 1982, pp. 275-280.
- [88] S. A. Boggs, A. Pathak and P. Walker, "Partial discharge. XXII. High frequency attenuation in shielded solid dielectric power cable and implications thereof for PD location", *IEEE Electr. Insul. Mag.*, vol. 12, no. 1, pp. 9-16, 1996.
- [89] J. G. Maloney, G. S. Smith and W. R. Scott, "Accurate computation of the radiation from simple antennas using the finite-difference time-domain method," *IEEE Trans. Antennas Propag.*, vol. 38, no. 7, pp. 1059-1068, Jul. 1990.
- [90] R. Jobava, A. Gheonjian, J. Hippeli, G. Chiqovani, D. Karkashadze, F. Bogdanov, B. Khvitia and A. Bzhalava, "Simulation of low-frequency magnetic fields in automotive EMC problems," *IEEE Trans. Electromagn. Compat.*, vol. 56, no. 6, pp. 1420-1430, Dec. 2014.
- [91] K. Mitzner, "Effective boundary conditions for reflection and transmission by an absorbing shell of arbitrary shape," *IEEE Trans. Antennas Propag.*, vol. 16, no. 6, pp. 706-712, Nov. 1968.
- [92] A. Karlsson, "Approximate boundary conditions for thin structures," *IEEE Trans. Antennas Propag.*, vol. 57, no. 1, pp. 144-148, Jan. 2009.
- [93] L. Krahenbuhl and D. Muller, "Thin layers in electrical engineering. Example of shell models in analyzing eddy-currents by boundary and finite element methods," *IEEE Trans. Magn.*, vol. 29, no. 2, pp. 1450-1455, Mar. 1993.
- [94] T. Le-Duc, G. Meunier, O. Chadebec and J.-M. Guichon, "A new integral formulation for eddy current computation in thin conductive shells," *IEEE Trans. Magn.*, vol. 48, no. 2, pp. 427-430, Feb. 2012.
- [95] H. Tsuboi, M. Tanaka and T. Misaki, "Eddy current and deflection analysis of a thin plate in time-changing magnetic field," *IEEE Trans. Magn.*, vol. 26, no. 5, pp. 1647-1649, Sep. 1990.
- [96] H. Chemkha and F. Rioux-Damidau, "A fast and accurate model for eddy current computation in thin conducting shells," *IEEE Trans. Magn.*, vol. 33, no. 2, pp. 1342-1345, Mar. 1997.

- [97] A. Canova, G. Gruosso and M. Repetto, "Integral methods for analysis and design of low-frequency conductive shields," *IEEE Trans. Magn.*, vol. 39, no. 4, pp. 2009–2017, July 2003.
- [98] K. Ishibashi, "Eddy current analysis by integral equation method utilizing loop electric and surface magnetic currents as unknowns," *IEEE Trans. Magn.*, vol. 34, no. 5, pp. 2585–2588, Sep. 1998.
- [99] I. R. Ciric, F. I. Hantila and M. Maricaru, "Field analysis for thin shields in the presence of ferromagnetic bodies," *IEEE Trans. Magn.*, vol. 46, no. 8, pp. 3373–3376, Aug. 2010.
- [100] R. Jobava, A. Gheonjian, D. Karkashadze and J. Hippeli, "Interaction of low frequency magnetic fields with thin 3D sheets of combined resistive and magnetic properties," in *Proc. 2010 European Microwave Conf. (EuMC), Paris, 2010*, pp. 1309–1312.
- [101] R. Jobava, A. Gheonjian, D. Karkashadze and J. Hippeli, "Interaction of low frequency magnetic fields with car chassis," in *Proc. 9th Int. Symp. on EMC, Wroclaw, Poland, 2010*, pp. 284–289.
- [102] R. Jobava, A. Gheonjian, D. Karkashadze, G. Chiqovani, A. Bzhalava and J. Hippeli, "Scattering of low frequency magnetic fields by thin 3D sheets with combined resistive and magnetic properties," in *Proc. 15th Int. Seminar/Workshop on Direct and Inverse Problems of Electromagnetic and Acoustic Wave Theory 2010. DIPED 2010*, Tbilisi, Georgia, 2010, pp. 103–109.
- [103] I. D. Mayergoyz and G. Bedrosian, "On calculation of 3-D eddy currents in conducting and magnetic shields," *IEEE Trans. Magn.*, vol. 31, no. 3, pp. 1319–1324, May 1995.
- [104] S. Koch, H. Schneider and T. Weiland, "A low-frequency approximation to the Maxwell equations simultaneously considering inductive and capacitive phenomena," *IEEE Trans. Magn.*, vol. 48, no. 2, pp. 511–514, Feb. 2012.
- [105] R. Graglia and G. Lombardi, "Singular higher order divergence-conforming bases of additive kind and moments method applications to 3D sharp-wedge structures," *IEEE Trans. Antennas Propag.*, vol. 56, no. 12, pp. 3768–3788, Dec. 2008.
- [106] J. Mautz and R. Harrington, "An E-field solution for a conducting surface small or comparable to the wavelength," *IEEE Trans. Antennas Propag.*, vol. 32, no. 4, pp. 330–339, Apr. 1984.
- [107] D. R. Wilton and A. W. Glisson, "On improving the electric field integral equation at low frequencies," in *Proc. URSI Radio Science Meeting Dig., Los Angeles, CA, 1981*, pp. 24.

-
- [108] W. L. Wu, A. Glisson and D. Kajfez, "A study of two numerical solution procedures for the electric field integral equation at low frequency," *Appl. Comput. Electromagn. Soc. J.*, vol. 10, no. 3, pp. 69–80, 1995.
- [109] M. Burton and S. Kashyap, "A study of a recent moment-method algorithm that is accurate to very low frequencies," *Appl. Comput. Electromagn. Soc. J.*, vol. 10, no. 3, pp. 58–68, 1995.
- [110] G. Vecchi, "Loop-star decomposition of basis functions in the discretization of the EFIE," *IEEE Trans. Antennas Propag.*, vol. 47, no. 2, pp. 339–346, Feb. 1999.
- [111] J. S. Zhao and W. C. Chew, "Integral equation solution of Maxwell's equations from zero frequency to microwave frequencies," *IEEE Trans. Antennas Propag.*, vol. 48, no. 10, pp. 1635–1645, Oct. 2000.
- [112] J.-F. Lee, R. Lee and R. J. Burkholder, "Loop star basis functions and a robust preconditioner for EFIE scattering problems," *IEEE Trans. Antennas Propag.*, vol. 51, no. 8, pp. 1855–1863, Aug. 2003.
- [113] F. Vipiana, G. Vecchi and D. Wilton, "Automatic loop-tree scheme for arbitrary conducting wire-surface structures," *IEEE Trans. Antennas Propag.*, vol. 57, no. 11, pp. 3564–3574, Nov. 2009.
- [114] G. Fairweather, A. Karageorghis and P. A. Martin, "The method of fundamental solutions for scattering and radiation problems," *Eng. Anal. Bound. Elem.*, vol. 27, no. 7, pp. 759–769, 2003.
- [115] M. A. Leontovich, "On the approximate boundary conditions for the electromagnetic field on the surface of well conducting bodies," In *Investigations of Radio Waves*, B. A. Vvedensky, Ed. Moscow: Acad. of Sciences of USSR, 1948 (in Russian), pp. 5-12.
- [116] E. Bulic, A. R. Sinigoj and B. Cestnik, "An equivalent surface source method for computation of the magnetic field reduction of metal shields," *IEEE Trans. Electromagn. Compat.*, vol. 51, no. 2, pp. 263–273, May 2009.
- [117] D. Karkashadze and R. Zaridze, "The method of auxiliary sources in applied electrodynamics," in *Proc. Latsis Symp. Computational Electrodynamics*, Zurich, Switzerland, 1995, pp. 163–180.
- [118] F. Bogdanov, D. Karkashadze and R. Zaridze, "The method of auxiliary Sources in Electromagnetic Scattering Problems," in *Generalized Multipole Techniques for Electromagnetic and Light Scattering*, vol. 4, T. Wriedt, Ed. Amsterdam: Elsevier, 1999, pp. 143–172.
- [119] P. C. Waterman, "Matrix formulation of electromagnetic scattering," *Proc. IEEE*, vol. 53, no. 8, pp. 805–812, Aug. 1965.
-

- [120] E. Arvas, R. Harrington and J. Mautz, "Radiation and scattering from electrically small conducting bodies of arbitrary shape," *IEEE Trans. Antennas Propag.*, vol. 34, no. 1, pp. 66–77, Jan. 1986.
- [121] F. Bogdanov, R. Jobava, A. Gheonjian and K. Khasaia "Application of loop-star and loop-tree basis functions to MoM solution of radiation and scattering problems on complicated surface and wire geometries from low to microwave frequencies," in *Proc. 6th European Conf. Antennas Propag. (EuCAP)*, Prague, Czech Republic, 2012 pp. 1–5.
- [122] J. R. Moser, "Low-frequency shielding of a circular loop electromagnetic field source," *IEEE Trans. Electromagn. Compat.*, vol. 9, pp. 6–18, Mar. 1967.
- [123] P. R. Bannister, "New theoretical expressions for predicting shielding effectiveness for the plane shield case," *IEEE Trans. Electromagn. Compat.*, vol. 10, no. 1, pp. 2–7, Mar. 1968.
- [124] P. R. Bannister, "Further notes for predicting shielding effectiveness for the plane shield case," *IEEE Trans. Electromagn. Compat.*, vol. 11, no. 2, pp. 50–53, May 1969.
- [125] R. W. Latham and K. S. H. Lee, "Theory of inductive shielding," in *EMP Interaction Notes (EMP-3)*, Note XII, Mar. 1968.
- [126] N. Bowler, "Frequency-dependence of relative permeability in steel," *AIP Conf. Proc.*, vol. 820, pp. 1269–1276, 2006.
- [127] A. Gheonjian, B. Khvitia, D. Yeremian, Z. Kuchadze, R. Jobava, and X. Bunlon, "Full wave MOM simulations of EM interactions in EMC filters from 10kHz to 50MHz", In *Proc. 17th Int. Symp. on Electro-Magnetic Compatibility (CEM 2014)*, Clermont-Ferrand, France, 2014.
- [128] E. Hoene, A. Lissner, S. Weber, S. Guttowski, W. John and H. Reichl, "Simulating electromagnetic interactions in high power density inverters", in *Proc. 2005 IEEE 36th Power Electron. Specialists Conf.*, Recife, Brasil, 2005, pp. 1665 – 1670.
- [129] S. P. Weber, E. Hoene, S. Guttowski, W. John and H. Reichl, "Predicting parasitics and inductive coupling in EMI-filters", in *Proc. IEEE 21st Annu. IEEE Appl. Power Electron. Conf. Expo. (APEC 2006)*, Dallas, TX, 2006, vol. 1, pp. 1157-1160.
- [130] E. Hoene, A. Lissner and S. Guttowski, "Prediction of EMI behaviour in terms of passive component placement", in *Proc. 18th Int. Zurich Symp. on EMC*, Munich, Germany, 2007, pp. 49-52.
- [131] S. P. Weber, E. Hoene, S. Guttowski, W. John and H. Reichl, "On coupling with EMI capacitors", in *Proc. 2004 Int. Symp. on EMC*, Santa Clara, CA, 2004, vol. 1, pp. 336-340.

- [132] R. Huang, D. Zhang and K. J. Tseng, "Determination of dimension-independent magnetic and dielectric properties for Mn-Zn ferrite cores and its EMI applications", IEEE Trans. Electromagn. Compat., vol. 50, no. 3, pp. 597 – 602, Aug. 2008.

List of Figures

Fig. 1. Initial car model (334,421 elements)	11
Fig. 2. Coarsened car model (11,014 elements, valid up to 430 MHz)	12
Fig. 3. EMC Studio view of the complex cable harness of a vehicle; boxes represent devices ..	13
Fig. 5. Computational models of vehicle with glass antenna in the rear window	25
Fig. 6. Original (a) and equivalent (b) glass-antenna models	27
Fig. 7. Sources and images in the presence of dielectric interface	28
Fig. 8. Measurement setups for a simple grid antenna on a thin glass	33
Fig. 9. Comparison between the simulation and measurement results	34
Fig. 10. View of the measurement setup for complex grid antenna	35
Fig. 11. Schematic representation of the measurement setup	35
Fig. 12. Comparison of the measurement and simulation results for complex grid antenna ...	36
Fig. 13. Measurement setup for a rear-window automobile glass antenna	37
Fig. 14. Comparison between the simulation and measurement results	37
Fig. 15. Simulation model of measurement setup with a glass antenna and its FM port	38
Fig. 16. Comparison of measurement and simulation results for a complete car model	38
Fig. 17. N-port network directly connected to the MoM geometry	39
Fig. 18. Schematic representation of an antenna validation test	41
Fig. 19. Location of a car and a test antenna in an anechoic chamber	42
Fig. 20. Test antenna dimensions	42
Fig. 21. Antenna factor	42
Fig. 22. Volkswagen car model with a glass antenna in the right window	43
Fig. 23. S-parameters of (a) TV2 amplifier and (b) TV3 amplifier	43
Fig. 24. Voltage received by TV2 antenna in (a) Band I and II, and (b) Band III	44
Fig. 25. Structure of multi-partitioned and multi-excitation calculations	46
Fig. 26. Audi A5 car body with heating structure printed on the rear windscreen	48
Fig. 27. Different variants of antenna structure: (a) initial structure, 102 metallic elements, (b) structure with extended arm, 117 metallic elements, (c) structure with shifted bridge, 117 metallic elements, and (d) reflection coefficient of the above antennas as a function of frequency	49

Fig. 28. Test setup for antenna pattern measurements	50
Fig. 29. Car body exposed to plane waves incident from different angles	50
Fig. 30. Measured S-parameters of RF amplifiers as a function of frequency: (a) AM/FM1 amplifier, (b) FM2 amplifier, (c) DAB amplifier, (d) TV1 amplifier, (e) TV3 amplifier	52
Fig. 31. A car model with a complete antenna pattern considered as a basis part	53
Fig. 32. Pigtail wire copies with different amplifiers (partitions)	53
Fig. 33. Voltage received by antenna with different amplifiers as a function of azimuth angle of plane wave at a frequency 174 MHz: (a) vertical polarisation, (b) horizontal polarisation	53
Fig. 34. Averaged received voltage in FM frequency range: (a) vertical component, (b) horizontal component	54
Fig. 35. Averaged received voltage in DAB/TV (band III) frequency range: (a) vertical component, (b) horizontal component	54
Fig. 36. Part of the cable harness of an automobile	57
Fig. 37. Segmentation of MTL	60
Fig. 38. Equivalent lumped-circuit model for two wires	60
Fig. 39. Equivalent circuit for coaxial cable	62
Fig. 40. Twisted-pair cable	63
Fig. 41. 3-twisted wire cable	63
Fig. 42. Single wire and TWP cable. Measurement setup	64
Fig. 43. Simulation model of a single wire and a TWP cable	64
Fig. 44. Magnitude of the transmission coefficient vs. frequency	64
Fig. 45. Monopole and TWP cable. Measurement setup	65
Fig. 46. Monopole and TWP cable. Simulation model	66
Fig. 47. Active monopole	66
Fig. 48. Active TWP cable	66
Fig. 49. Glass antenna and TWP cable. Measurement setup	67
Fig. 51. Transmission (TWP 901.916)	68
Fig. 52. Transmission (3-twisted 901.951)	68
Fig. 53. Cable and car rear-window antenna. Measurement setup and schematic of cable terminations	69
Fig. 54. Transmission coefficient (common mode)	70
Fig. 55. Transmission coefficient (differential mode)	70

Fig. 56. Schematic representation of an HV cable and PD sensor 72

Fig. 57. FDTD grid for HD cable and PD sensor 75

Fig. 58. Measurement setup for experimental optimisation of the sensor 76

Fig. 59. Output signal of the sensor, simulation and measurement 77

Fig. 60. Sensitivity vs. length of sensor for 3 ns pulse width 78

Fig. 61. Sensitivity vs. thickness of the dielectric substrate 78

Fig. 62. Contour plot of H-field for different time steps 79

Fig. 63. Measurement setup: single cable and Coroplast 35 mm² cable with adapters 80

Fig. 64. Measurement sample of Coroplast 35 mm² cable with adapters 80

Fig. 65. Computational model for crosstalk analysis using an LCTL scheme of the transmission line 81

Fig. 66. System diagram for crosstalk calculations 81

Fig. 67. Layered shield: braided shield with aluminium foil wrapped around it 81

Fig. 68. Braided shield without foil 81

Fig. 69. Cross section of HV cable Coroplast 35 mm² 83

Fig. 70. Cable termination with adapter and N-type connector 83

Fig. 71. Transfer impedance of braided and layered shields 83

Fig. 72. Transmission coefficient vs. frequency 83

Fig. 73. HV cable samples with perfect and resistive connections between the cable shield and the adapter box 84

Fig. 74. Model for MoM calculations with solid shield and 16 SMD resistors 84

Fig. 75. Model for 3D simulations using MoM 85

Fig. 76. Influence of contact resistance 85

Fig. 77. Cross section of HV cable Coroplast 25 mm² 87

Fig. 78. Cable termination with adapter and N-type connector 87

Fig. 79. Transfer impedance of layered shield of the Coroplast 25 mm² cable 87

Fig. 80. Input impedance at Port1 of Coroplast 25 mm² 88

Fig. 81. Transmission coefficient between shielded cable and single wire vs. frequency 88

Fig. 82. Coaxial loops separated by an infinite plane [122] 100

Fig. 83. Shielding effectiveness vs. frequency for a plate made of an aluminium alloy. An infinite plane is used for the analytical solution. For measurement and numerical simulations, the plate has dimensions 1.22 m × 1.22 m and is comprised of a triangular mesh with edge lengths of 1 cm	101
Fig. 84. A vertical loop above a finite plate	102
Fig. 85. Total electric E-field at various observation points, located above the edge of a plate (frequency = 10 kHz)	102
Fig. 86. Shielding effectiveness vs. frequency for a spherical shell	103
Fig. 87. A model of a car body with a power-supply cable	104
Fig. 88. Comparison of measured and calculated B-field in a car	104
Fig. 89. Distribution of the B-field in the cross section of a carbon car body (frequency = 10 Hz)	105
Fig. 90. Coil antenna of a smart-key system	106
Fig. 91. Measurement setup with antenna in free space	107
Fig. 92. Transmitting antenna in free space	107
Fig. 93. H-field for antenna in free space, ρ -component	108
Fig. 94. H-field for antenna in free space, φ -component	108
Fig. 95. A transmitting antenna with aluminium shield. Position of the shield: L=5 cm from the antenna centre. Position of the field probe: d=95 cm from the antenna centre	109
Fig. 96. H-field for the antenna located near the edge of the aluminium shield, ρ -component	110
Fig. 97. H-field for the antenna located near the edge of the aluminium shield, φ -component	110
Fig. 98. Positions of three ferrite-rod antennas inside a car model	111
Fig. 99. Isoline representation of the B-field at 1 nT	112
Fig. 100. Isosurface at a 1 nT B-field for an internal antenna	112
Fig. 101. Model details of the transmitting coil of an inductive charging system	113
Fig. 102. Near-field distribution of the B-field (frequency = 150 kHz, power = 3 kW)	114
Fig. 103. Modelling of film capacitor	116
Fig. 104. Transmission coefficient	117
Fig. 105. Measured sample and model of coil	118
Fig. 107. Coil impedance	119

Fig. 106. Frequency dependence of the complex permeability and permittivity of EPCOS N30 ferrite material 119

Fig. 108. Schematic of the filter under study 120

Fig. 109. Filter layouts and corresponding 3D models 121

Fig. 110. Measurement of the DM transfer function 122

Fig. 111. Simulation model with baluns and coaxial lines 122

Fig. 112. Simulated and measured CM transfer functions 123

Fig. 113. Simulated and measured DM transfer functions 123

Fig. 114. Observation of B-field distribution (example of filter Model 2) 124

Fig. 115. Measured vertical component of the B-field at 1 MHz for filter Model 2 125

Fig. 116. Simulated vertical component of the B-field at 1 MHz for filter Model 2 125

Fig. 117. Simulated vertical component of the B-field at 1 MHz for filter Model 1 126

List of Tables

Table 1. Solving times and gains for sequential calculations for $\beta = 0$	47
Table 2. Solving times and gains for cluster calculations	47
Table 3. Summary of computational times	49
Table 4. Summary of computational times	54
Table 7. Model element dimensions	116
Table 8. Toroidal core dimensions	118